

A Magnetotelluric Investigation  
of an Electrical Conductivity Anomaly  
in the Southwestern United States

by

CHARLES MOORE SWIFT, Jr.

A.B., Princeton University  
(1962)

SUBMITTED IN PARTIAL FULFILLMENT

OF THE REQUIREMENTS FOR THE

DEGREE OF DOCTOR OF

PHILOSOPHY

at the

MASSACHUSETTS INSTITUTE OF

TECHNOLOGY

July, 1967

Signature of Author. . .

Department of Geology and Geophysics, July 31, 1967

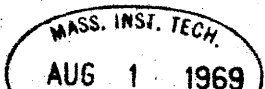
Certified by . . . . .

Thesis Supervisor

Accepted by. . . . .

Chairman, Departmental Committee on Graduate Students

Lindgren





Room 14-0551  
77 Massachusetts Avenue  
Cambridge, MA 02139  
Ph: 617.253.5668 Fax: 617.253.1690  
Email: docs@mit.edu  
<http://libraries.mit.edu/docs>

## **DISCLAIMER OF QUALITY**

Due to the condition of the original material, there are unavoidable flaws in this reproduction. We have made every effort possible to provide you with the best copy available. If you are dissatisfied with this product and find it unusable, please contact Document Services as soon as possible.

Thank you.

**Due to the poor quality of the original document, there is some spotting or background shading in this document.**

A MAGNETOTELLURIC INVESTIGATION OF AN ELECTRICAL CONDUCTIVITY  
ANOMALY IN THE SOUTHWESTERN UNITED STATES

by

Charles Moore Swift, Jr.

Submitted to the Department of Geology and Geophysics

on July 31, 1967 in

partial fulfillment of the requirements for the

degree of Doctor of Philosophy

ABSTRACT

Large scale magnetotelluric observations were made in the southwestern United States by combining telluric data from seven sites with Tucson geomagnetic observatory data. The use of the Tucson data as representative for the telluric recording sites is justified by a quantitative coherency study, which showed that the geomagnetic fluctuations of fifteen minute to diurnal periods in the southwest are characterized by horizontal wavelengths greater than 10,000 kilometers. The magnetotelluric data is analyzed for tensor apparent resistivities, principal directions, and two-dimensionality measures.

The measured anisotropic apparent resistivities are interpreted in terms of inhomogeneous resistivity structure, using theoretical values obtained for two-dimensional models which took the known surface geology into account. The resulting interpretations show a high conductivity zone in the upper mantle of southern Arizona and southwestern New Mexico. Thus, the magnetotelluric evidence supports Schmucker's geomagnetic indication of increased conductivities. Partly because this region is characterized by high heat flow, these high conductivities are attributed to a zone of high temperatures.

Using Ringwood's "pyrolite" petrologic model for the upper mantle and laboratory conductivity measurements on pyrolite constituents, a temperature differential at a depth of 50 km of 600° with respect to a normal geotherm is postulated. This temperature and compositional model incorporates a lateral phase change within the pyrolite and is consistent with the observed low  $P_n$  velocities, low density, and high heat flow observed in the Southwest. This anomalous zone is believed to represent an extension of the East Pacific Rise under continental North America.

Thesis Supervisor: Theodore R. Madden

Title: Professor of Geophysics

### Acknowledgements

A thesis usually does not represent an isolated piece of research. This is true of the present investigation, and I would like to express my indebtedness to the previous published and unpublished work done in magnetotellurics by the M.I.T. Geophysics Department.

Primarily, I would like to thank my thesis advisor, Professor Theodore R. Madden, for suggesting the thesis topic and for providing guidance and assistance throughout this investigation. Besides contributing the recording instrumentation, computer programs, and much physical insight into the problems, Professor Madden has continually admonished me to support speculative statements with concrete evidence.

I would like to acknowledge the following for helpful discussions - Mr. David Blackwell, Dr. Jon Claerbout, Dr. Phillip Nelson, Dr. Ulrich Schmucker, Mr. William Sill, Dr. David Strangway and Dr. Keeva Vozoff. Dr. Joel Watkins provided the gravity maps of the Phoenix area.

Dr. Ralph Holmer of the Kennecott Copper Corporation permitted me to spend many days acquiring telluric data while employed for summer work. Many employees of the

Mountain States Telephone Company co-operated by setting up the unorthodox telephone circuits.

Research Calculations of Newton, Massachusetts, digitized the 1966 telluric records. Dr. William Paulishak, of the Data Center Branch, Geomagnetism Division, Coast and Geodetic Survey, ESSA, supplied the digitized magnetic data. The digital calculations were performed at the M.I.T. Computation Center, who also provided some computer time at the beginning of this investigation. Mariann Pilch typed the manuscript.

During his graduate years the author has held an M.I.T. Whitney Fellowship, an N.S.F. Graduate Fellowship, and a research assistantship financed by the American Chemical Society. The Office of Naval Research has funded the work through Contracts Nonr 1841(75) and Nonr. (G)00041-66.

Finally, I would like to thank my wife, Tricia, for her patience and moral support, particularly during the final months.

TABLE OF CONTENTS

ABSTRACT	ii	27
ACKNOWLEDGEMENTS	iv	28
TABLE OF CONTENTS	vi	29
LIST OF FIGURES AND TABLES	ix	30
CHAPTER 1 - INTRODUCTION	1	
1.1 Purpose of investigation	1	
1.2 Brief historical review of the magnetotelluric method	4	
1.3 Upper Mantle conductivity determinations	7	
1.4 Outline of thesis	11	
CHAPTER 2 - MAGNETOTELLURIC THEORY	13	
2.1 Relationships from Maxwell's Equations	14	
2.2 Magnetotelluric solutions for a layered earth geometry	22	
2.3 Impedance of a spherically stratified conductor	28	
Transmission-line analogy formulation and solution	34	
2.4 Magnetotelluric relationships for a two-dimensional geometry	40	
Maxwell's Equations formulation	42	
Transmission-surface analogy formulation	45	
Network solution for theoretical apparent resistivities	49	
Example - theoretical apparent resistivities over a vertical contact	53	
2.5 Properties of the magnetotelluric impedance tensor	57	
Properties of theoretical impedance tensor	58	
Characteristics of measured impedance tensor	61	
Improper impedance tensors from finite-length dipoles	64	

TABLE OF CONTENTS (continued)

CHAPTER 3 - MAGNETOTELLURIC EXPERIMENTS IN THE SOUTH- WESTERN UNITED STATES	69
3.1 Magnetic field data	69
Sources of the incident magnetic field	75
3.2 Electric field measurement	77
3.3 Method of data analysis	82
Higher frequency analysis	83
Lower frequency analysis	87
Sources of error	88
3.4 Magnetotelluric apparent resistivity results	96
Roswell, New Mexico	96
Deming, New Mexico	109
Safford, Arizona	113
Tucson, Arizona	117
Phoenix, Arizona	120
Yuma, Arizona	126
Gallup, New Mexico	130
3.5 Interpreted conductivity structure from magnetotelluric apparent resistivities	133
Interpretation of Safford results	134
Interpretation of Roswell and Deming results	137
Interpretation of Phoenix results	140
Interpretation of Gallup results	142
Disucssion of the Yuma and Tucson results	145
Summary of interpretation	151
CHAPTER 4 - INTERPRETATION OF THE ELECTRICAL CONDUCTIVITY ANOMALY	156
4.1 Electrical conductivity of the upper mantle	156
Upper mantle temperature distribution from conductivity structure	163
4.2 Correlation of high temperature zone with other geophysical data	169
Seismic evidence	169
Heat flow evidence	173
Relationship to the East Pacific Rise	175



TABLE OF CONTENTS (continued)

CHAPTER 5 - SUGGESTIONS FOR FUTURE WORK	180
APPENDIX 1 - Error introduced by lumped circuit approximation to a distributed transmission line	182
APPENDIX 2 - Calculation of the vertical electric field associated with a toroidal B mode diurnal	185
APPENDIX 3 - Greenfield algorithm for the direct solution of the magnetotelluric network equations	189
APPENDIX 4 - Principal axis and principal values of the magnetotelluric impedance tensor	194
APPENDIX 5 - Computational details of the sonogram analysis	198
REFERENCES	201
BIOGRAPHICAL NOTE	211

LIST OF FIGURES AND TABLES

<u>Figure</u>		
2.1	Electromagnetic skin depths	17
2.2	Equivalent network for the spherically stratified conductor	37
2.3	Cantwell-McDonald conductivity model	38
2.4	Electromagnetic fields over a lateral conductivity contrast	41
2.5	Theoretical apparent resistivities over a vertical contact	54
2.6	Theoretical magnetotelluric fields over a vertical contact	55
2.7	Effect of finite-length dipoles on the measured apparent resistivity over a vertical contact	68
3.1	Location map for telluric recording sites	70
3.2	Geomagnetic observatory data, Dallas and Tucson	72
3.3	Coherency analysis of Dallas and Tucson magnetics	73
3.4	Telluric instrumentation response	79
3.5	Magnetotelluric field data, Roswell, New Mexico	97
3.6	Power spectra and coherencies, Roswell, New Mexico	98
3.7	Electric field predictability, Roswell, New Mexico	99
3.8	Time consistency of apparent resistivity estimates, Roswell, New Mexico	101
3.9	Magnetotelluric results, Roswell, New Mexico	103
3.10	Electric and magnetic field hodographs, Roswell, New Mexico	107
3.11	Magnetotelluric results using Dallas magnetics, Roswell, New Mexico	108
3.12	Magnetotelluric field data, Deming, New Mexico	110

LIST OF FIGURES AND TABLES (continued)

3.13	Magnetotelluric results, Deming, New Mexico	111
3.14	Electric and magnetic field hodographs, Deming, New Mexico	112
3.15	Magnetotelluric field data, Safford, Arizona	114
3.16	Magnetotelluric results, Safford, Arizona	115
3.17	Electric and magnetic field hodographs, Safford and Tucson, Arizona	116
3.18	Magnetotelluric field data, Tucson, Arizona	118
3.19	Magnetotelluric results, Tucson, Arizona	119
3.20	Magnetotelluric field data, July 1965, Phoenix, Arizona	121
3.21	Magnetotelluric field data, July, 1966, Phoenix, Arizona	122
3.22	Magnetotelluric results, 1965 data, Phoenix, Arizona	123
3.23	Magnetotelluric results, 1966 data, Phoenix, Arizona	124
3.24	Electric and magnetic field hodographs, Phoenix, Arizona	125
3.25	Magnetotelluric field data, Yuma, Arizona	128
3.26	Magnetotelluric results, Yuma, Arizona	129
3.27	Magnetotelluric field data, Gallup, New Mexico	131
3.28	Magnetotelluric results, Gallup, New Mexico	132
3.29	Interpreted conductivity structure, Safford	136
3.30	Interpreted conductivity structure, Deming and Roswell	139
3.31	Gravity map of Phoenix area	141
3.32	Elevation of basement rocks, southwest United States	144
3.33	Interpreted conductivity structure, Gallup	146

LIST OF FIGURES AND TABLES (continued)

---

3.34	Summarized magnetotelluric earth conductivity profiles	153
3.35	Summarized theoretical apparent resistivity profiles	155
4.1	Pyrolite stability fields	158
4.2	Conductivity-temperature plots for mantle constituents	160
4.3	Postulated temperature cross-section	167
4.4	Seismic evidence for an inhomogeneous upper mantle, western United States	170
4.5	Heat flow measurements, western United States	174
4.6	Cenozoic fault system and extensional tectonic pattern, western United States	176
A.1	Coefficient matrix for network solution	190
A.2	Response of digital filters	199

Table

2.1	Apparent resistivities for a spherically stratified earth	39
3.1	Telluric recording data	80
3.2	Representative $H_{\text{vertical}}/H_{\text{horizontal}}$ ratios, Tucson, Arizona	149

## Chapter 1 - Introduction

### 1.1 Purpose of investigation

The science of geophysics is the systematic application of physics to determine the composition and behavior of the earth and the earth environment. As such, much of solid-earth geophysics consists of the indirect techniques of interpreting the internal structure of the earth from surface measurements. This thesis is concerned with the magnetotelluric method of determining subsurface electrical conductivity by measuring the electromagnetic impedance of the earth.

In the upper crust, where conductivity variations can usually be correlated with differences in rock types and/or water content, structure has been inferred using telluric current and direct current resistivity methods. In the mantle, where conductivity variations can usually be correlated with differences in temperature, conductivity anomalies have been detected using geomagnetic induction methods.

The magnetotelluric method, which was recognized in the early 1950's, is capable of yielding quantitative information about the conductivity structure of the crust and

upper mantle. Theoretical and practical difficulties, however, have plagued the successful application of the method. The possible non-plane-wave nature of the sources has been called upon to explain inconsistent data. More important, the effect of lateral conductivity variations has not been understood quantitatively. Qualitatively, the electric currents, preferring to flow in a more conductive medium, may flow in a direction controlled by the lateral conductivity structure of the local geology rather than in a direction perpendicular to the magnetic field as expected when no lateral resistivity contrast is present. Because the resulting electric field is not always orthogonal to the magnetic field, the measured apparent resistivities can be anisotropic.

The original purpose of this thesis was to investigate the reasons for the anomalously low vertical magnetic field fluctuations observed at Tucson, Arizona. Small vertical magnetic fields can be caused by horizontally layered conductive rocks. Tucson is known to be in a zone of anomalously high electrical conductivity in the southwestern United States (Schmucker, 1964). High apparent resistivities, however, were obtained by a rough calculation using diurnal variations of E and H given by Fleming (1939).

Although not definitive in the Tucson region, initial magnetotelluric data taken by the author in the summer of 1965 in the southwestern United States appeared interesting enough to justify further work in 1966 to more accurately determine the high conductivities and the inferred high temperatures associated with the Basin and Range province.

In the author's opinion, the contribution of this thesis is the interpretation of low frequency magnetotelluric data in terms of a petrologically valid upper mantle conductivity structure in a geologically anomalous region. Anisotropic apparent resistivity data is interpreted quantitatively in terms of two-dimensional conductivity structure, using theoretical values obtained via a transmission-line analogy due to T. R. Madden. The conductivity structure resulting from this magnetotelluric investigation correlates with other geophysical evidence to indicate that the anomalous upper mantle in the southwestern United States represents an extension of the East Pacific Rise.

## 1.2 Brief historical review of the magnetotelluric method

Magnetotelluric theory is the result of a recent approach towards determining the relationship between telluric currents and the geomagnetic field. In 1940 Chapman and Bartels reviewed the confusing state of the correlation between earth-current variations and geomagnetic activity. Subsequently, by considering the phase relationships between observed electric and magnetic fields at the surface of the earth, various workers in the early 1950's (Tikhonov and Lipskaya in Russia; Kato, Kikuchi, and Rikitake in Japan) discovered the electromagnetic nature of the magnetotelluric field. In 1953 Cagniard published a comprehensive paper on the theory of the magnetotelluric field within a horizontally layered earth and on interpretive methods for obtaining earth resistivity estimates.

Magnetotelluric field data have been successfully interpreted only for horizontally layered structures; representative papers are by Cantwell (1960) and Tikhonov and Berdichevskii (1966). Problems have arisen in interpreting magnetotelluric data in areas of lateral conductivity (Srivastava, Douglass and Ward, 1963, for example).

Further theoretical contributions have considered three problems - the assumption of a plane incident wave, the



tensor nature of the impedance, and theoretical apparent resistivities for two dimensional structures.

Wait (1954) showed how Cagniard's results for a layered earth are valid only if the fields themselves do not vary appreciably in a horizontal distance of the order of a skin depth in the ground. Consequently, the field should be uniform over a considerably broad area to permit the Cagniard interpretive procedure to be applied. Price (1962) has reemphasized this restriction. However, Madden and Nelson (1964) have considered a realistic earth conductivity profile and have concluded that the plane-wave assumption is valid in most cases.

For an anisotropic or inhomogeneous earth, the field apparent resistivity data become anisotropic because the impedance becomes a tensor quantity. Chetaev (1960), Kovtun (1961), Rokityanski (1961), Cantwell (1960) and Bostick and Smith (1962) have provided schemes to obtain the principal directions of the conductivity structure. Wait (1962) has a good review of the Russian work. Madden and Nelson (1964) have indicated how to calculate the tensor components using statistical and spectral techniques.

Early discussions of the effect of two-dimensional conductivity structures centered around the "coast effect".

This effect, an enhancement of the vertical magnetic field near a coastline associated with an enhanced telluric field on the land directed towards the coast (Parkinson, 1962; Rokityanskii, 1963), is due to the lateral contrast in conductivity between the conductive oceans and oceanic mantle and the more resistive continents. In the first quantitative approach, Neves (1957) calculated apparent resistivities over dipping interfaces using a finite difference technique, but used the correct boundary conditions only for the electric field polarized perpendicular to the strike polarization. d'Erceville and Kunetz (1962) analytically solved the problem of a fault within a layer over a half space by expanding the fields in trigonometric series for the E perpendicular polarization. Weaver (1963) solved the infinite depth vertical contact problem, again only correctly for the E perpendicular polarization, by numerical evaluation of the solution integrals.

### 1.3 Upper mantle conductivity determinations

As included in an impressive bibliography by Fournier (1966), presently available magnetotelluric results are characterized by the decrease of apparent resistivities for periods of longer than two hours. This effect is due to the deeper sampling into the conductive upper mantle under the resistive crust for increasing period.

Most individual magnetotelluric measurements are characterized by a limited frequency range and have been interpreted in terms of a step increase in conductivity. The depth to this interface and the conductivity beneath vary widely, with a greater depth required for lower frequency measurements. These results are indicative of a continuously increasing conductivity with depth corresponding to the increasing temperatures.

Earth electrical conductivity information is also provided by analysis of geomagnetic variations. Chapman and Whitehead (1923), Chapman and Price (1930), Lahiri and Price (1939) and Rikitake (1950) have used the ratios of the internal to external source terms of the earth's surface potential for the diurnal variations and storm time transients to essentially define the depth to, and the conductivity of a conductive mantle. McDonald (1957)

analyzed the attenuation of the secular variations through the mantle for conductivity estimates for the lower mantle and combined his conclusions with those of Lahiri and Price (1939) for a mantle conductivity profile. Eckhardt, et al (1963) found that McDonald's model was adequate to explain their magnetic fluctuation data of 13.5 day and 6 month periods.

Although these determinations are relatively consistent, a unique earth conductivity model within narrow limits of uncertainty is presently unavailable.

Upper mantle perturbations from a radially symmetric conductivity distribution can be detected using either the magnetic induction or the magnetotelluric method. For rough detection, locally anomalous ratios of vertical to horizontal field components are the magnetic induction indication of lateral conductivity contrasts. Similarly, different one-dimensional magnetotelluric profiles at separated stations are indicative of lateral conductivity contrasts. For proper interpretation, the magnetic induction method requires sufficient coverage to separate the external and the internal fields. Similarly, continuous magnetotelluric coverage is required for a proper delineation of lateral contrasts. Unfortunately, as shown in

the results of this thesis, the magnetotelluric indications of anomalous upper mantle structures can be lost in the severe effects of surficial conductivity structure. When measurements are made parallel to the strike of such surficial structures, however, their effects are greatly diminished.

The major perturbation from a radially symmetric conductivity distribution is the conductive ocean and conductive oceanic mantle. The conductive oceanic mantle, which is probably due to the increased temperatures (McDonald, 1963; Clark and Ringwood, 1964), causes the geomagnetic coast effect. A reverse ocean-effect has been measured along the coast of Peru (Schmucker, et al, 1964); the proximity of an ocean trench could explain the necessary low temperatures.

The world wide occurrence and geomagnetic interpretations of isolated "upper mantle conductivity anomalies" has been reviewed recently by Rikitake (1966). These anomalies are usually pictured as conductive spheres or cylinders or as variations in the depth to an infinitely conducting mantle under an insulating crust. However, many anomalies are not satisfactorily explained. The Japan anomaly, for example, appears to be superimposed upon

a coastline effect. Magnetotelluric measurements are now being made in some of these anomalous regions to reduce the ambiguity in the interpretations. However, the Alert Anomaly in northern Canada has been analyzed by both techniques without a satisfactory interpretation (Rikitake and Whitham, 1964; Whitham and Anderson, 1965; Whitham, 1965). Also, the North German Anomaly, originally attributed to a cylindrical conductor at depth (reviewed by Kertz, 1964), is now interpreted to be complicated by surface conductivity structures from magnetotelluric data (Vozoff and Swift). This thesis represents a magnetotelluric investigation of the conductivity anomaly in the southwestern United States, originally detected by Schmucker (1964).

#### 1.4 Outline of thesis

Chapter 2, on magnetotelluric theory, first describes the basic one-dimensional theory and applies it to a realistic spherically stratified earth conductivity structure to obtain the effect of finite horizontal wavelengths in the source field on apparent resistivities. The equations for an earth with lateral conductivity contrasts are developed, are transformed into circuit equations via a transmission-surface analogy, and are solved numerically via network techniques for theoretical apparent resistivities. Finally, characteristics of theoretical and measured impedance tensors are discussed.

Chapter 3 describes the acquisition, analysis, results and interpretation of magnetotelluric data from the southwestern United States. A coherency study of magnetic data from Tucson, Arizona, and Dallas, Texas, is included to determine empirically the horizontal wavelengths of the source field. The technique for obtaining theoretical apparent resistivities over two-dimensional structures is applied to obtain models necessary to explain the actual anisotropic apparent resistivity data.

In Chapter 4 the resulting electrical conductivity structure is interpreted geologically. With reference to

laboratory measurements of the conductivity-temperature relationships of upper mantle constituents, a temperature cross-section is obtained consistent with the conductivity structure. Finally, the electrical conductivity anomaly is correlated with other geophysical data to draw some conclusions on the relationship between the North American continent and the East Pacific Rise.

Chapter 5 includes some suggestions for further work and is followed by five miscellaneous topics in Appendices.



## Chapter 2 - Magnetotelluric Theory

The magnetotelluric method utilizes the boundary conditions forced on the electric and magnetic fields when an electromagnetic wave propagating through air interacts with the earth's surface. Whereas the incident horizontal magnetic field is roughly doubled at the surface, the electric field is strongly dependent upon the earth's conductivity structure. The essential measurement is the electromagnetic impedance (the ratio of electric field over magnetic field,  $E/H$ ) at the surface.

Since the electric and magnetic fields are vector quantities, the impedance is really a 3 by 3 tensor. At the surface of the earth, where  $E_z$  vanishes, this tensor reduces to a 2 by 2 when the horizontal wavelengths are fixed. For a homogeneous or a layered earth, the horizontal electric field is only related to the orthogonal magnetic field, and the impedance reduces to a complex scalar. In general, for an anisotropic earth (homogeneous media with  $J_i = \sigma_{ij} E_j$ ) or an inhomogeneous earth (lateral variations of isotropic conductivity) the electric field is related to both horizontal magnetic field components, and the impedance must be treated as a 2 by 2 tensor.

Most geophysical disciplines consider progressively more complicated, and, hence, more realistic earth models as theory develops. In this chapter, a homogeneous earth geometry is first considered to develop the basic magnetotelluric relationships and to calculate the effect of finite horizontal wavelengths upon the impedance. Then a plane and spherically stratified earth geometry is considered using various layered-media techniques. Then a two-dimensional earth geometry, in which a conductivity cross section is constant along a strike direction, is considered to calculate the effect of lateral conductivity contrasts. Finally, the properties of the 2 by 2 impedance tensor are discussed.

## 2.1 Relationships from Maxwell's Equations

In the following derivations in Cartesian co-ordinates, the geomagnetic co-ordinate convention will be used, with x - north, y - east, and z - down. In homogeneous isotropic media, in the absence of sources, Maxwell's equations in the rationalized MKS system are

$$\nabla \times E = - \frac{\partial B}{\partial t} \quad 2.1-1$$

$$\nabla \times H = J + \frac{\partial D}{\partial t} \quad 2.1-2$$

$$\nabla \cdot D = \rho = 0 \quad 2.1-3$$

$$\nabla \cdot B = 0 \quad 2.1-4$$

where  $J = \sigma E$ ,  $D = \epsilon E$ ,  $B = \mu H$

By assuming  $e^{-i\omega t}$  time dependence, these equations reduce to

$$\nabla \times E = i\omega\mu H \quad 2.1-5$$

$$\nabla \times H = \sigma E - i\omega\epsilon E \quad 2.1-6$$

It is standard procedure to combine these two equations into the vector Helmholtz equation

$$\nabla^2 \begin{Bmatrix} E \\ H \end{Bmatrix} + k^2 \begin{Bmatrix} E \\ H \end{Bmatrix} = 0 \quad 2.1-7$$

$$k^2 = i\omega\mu\sigma + \epsilon\mu\omega^2$$

This formulation emphasizes the wave nature of the solutions

$$\begin{Bmatrix} E \\ H \end{Bmatrix} = e^{i(k_x x + k_y y + k_z z)}$$

$$k^2 = k_x^2 + k_y^2 + k_z^2$$

In electromagnetic propagation in the earth at magnetotelluric frequencies ( $\omega < 10^4$  cps), the propagation constant is dominated by the conduction current term ( $i\omega\mu\sigma$ ), and the Helmholtz equation becomes a diffusion equation.

The solution field does not freely propagate, but exponentially decays with depth; this decay, dependent upon the conductivity and frequency, is called the "skin effect". The skin depth, defined as that depth at which the fields reduce to  $1/e$  of the surface value, affords a rather crude qualitative estimate of an effective "depth of penetration". Skin depths,  $\delta = \sqrt{\frac{2}{\mu\omega\sigma}}$ , are given in Figure 2.1 as a function of  $\sigma$  and  $\omega$ , assuming a free space value for  $\mu$ . Therefore, the frequency range appropriate for a magnetotelluric investigation depends upon the depths of interest.

The conduction current term is much greater than the displacement current term for most magnetotelluric instances and the propagation constant in the ground is much greater than in the air:

$$k_{air}^2 = \mu\epsilon\omega^2 \ll |i\omega\mu\sigma| = |k_{earth}^2|$$

Thus, the earth has a high refractive index with respect to the air, and incident waves will be refracted almost straight down, regardless of the angle of incidence.

The impedance relationships are dependent on the spatial variations of the incident field, not on the nature of the source itself. The source of the electromagnetic energy depends upon the frequency range involved; the sources for the low frequency magnetotelluric data analyzed in this thesis

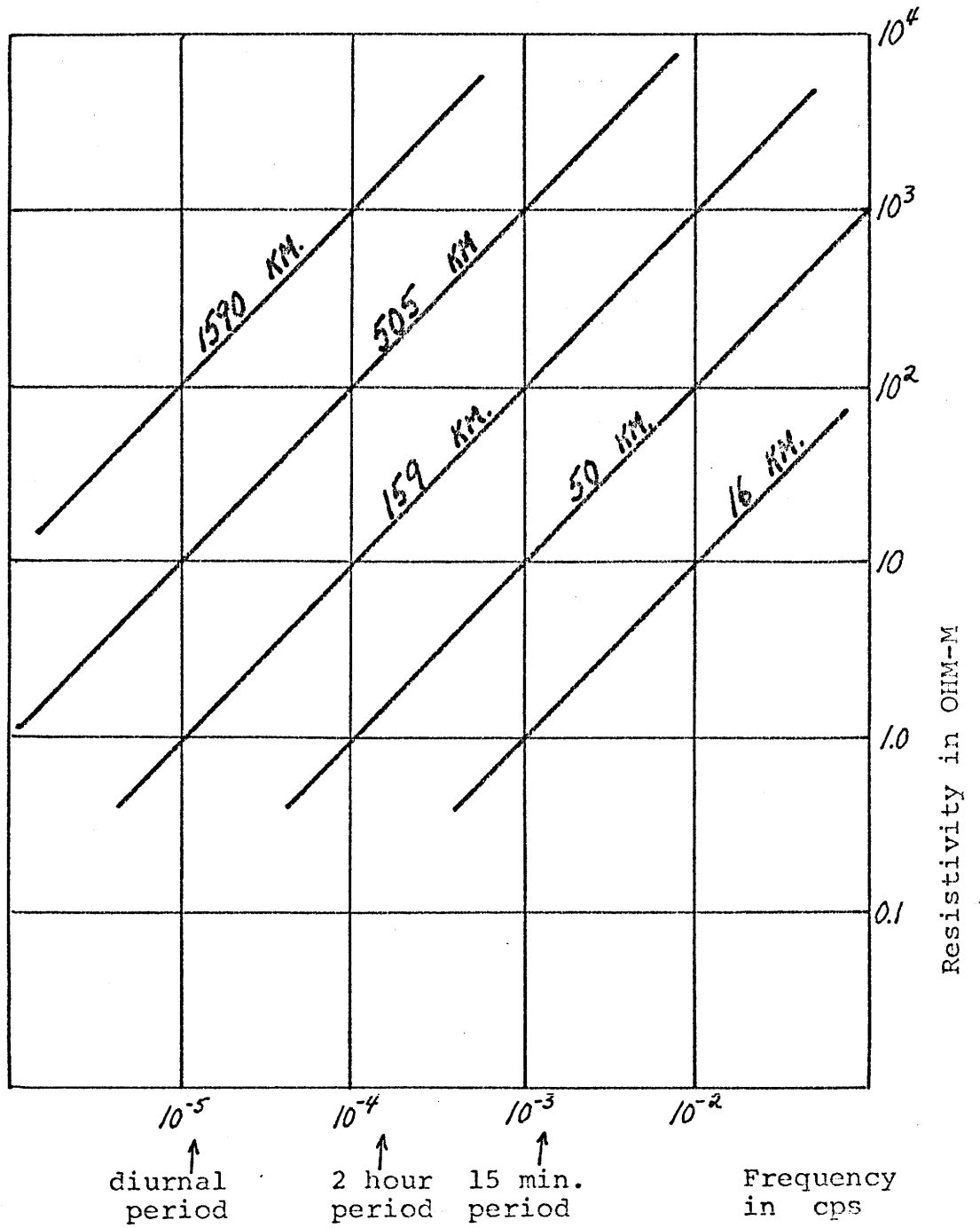


Figure 2.1 Electromagnetic Skin Depths as a Function of Frequency and Resistivity.

are discussed in Chapter III.

The straight-forward calculation of wave refraction at the earth's surface introduces the effects of a finite horizontal wavelength on the impedance. This calculation is given for the two polarizations, "E horizontal" and "H horizontal", in which the specified field is linearly polarized parallel to the earth's surface.

For an incident E horizontal wave,

$$E^I = E_x^I e^{\pm i(k_x x + k_y y + k_z z)} \quad 2.1-8$$

the refracted wave is obtained by matching phases at the boundary, as

$$E_x^T = E_x^T e^{\pm i(k_x x + k_y y + k_{z_1} z)} \quad 2.1-9$$

From Maxwell equation 2.1-1, the associated tangential magnetic field is

$$H_y^T = \frac{k_{z_1}}{\mu\omega} E_x^T \quad 2.1-10$$

Therefore, the impedance is defined as

$$\eta \equiv E_x/H_y = \mu\omega/k_{z_1} \quad 2.1-11$$

where  $k^2 = i\omega\mu\sigma = k_{z_1}^2 + k_x^2 + k_y^2$

Analogously, for an incident H horizontal wave,

$$H^I = H_x^I e^{\pm i(k_x x + k_y y + k_z z)} \quad 2.1-12$$

and the refracted wave is

$$H_x^T = H_x^T e^{\pm i(k_x x + k_y y + k_z z)}$$

From Maxwell equation 2.1-2, the associated tangential electric field is

$$E_y^T = \frac{ik_{z_1}}{\sigma} H_x^T \quad 2.1-13$$

Therefore, the impedance is given as

$$\eta \equiv -E_y/H_x = -\frac{ik_{z_1}}{\sigma} \quad 2.1-14$$

The fact that the impedance depends upon the horizontal wavelength ( $1/k_y$ ,  $1/k_x$ ) has caused the continuous debate over the plane wave assumption of Cagniard (1953). If the impedance does depend upon the horizontal wavelength, knowledge of the spatial distribution of the source field is required. If, however,  $k_x^2 + k_y^2 \ll k^2$  then  $k_{z_1}^2 \approx k^2$ , and the impedance is independent of the source field geometry. This requires that the horizontal wavelength is much greater than the skin depth in the earth.

For sources with relatively long wavelengths, the E parallel and H horizontal impedances are equal, and thus the

impedance for a homogeneous halfspace is isotropic. This impedance is

$$\eta = \frac{\mu\omega}{k} = \frac{-ik}{\sigma} = \sqrt{\frac{-i\mu\omega}{\sigma}} \quad 2.1-15$$

The phase of this impedance is  $-45^\circ$ , which means that the magnetic field lags the orthogonal electric field.

The resistivity is simply obtained from the impedance by

$$\rho = \frac{1}{-i\mu\omega} \eta^2 \quad 2.1-16$$

For a homogeneous earth, the calculated  $\rho$  will be the true earth resistivity. For a heterogeneous earth, the calculation will yield a complex frequency-dependent apparent resistivity. Through the skin effect, sufficient degrees of freedom are inherent in apparent resistivity data as a function of frequency to permit a magnetotelluric sounding interpretation in the form of a resistivity versus depth profile.

The concept of an apparent resistivity is familiar from standard resistivity methods. Moreover, the concept of an apparent resistivity as a function of frequency is analogous to a dispersion curve in wave propagation. This is important for two reasons. First, it suggests that the



the impedance is as physically important as, say, the phase velocity. Secondly, it indicates that the determination of the conductivity distribution from apparent resistivity data is a typical geophysical inverse boundary-value problem.

## 2.2 Magnetotelluric solutions for a layered earth geometry

The original method for calculating the surface impedance of a horizontally layered earth is to set up wave solutions for each layer, to obtain relationships between the coefficients by applying the boundary condition of continuity of the horizontal fields at each interface, then to solve the resultant set of simultaneous equations (Cagniard, 1953).

The surface impedance of a layered earth can be more easily calculated by using a simple transmission matrix, which relates the fields at the top and bottom of a layer of constant properties:

$$\begin{bmatrix} E' \\ H' \end{bmatrix}_{z'=z_0-\Delta z} = \begin{bmatrix} \cos(k_z \Delta z) & \frac{i\mu\omega}{k_z} \sin(k_z \Delta z) \\ \frac{ik_z}{\mu\omega} \sin(k_z \Delta z) & \cos(k_z \Delta z) \end{bmatrix} \begin{bmatrix} E \\ H \end{bmatrix}_{z=z_0} \quad 2.2-1$$

The 2 by 2 transmission matrix is equivalent to the matrizant for a layer of thickness  $\Delta z$  with a constant  $\sigma$ . By using the halfspace impedance at the lowest interface, this matrix can be successively applied upward to obtain the surface impedance.

Alternatively, an analytic formulation is possible for cases where the conductivity varies continuously with depth. For this formulation, Maxwell's equations can be

rearranged into a form also convenient for matrix method solutions. For the H horizontal polarization, where

$$H_y = H_z = E_x = 0, \text{ and } \frac{\partial}{\partial x} [ \quad ] = 0,$$

$$H_x \sim e^{\pm i(k_y y + k_z z)}$$

Maxwell's equations are

$$\frac{\partial H_x}{\partial z} = \sigma E_y \quad 2.2-2$$

$$\frac{\partial H_x}{\partial y} = -\sigma E_z \quad 2.2-3$$

$$\frac{\partial E_z}{\partial y} - \frac{\partial E_y}{\partial z} = i\omega\mu H_x \quad 2.2-4$$

By removing  $E_z$ ,

$$\frac{\partial E_y}{\partial z} = -i\omega\mu H_x + \frac{\partial}{\partial y} \left( -\frac{1}{\sigma} \frac{\partial H_x}{\partial y} \right) \quad 2.2-5$$

$$\frac{\partial E_y}{\partial z} = -i\omega\mu \left( 1 - \frac{k_y^2}{k^2} \right) H_x \quad 2.2-6$$

Equations 2.2-2 and 2.2-6 can be combined into a matrix formulation,

$$\frac{\partial}{\partial z} \begin{bmatrix} E_y \\ H_x \end{bmatrix} = \begin{bmatrix} 0 & -i\omega\mu \left( 1 - \frac{k_y^2}{k^2} \right) \\ \sigma & 0 \end{bmatrix} \begin{bmatrix} E_y \\ H_x \end{bmatrix} \quad 2.2-7$$

Analogously, the E horizontal polarization case can be represented as:

$$\frac{\partial}{\partial z} \begin{bmatrix} E_x \\ H_y \end{bmatrix} = \begin{bmatrix} 0 & i\mu\omega \\ -\sigma(1 - \frac{k_y^2}{k^2}) & 0 \end{bmatrix} \begin{bmatrix} E_x \\ H_y \end{bmatrix} \quad 2.2-8$$

For an expression directly in terms of the impedance,

$$\frac{\partial}{\partial z} \left( \frac{E}{H} \right) = \frac{1}{H} \frac{\partial E}{\partial z} - \frac{E}{H^2} \frac{\partial H}{\partial z} \quad 2.2-9$$

Thus, for the H horizontal polarization,

$$\frac{\partial}{\partial z} \left( \frac{E_y}{H_x} \right) = \frac{1}{H_x} \left( -i\mu\omega \left( 1 - \frac{k_y^2}{k^2} \right) H_x \right) - \frac{E_y}{H_x^2} \left( \sigma E_y \right) \quad 2.2-10$$

or

$$\frac{\partial}{\partial z} Z = -\sigma Z^2 - i\mu\omega \left( 1 - \frac{k_y^2}{k^2} \right) \quad 2.2-11$$

And, analogously, for the E horizontal polarization,

$$\frac{\partial}{\partial z} Z = \sigma \left( 1 - \frac{k_y^2}{k^2} \right) Z^2 + i\mu\omega \quad 2.2-12$$

Equations 2.2-11 and 2.2-12 are Riccati equations for the impedance.

Another method interprets the surface impedance of a layered earth as being analogous to the impedance of a non-uniform transmission line. This approach has been used previously by Madden (1966; Madden and Nelson, 1964; Madden and Thompson, 1965) and its influence permeates this entire thesis.

This transmission line analogy is motivated by the similarity between Maxwell's equations governing the orthogonal components of E and H and the transmission line equations governing current and voltage on a transmission line. This analogy emphasizes the role of the impedance as the important physical parameter relating E and H, and suggests that the cross-coupled first order partial differential equations are in a sense more basic than the derived uncoupled wave equation. The transmission line equations are

$$\frac{dV}{dz} = -ZI \quad 2.2-13$$

$$\frac{dI}{dz} = -YV \quad 2.2-14$$

or

$$\frac{d}{dz} \begin{bmatrix} V \\ I \end{bmatrix} = \begin{bmatrix} 0 & -Z \\ -Y & 0 \end{bmatrix} \begin{bmatrix} V \\ I \end{bmatrix} \quad 2.2-15$$

where  $Z$  is the series impedance per unit length and  $Y$  the shunt admittance per unit length. Combining equations 2.2-13 and 2.2-14 yields wave equations for  $V$  and  $I$ , with a propagation constant  $k$  given by

$$k^2 = -ZY \quad 2.2-16$$

The characteristic impedance is defined by

$$Z_c \equiv \sqrt{Z/Y} \quad 2.2-17$$

The basic analogy is between equations 2.2-15 and either 2.2-7 and 2.2-8. By associating  $E$  with  $V$  and  $H$  with  $I$ , or vice versa, the distributed circuit parameters of the equivalent transmission line are given in terms of the earth parameters involved. A lumped circuit approximation results which can be solved using standard network techniques. Note that the propagation constant and characteristic impedance are given by

$$k_z^2 = -ZY = j\omega\mu\sigma \left(1 - \frac{k_y^2}{k^2}\right) \quad 2.2-18$$

$$Z_c = \sqrt{Z/Y} = \sqrt{\frac{-j\omega\mu}{\sigma \left(1 - \frac{k_y^2}{k^2}\right)}} \text{ or } \sqrt{\frac{-j\omega\mu \left(1 - \frac{k_y^2}{k^2}\right)}{\sigma}} \quad 2.2-19$$

Although the transmission matrix of equation 2.2-1 was used to generate theoretical magnetotelluric apparent resistivity type-curves for multi-layered cases, the transmission-line analogy was developed and extended to a transmission-surface analogy for two-dimensional earth geometries. The maximum layer thickness restriction and the effect of thick layers on the surface impedance is discussed in Appendix 1.

Various authors (Cagniard, 1953; Yungel, 1961; and Wait, 1962) have presented two and three layer magnetotelluric type curves and discussed typical resolution problems such as that of a thin resistive layer.

### 2.3 Impedance of a spherically stratified conductor

Since the assumption of infinite horizontal wavelengths becomes less valid at low frequencies, while simultaneously the increased skin depth becomes a significant fraction of the earth's radius, it is desirable to calculate the impedance of a spherically stratified conductor for any given horizontal wavelength. Wait (1962) and Srivastava (1966) have approached this problem via the standard method of setting up wave solutions in spherical shells, then solving the resultant problem in terms of spherical Bessel functions. Complications in the evaluation of the Bessel functions limit the usefulness of this approach. However, the calculation of the impedance of a spherically stratified conductor is a good example of the transmission line analogy approach.

Solutions to the vector wave equation in spherical coordinates for a homogeneous region can be represented by a complete set of orthogonal vector solutions, designated as L, M, and N by Stratton (1941). The H and E fields can be completely represented by the M and N solutions:

$$H = \frac{1}{\mu} \sum_M \sum_m \left( a_{Mm} M_{Mm} + b_{Mm} N_{Mm} \right) \quad 2.3-1$$

$$E = \frac{i\omega}{k} \sum_M \sum_m \left( b_{Mm} M_{Mm} + a_{Mm} N_{Mm} \right) \quad 2.3-2$$



where

$$M_{MM} = \mp \frac{M}{\sin \theta} P_M^M \begin{Bmatrix} \sin M\phi \\ \cos M\phi \end{Bmatrix} S_M(kR) \vec{i}_\theta - \frac{\partial P_M^M}{\partial \theta} \begin{Bmatrix} \cos M\phi \\ \sin M\phi \end{Bmatrix} S_M(kR) \vec{i}_\phi \quad 2.3-3$$

$$\begin{aligned} N_{MM} &= M(M+1) P_M^M \begin{Bmatrix} \cos M\phi \\ \sin M\phi \end{Bmatrix} \frac{S_M(kR)}{kR} \vec{i}_r \\ &+ \frac{\partial P_M^M}{\partial \theta} \begin{Bmatrix} \cos M\phi \\ \sin M\phi \end{Bmatrix} \frac{1}{kR} \frac{\partial}{\partial R} [R S_M(kR)] \vec{i}_\theta \\ &\mp \frac{M}{\sin \theta} P_M^M \begin{Bmatrix} \sin M\phi \\ \cos M\phi \end{Bmatrix} \frac{1}{kR} \frac{\partial}{\partial R} [R S_M(kR)] \vec{i}_\phi \end{aligned} \quad 2.3-4$$

$S_M(kR)$  is the appropriate spherical function

The geomagnetic field can be separated into independent poloidal B (TE) and toroidal B (TM) modes:

$$\text{poloidal B} \quad B = \sum_{M=0}^{\infty} \sum_{m=1}^{\infty} b_{MM} N_{MM}, \quad E = \frac{i\omega}{k} \sum_{M=0}^{\infty} \sum_{m=1}^{\infty} b_{MM} M_{MM} \quad 2.3-5$$

$$\text{toroidal B} \quad B = \sum_{M=0}^{\infty} \sum_{m=1}^{\infty} a_{MM} M_{MM}, \quad E = \frac{i\omega}{k} \sum_{M=0}^{\infty} \sum_{m=1}^{\infty} a_{MM} N_{MM} \quad 2.3-6$$

Since the M solution possesses no radial component the above representation is consistent with no  $E_r$  in the poloidal B mode, no  $B_r$  in the toroidal B mode.

A discussion of the separation of the geomagnetic field into these two modes is included in a paper by Eckhart, Larner and Madden (1963). Physically, the

horizontal ionospheric electric currents, which are the primary generating sources for low-frequency geomagnetic energy, produce a predominantly poloidal B field. Moreover, the vertical electric field in the air that would be associated with a toroidal B mode diurnal variation is unrealistically large (Appendix 2).

Theoretically, the impedance for any harmonic of each mode is isotropic, a result implied by the spherical symmetry.

$$Z_{\text{poloidal B}}^{MM} = \frac{E_{\theta}}{H_{\phi}} = \frac{i\omega\mu}{k} \frac{kR S_m(kR)}{\frac{\partial}{\partial R} [R S_m(kR)]} = -\frac{E_{\phi}}{H_{\theta}} \quad 2.3-7$$

$$Z_{\text{toroidal B}}^{NM} = \frac{E_{\theta}}{H_{\phi}} = -\frac{i\omega\mu}{k} \frac{\frac{\partial}{\partial R} [R S_m(kR)]}{kR S_m(kR)} = -\frac{E_{\phi}}{H_{\theta}} \quad 2.3-8$$

However, even in a homogeneous medium, the impedance is not constant with depth since the geometry is constantly changing.

To use the transmission line analogy approach, a matrix formulation of Maxwell's equations for each harmonic of the poloidal B mode must be developed. In spherical co-ordinates, and with  $e^{-i\omega t}$  time dependence, Maxwell's equations expand into:

$$\frac{1}{r \sin \theta} \left[ \frac{\partial}{\partial \theta} (\sin \theta E_\phi) - \frac{\partial E_\theta}{\partial \phi} \right] = i\omega\mu H_r \quad 2.3-9$$

$$\frac{1}{r} \left[ -\frac{\partial}{\partial r} (r E_\phi) \right] = i\omega\mu H_\theta \quad 2.3-10$$

$$\frac{1}{r} \left[ \frac{\partial}{\partial r} (r E_\theta) \right] = i\omega\mu H_\phi \quad 2.3-11$$

and

$$\frac{1}{r} \left[ -\frac{\partial}{\partial r} (r H_\phi) + \frac{1}{\sin \theta} \frac{\partial H_r}{\partial \phi} \right] = \sigma E_\theta \quad 2.3-12$$

$$\frac{1}{r} \left[ \frac{\partial}{\partial r} (r H_\theta) - \frac{\partial H_r}{\partial \theta} \right] = \sigma E_\phi \quad 2.3-13$$

$$\left[ \frac{\partial}{\partial \theta} (\sin \theta H_\phi) - \frac{\partial H_\theta}{\partial \phi} \right] = 0 \quad 2.3-14$$

where  $E_r$  is zero in the poloidal B. mode. Equation 2.3-14 is consistent with the solutions of equations 2.3-3 through 2.3-5. Similarly from these solutions,

$$\frac{1}{\sin \theta} \frac{\partial H_r}{\partial \phi} = \left[ \frac{k}{i\mu\omega} \frac{m(m+1)}{kr^2} \right] (r E_\theta) \quad 2.3-15$$

$$\frac{\partial H_r}{\partial \theta} = \left[ -\frac{k}{i\mu\omega} \frac{m(m+1)}{kr^2} \right] (r E_\phi) \quad 2.3-16$$

With equation 2.3-15, equation 2.3-12 reduces to

$$\frac{\partial}{\partial r} (r H_\phi) = \left( \frac{m(m+1)}{i\mu\omega r^2} - \sigma \right) (r E_\theta) \quad 2.3-17$$

With equation 2.3-16, equation 2.3-13 reduces to

$$\frac{\partial}{\partial r} (r H_\theta) = \left( \sigma - \frac{m(m+1)}{i\mu\omega r^2} \right) (r E_\phi) \quad 2.3-18$$

Combining equations 2.3-10, 2.3-11, 2.3-17, and 2.3-18 to remove  $H_r$ , Maxwell's equations can be expressed as

$$\frac{\partial}{\partial r} \begin{bmatrix} r E_\phi \\ r H_\theta \\ r E_\theta \\ r H_\phi \end{bmatrix} = \begin{bmatrix} 0 & -i\mu\omega & 0 & 0 \\ \sigma - \frac{m(m+1)}{i\mu\omega r^2} & 0 & 0 & 0 \\ 0 & 0 & 0 & +i\mu\omega \\ 0 & 0 & \frac{m(m+1)}{i\mu\omega r^2} - \sigma & 0 \end{bmatrix} \begin{bmatrix} r E_\phi \\ r H_\theta \\ r E_\theta \\ r H_\phi \end{bmatrix} \quad 2.3-19$$

This 4x4 matrix uncouples into two independent polarizations with coefficient matrices differing only in sign. The difference in sign is due to  $Z^{mm} = \frac{E_\theta}{H_\phi} = -\frac{E_\phi}{H_\theta}$ , thus the impedance is isotropic, as indicated in equation 2.3-7.

The 2x2 relationships

$$\begin{bmatrix} r E \\ r H \end{bmatrix} = \pm \begin{bmatrix} 0 & i\mu\omega \\ \frac{m(m+1)}{i\mu\omega r^2} - \sigma & 0 \end{bmatrix} \begin{bmatrix} r E \\ r H \end{bmatrix} \quad 2.3-20$$

differ from the flat earth case in that  $\lambda E$  and  $\lambda H$  are the cross-coupled variables, rather than E and H, but the impedance is maintained as  $Z = \frac{\lambda E}{\lambda H} = \frac{E}{H}$ .

A Riccati equation for the impedance is easily derived from the equations 2.3-10 as

$$\frac{dZ}{d\lambda} = \left( \frac{k^2 \lambda^2 - M(M+1)}{i\omega\mu\lambda^2} \right) Z^2 + i\omega\mu \quad 2.3-21$$

A quirk in spherical geometry makes this equation, and equation 2.3-7 for the impedance, independent of m. Since m must be less than n, a large m requires a large n.

For reference, equation 2.2-15 for the flat-earth impedance case can be expressed as

$$\frac{dZ}{dz} = \left( \frac{k^2 - k_y^2}{i\mu\omega} \right) Z^2 + i\omega\mu \quad 2.3-22$$

The flat-earth long horizontal wavelength approximation,

$k^2 \gg k_y^2$  transforms in the spherical earth case to

$$k^2 = i\mu\omega\sigma \gg \frac{M(M+1)}{\lambda^2} \quad 2.3-23$$

This inequality will not hold for values of  $\lambda$  near the center of the earth. Due to the skin effect, however, only

very low frequency variations will penetrate deep enough in an earth with conductivity increasing with depth to be perturbed by the sphericity.

Transmission-line analogy formulation and solution

A transmission-line analogy calculation for the surface impedance follows directly from equation 2.3-20.

To make valid transmission-line associations, energy must be conserved. This restriction essentially normalizes the equivalent transmission line variables with length parameters and results in a non-uniform transmission line. For a spherical geometry.

$$\text{Energy flow} = VI^* = \iint (E \times H)_n dA = 4\pi r^2 EH \quad 2.3-24$$

Since  $rE$  and  $rH$  are the variables in equations 2.3-20 and since an impedance of  $E/H$  is desired, the appropriate associations are

$$I \iff \sqrt{4\pi} \quad rH \quad 2.3-25$$

$$V \iff \sqrt{4\pi} \quad rE \quad 2.3-26$$

With these associations, the distributed impedance and admittance expressions consistent with 2.3-20 and the transmission line equations are

$$Z = -i\omega\mu \quad 2.3-27$$

$$Y = \frac{i\omega\mu\sigma\lambda^2 - M(M+1)}{i\mu\omega\lambda^2} \quad 2.3-28$$

Note that

$$k^2 = i\omega\mu\sigma - \frac{M(M+1)}{\lambda^2} \quad 2.3-29$$

$$Z_c = \sqrt{\frac{-\omega^2\mu^2\lambda^2}{M(M+1) - i\omega\mu\sigma\lambda^2}} \quad 2.3-30$$

For calculation an equivalent network is constructed by sectioning a conductivity model into layers of thickness much smaller than a skin depth. Since the lumped impedance and the lumped admittance are proportional to the distance between nodes, the lumped parameters are

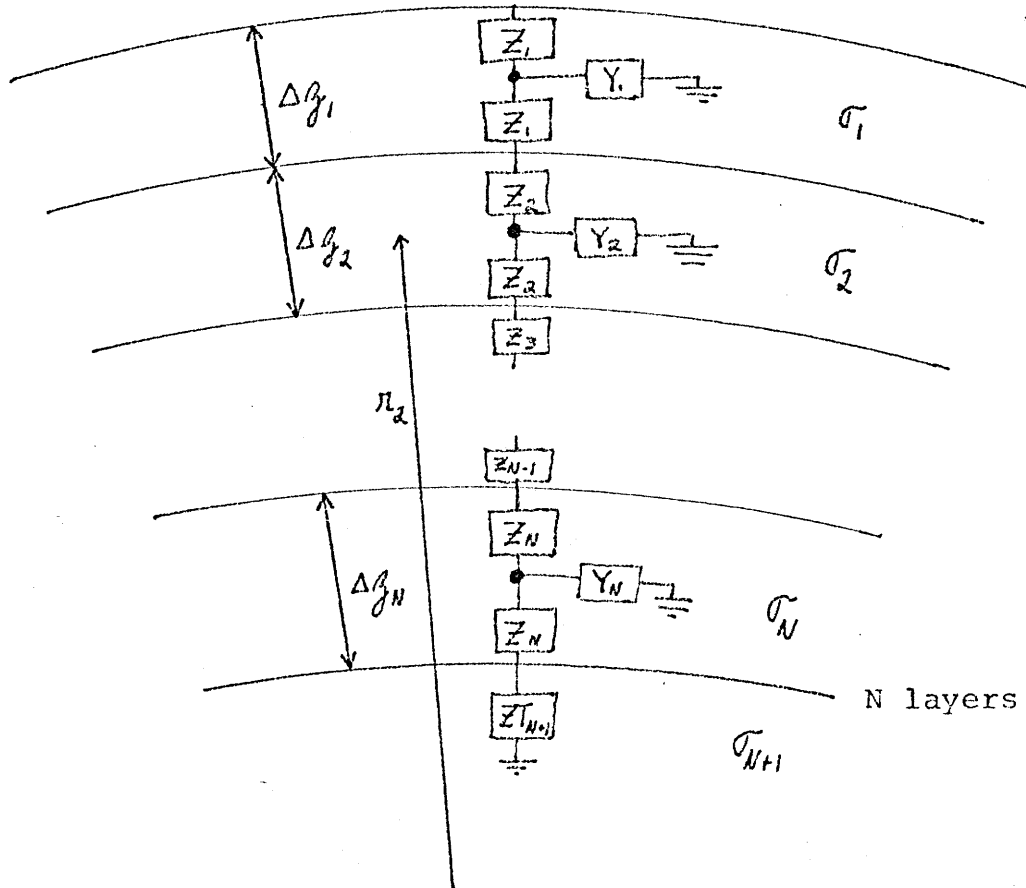
$$Z_{lumped} = -i\omega\mu \Delta \quad 2.3-31$$

$$Y_{lumped} = \left( \frac{i\omega\mu\sigma\lambda^2 - M(M+1)}{i\mu\omega\lambda^2} \right) \Delta \quad 2.3-32$$

where  $\Delta$  is the layer thickness. For thin layers far from the center of the sphere, the radius to the middle of the layer can be used for  $r$ . The terminal impedance is the characteristic impedance of the homogeneous inner sphere. This equivalent network is diagramed in Figure 2.2.

Using the Cantwell-McDonald earth conductivity profile (McDonald, 1957; Cantwell, 1960), which is plotted on Figure 2.3, a 320 layer model was solved for the surface impedance. Apparent resistivities and phases are given in Table 2.1 for a range of spherical harmonic orders and frequencies. For the non-physical zero order, the results are equivalent to the infinite horizontal wavelength flat-earth geometry and are given for comparison to show the effect of sphericity. The minimum wavelength, at which the estimated apparent resistivity differs by an arbitrary twenty per cent deviation criterion, is indicated in Table 2.1.





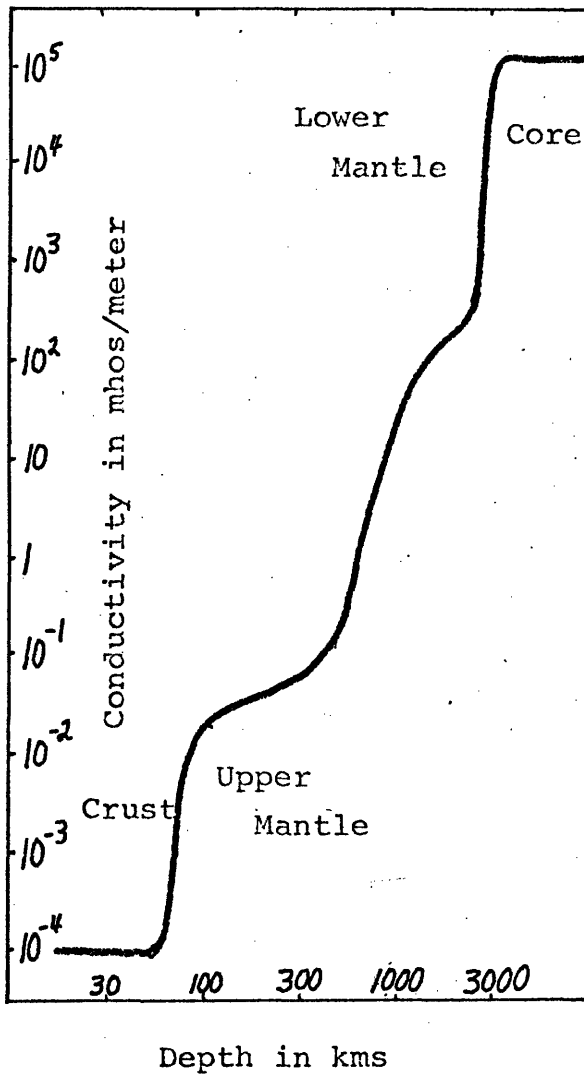
where:

$$Y_i = \left( \frac{i\omega\mu\sigma_i r_i^2 - m(m+1)}{i\omega\mu r_i^2} \right) \Delta z_i$$

$$Z_i = \frac{1}{2} (-i\omega\mu) \Delta z_i$$

$$Z_{N+1} = \sqrt{Z_{N+1}/Y_{N+1}}$$

Figure 2.2 Equivalent network for the spherically stratified conductor.



DEPTH (km)	CONDUCTIVITY (mhos/meter)
0	$1.0 \times 10^{-4}$
20	$1.0 \times 10^{-4}$
40	$1.0 \times 10^{-4}$
60	$1.0 \times 10^{-4}$
80	$.20 \times 10^{-1}$
100	$.22 \times 10^{-1}$
125	$.25 \times 10^{-1}$
150	$.28 \times 10^{-1}$
200	$.32 \times 10^{-1}$
300	$.42 \times 10^{-1}$
400	$.50 \times 10^{-1}$
600	.10
700	.50
800	$.30 \times 10^1$
900	$.10 \times 10^2$
1000	$.20 \times 10^2$
1500	$.30 \times 10^2$
2000	$.60 \times 10^2$
2500	$.12 \times 10^3$
2850	$.20 \times 10^3$
2898	$1.0 \times 10^5$

Figure 2.3 Cantwell-McDonald conductivity model

MAGNETOTELLURIC APPARENT RESISTIVITIES  
FOR SPHERICALLY STRATIFIED EARTH FOR VARIOUS SPHERICAL MODE ORDERS  
CANTWELL-MCDONALD CONDUCTIVITY MODEL

FREQ		RESISTIVITIES IN OHM-METERS							
IN CPS	N= 0	1	2	4	9	18	36	100	
1.00E-07	.12E 01	.11E 01	.10E 01	.76E 00	.31E 00	.89E-01	.23E-01	.32E-02	
.14E-06	.14E 01	.13E 01	.13E 01	.95E 00	.4CE 00	.12E 00	.32E-01	.44E-02	
.19E-06	.22E 01	.2 E 01	.18E 01	.14E 01	.59E 00	.17E 00	.46E-01	.61E-02	
.27E-06	.24E 01	.24E 01	.22E 01	.17E 01	.77E 00	.23E 00	.63E-01	.84E-02	
.37E-06	.34E 01	.33E 01	.31E 01	.24E 01	.11E 01	.34E 00	.88E-01	.12E-01	
.52E-06	.42E 01	.4CE 01	.39E 01	.31E 01	.14E 01	.45E 00	.12E 00	.16E-01	
.72E-06	.55E 01	.53E 01	.50E 01	.41E 01	.21E 01	.64E 00	.17E 00	.23E-01	
1.00E-06	.71E 01	.68E 01	.64E 01	.53E 01	.27E 01	.88E 00	.23E 00	.32E-01	
.14E-05	.87E 01	.88E 01	.82E 01	.69E 01	.37E 01	.12E 01	.33E 00	.44E-01	
.19E-05	.12E 02	.11E 02	.11E 02	.92E 01	.50E 01	.17E 01	.46E 00	.61E-01	
.27E-05	.14E 02	.14E 02	.13E 02	.12E 02	.66E 01	.23E 01	.63E 00	.84E-01	
.37E-05	.17E 02	.16E 02	.16E 02	.14E 02	.86E 01	.32E 01	.86E 00	.12E 00	
.52E-05	.21E 02	.2 E 02	.19E 02	.18E 02	.12E 02	.44E 01	.12E 01	.16E 00	
.72E-05	.25E 02	.25E 02	.24E 02	.22E 02	.15E 02	.61E 01	.17E 01	.23E 00	
1.00E-05	.28E 02	.28E 02	.27E 02	.25E 02	.18E 02	.82E 01	.23E 01	.31E 00	
.14E-04	.34E 02	.34E 02	.34E 02	.32E 02	.24E 02	.11E 02	.33E 01	.44E 00	
.19E-04	.38E 02	.38E 02	.38E 02	.36E 02	.29E 02	.15E 02	.45E 01	.61E 00	
.27E-04	.42E 02	.42E 02	.41E 02	.40E 02	.34E 02	.20E 02	.63E 01	.85E 00	
.37E-04	.44E 02	.45E 02	.44E 02	.43E 02	.38E 02	.25E 02	.85E 01	.12E 01	
.52E-04	.49E 02	.49E 02	.49E 02	.48E 02	.44E 02	.31E 02	.12E 02	.16E 01	
.72E-04	.53E 02	.53E 02	.53E 02	.52E 02	.49E 02	.38E 02	.16E 02	.23E 01	
1.00E-04	.59E 02	.59E 02	.59E 02	.58E 02	.55E 02	.45E 02	.21E 02	.31E 01	
.14E-03	.65E 02	.65E 02	.64E 02	.64E 02	.62E 02	.53E 02	.28E 02	.44E 01	
.19E-03	.73E 02	.72E 02	.72E 02	.72E 02	.7CE 02	.61E 02	.37E 02	.61E 01	
.27E-03	.82E 02	.81E 02	.81E 02	.81E 02	.79E 02	.71E 02	.47E 02	.84E 01	
.37E-03	.93E 02	.93E 02	.92E 02	.92E 02	.89E 02	.82E 02	.58E 02	.12E 02	
.52E-03	.11E 03	.11E 03	.11E 03	.11E 03	.1CE 03	.96E 02	.72E 02	.16E 02	
.72E-03	.12E 03	.12E 03	.12E 03	.12E 03	.12E 03	.11E 03	.88E 02	.22E 02	
1.00E-03	.14E 03	.14E 03	.14E 03	.14E 03	.14E 03	.13E 03	.11E 03	.31E 02	
.14E-02	.17E 03	.17E 03	.17E 03	.17E 03	.17E 03	.16E 03	.13E 03	.42E 02	
.19E-02	.21E 03	.21E 03	.21E 03	.21E 03	.2CE 03	.19E 03	.17E 03	.57E 02	
.27E-02	.25E 03	.25E 03	.25E 03	.25E 03	.25E 03	.24E 03	.20E 03	.78E 02	
.37E-02	.31E 03	.31E 03	.31E 03	.31E 03	.31E 03	.30E 03	.26E 03	.10E 03	
.52E-02	.38E 03	.38E 03	.38E 03	.38E 03	.38E 03	.37E 03	.32E 03	.14E 03	
.72E-02	.48E 03	.48E 03	.48E 03	.48E 03	.48E 03	.46E 03	.41E 03	.19E 03	
1.00E-02	.61E 03	.61E 03	.61E 03	.61E 03	.61E 03	.59E 03	.53E 03	.25E 03	

FREQ		IMPEDANCE PHASE IN DEGREES							
IN CPS	N= 0	1	2	4	9	18	36	100	
1.00E-07	-78.9	-79.5	-80.5	-83.4	-88.3	-89.9	-90.0	-90.0	
.14E-06	-75.7	-80.2	-80.9	-83.5	-88.2	-89.9	-90.0	-90.0	
.19E-06	-78.7	-79.5	-80.4	-82.9	-87.9	-89.8	-90.0	-90.0	
.27E-06	-75.4	-79.7	-80.7	-83.0	-87.6	-89.7	-90.0	-90.0	
.37E-06	-78.8	-79.2	-79.9	-82.2	-87.3	-89.7	-90.0	-90.0	
.52E-06	-78.6	-79.0	-79.6	-81.9	-86.9	-89.6	-90.0	-90.0	
.72E-06	-77.8	-78.2	-79.0	-81.1	-86.3	-89.4	-89.9	-90.0	
1.00E-06	-76.9	-77.3	-78.1	-80.3	-85.7	-89.2	-89.9	-90.0	
.14E-05	-76.0	-76.2	-77.0	-79.2	-84.9	-89.0	-89.9	-90.0	
.19E-05	-74.4	-74.8	-75.6	-77.7	-83.9	-88.7	-89.8	-90.0	
.27E-05	-73.1	-73.3	-74.4	-76.3	-82.7	-88.2	-89.8	-90.0	
.37E-05	-71.6	-72.0	-72.6	-74.7	-81.3	-87.7	-89.7	-90.0	
.52E-05	-65.6	-70.0	-70.8	-72.7	-79.5	-87.0	-89.6	-90.0	
.72E-05	-67.5	-67.6	-68.5	-70.4	-77.4	-86.0	-89.4	-90.0	
1.00E-05	-66.2	-66.4	-66.9	-68.7	-75.5	-84.8	-89.2	-90.0	
.14E-04	-63.7	-63.8	-64.1	-65.9	-72.8	-83.2	-88.9	-90.0	
.19E-04	-61.7	-61.8	-62.3	-64.0	-70.3	-81.3	-88.4	-90.0	
.27E-04	-60.6	-60.7	-61.1	-62.5	-68.0	-79.2	-87.9	-89.9	
.37E-04	-60.2	-60.2	-60.8	-61.7	-66.5	-77.0	-87.1	-89.9	
.52E-04	-55.5	-59.5	-59.9	-60.7	-64.6	-74.5	-86.1	-89.9	
.72E-04	-59.8	-60.0	-60.1	-60.8	-63.8	-72.4	-84.8	-89.8	
1.00E-04	-60.2	-60.2	-60.3	-60.9	-63.5	-70.6	-83.3	-89.8	
.14E-03	-61.0	-61.0	-61.2	-61.5	-63.4	-69.4	-81.6	-89.7	
.19E-03	-61.7	-61.8	-61.8	-62.2	-63.7	-68.5	-79.9	-89.6	
.27E-03	-62.7	-62.8	-62.9	-63.1	-64.3	-68.1	-78.2	-89.4	
.37E-03	-63.9	-63.9	-64.0	-64.2	-65.2	-68.3	-77.0	-89.2	
.52E-03	-65.3	-65.3	-65.3	-65.4	-66.1	-68.6	-76.0	-88.9	
.72E-03	-66.5	-66.5	-66.5	-66.7	-67.3	-69.3	-75.4	-88.5	
1.00E-03	-68.0	-68.0	-68.0	-68.1	-68.5	-70.1	-75.2	-88.1	
.14E-02	-65.3	-69.4	-69.4	-69.5	-69.8	-71.1	-75.3	-87.6	
.19E-02	-70.8	-70.8	-70.8	-70.9	-71.1	-72.2	-75.6	-87.1	
.27E-02	-72.2	-72.3	-72.3	-72.3	-72.5	-73.3	-76.2	-86.6	
.37E-02	-73.5	-73.5	-73.5	-73.5	-73.7	-74.4	-76.8	-86.2	
.52E-02	-74.8	-74.8	-74.8	-74.9	-75.1	-75.6	-77.6	-85.9	
.72E-02	-76.0	-76.0	-76.0	-76.0	-76.2	-76.6	-78.3	-85.7	
1.00E-02	-77.1	-77.1	-77.1	-77.1	-77.2	-77.6	-79.0	-85.6	

Table 2.1

## 2.4 Magnetotelluric relationships for a two-dimensional geometry

Because layered-media magnetotelluric interpretation is not appropriate for the many geologically interesting features where the conductivity structure is not horizontally layered, magnetotelluric theory must be extended to include inhomogeneous structures.

To see how the qualitative behavior of the impedance over a simple two-dimensional feature can be obtained just by the application of boundary conditions, consider the vertical contact shown in Figure 2.4. At a far distance from the contact on either side the impedance should be the appropriate isotropic value. Near the contact, the field components perpendicular to the contact are distorted due to re-adjustment required by the skin effect, causing vertical components. At the contact, the following boundary conditions must hold

$H_{\perp}$  continuous

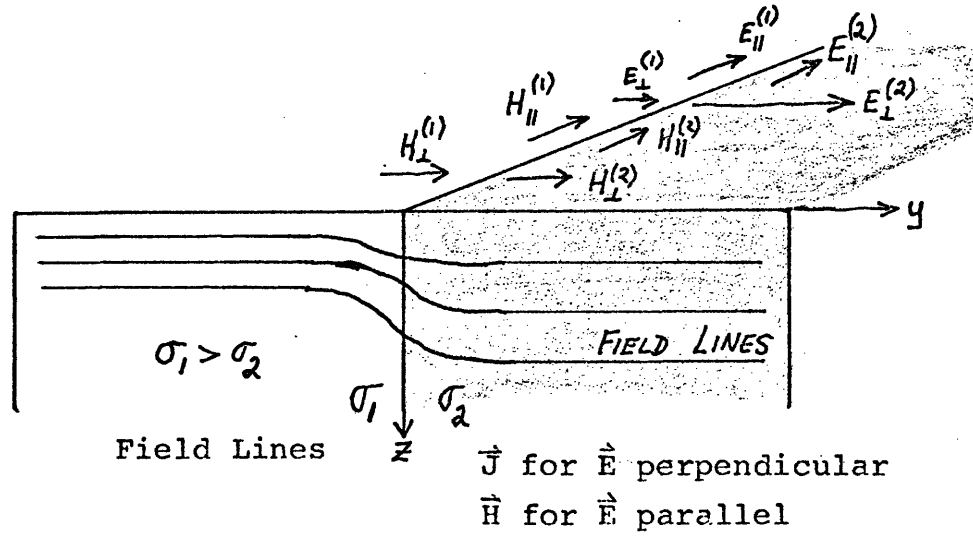
$H_{\parallel}$  continuous

$E_{\parallel}$  continuous

$J_{\perp}$  continuous

From current continuity, the boundary condition on  $E_{\perp}$  is

Electromagnetic Field Relationships



Apparent Resistivity Profile

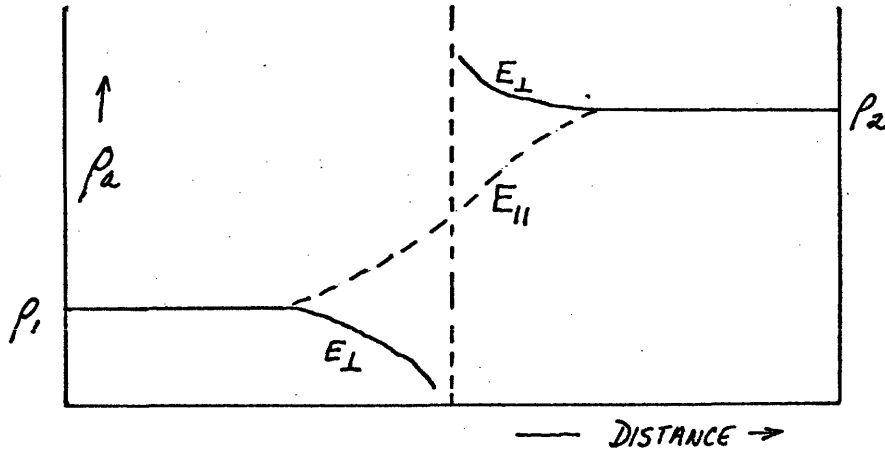


Figure 2.4 Electromagnetic fields over a lateral conductivity contrast.

$$E_{\perp}^{(1)} = \frac{\sigma_2}{\sigma_1} E_{\perp}^{(2)} \quad 2.4-1$$

Only  $E_{\perp}$  is discontinuous. Therefore, there will be a discontinuity in the apparent resistivity for the E perpendicular polarization ( $E_{\perp}/H_{\parallel}$ ), of magnitude  $(\sigma_1/\sigma_2)^2$ . This effect can be seen qualitatively in Figure 2.4. On the resistive side, greater current density near the contact increases  $E_{\perp}^{(2)}$  and, hence, increases  $\rho_a$  above  $\rho_2$ . On the conductive side, lower current density near the contact decreases  $E_{\perp}^{(1)}$  and, hence, decreases  $\rho_a$  below  $\rho_1$ . The behavior of the apparent resistivity, which is also shown on Figure 2.4, indicates that the E perpendicular apparent resistivity is more diagnostic of the contact.

For a magnetic field perpendicular to the contact, more current in the conductive side introduces a vertical magnetic field. This effect is observed in geomagnetic coast effect studies, in which Parkinson vectors (defined to be in the horizontal direction where there is maximum coherency between the horizontal and vertical magnetic fields) point toward the nearest coast (Parkinson, 1962).

#### Maxwell's Equations formulation

The geometry of Figure 2.4, with the x-axis the strike

direction of two-dimensionality, is now used for a convenient formulation of Maxwell's equations. The source field is assumed to vary as  $e^{ik_x x}$  along strike; any horizontal variations in the  $y$ -direction can be included in the boundary conditions.

For the E perpendicular polarizations,  $E_x = 0$ , and Maxwell's equations reduce to:

From  $\nabla \times E = -\frac{\partial B}{\partial t}$

$$\frac{\partial E_z}{\partial y} - \frac{\partial E_y}{\partial z} = i\mu\omega H_x \quad 2.4-2$$

$$H_y = \frac{-k_x}{\mu\omega} E_z \quad 2.4-3$$

$$H_z = \frac{k_x}{\mu\omega} E_y \quad 2.4-4$$

From  $\nabla \times H = J$

$$\frac{\partial H_z}{\partial y} - \frac{\partial H_y}{\partial z} = 0 \quad 2.4-5$$

$$\frac{\partial H_x}{\partial z} - ik_x H_z = \sigma E_y \quad 2.4-6$$

$$ik_x H_y - \frac{\partial H_x}{\partial y} = \sigma E_z \quad 2.4-7$$

Using 2.4-3 and 2.4-4 to remove  $H_y$  and  $H_z$ , equations 2.4-6 and 2.4-7 reduce to

$$\frac{\partial H_x}{\partial z} = \left( \sigma + \frac{ik_x^2}{\mu\omega} \right) E_y \quad 2.4-8$$

$$\frac{\partial H_x}{\partial y} = - \left( \sigma + \frac{ik_x^2}{\mu\omega} \right) E_z \quad 2.4-9$$

Therefore, equations 2.4-2, 2.4-8 and 2.4-9 represent a set of equations for  $E_y$ ,  $E_z$  and  $H_x$ .

$$\begin{cases} \frac{\partial E_z}{\partial y} - \frac{\partial E_y}{\partial z} = i\mu\omega H_x & 2.4-10a \\ \frac{\partial H_x}{\partial z} = \sigma \left( 1 - \frac{k_x^2}{k^2} \right) E_y & 2.4-10b \\ \frac{\partial H_x}{\partial y} = -\sigma \left( 1 - \frac{k_x^2}{k^2} \right) E_z & 2.4-10c \end{cases}$$

E perpendicular

Analogously for the H perpendicular polarization where  $H_x = 0$ , Maxwell's equations reduce to a set of equations for  $E_x$ ,  $H_y$  and  $H_z$ .

$$\begin{cases} \frac{\partial H_z}{\partial y} - \frac{\partial H_y}{\partial z} = \sigma E_x & 2.4-11a \\ \frac{\partial E_x}{\partial z} = i\mu\omega \left( 1 - \frac{k_x^2}{k^2} \right) H_y & 2.4-11b \\ \frac{\partial E_x}{\partial y} = -i\mu\omega \left( 1 - \frac{k_x^2}{k^2} \right) H_z & 2.4-11c \end{cases}$$

H perpendicular

For long horizontal wavelengths,  $k_x = 0$  and these polarizations completely separate into two polarizations



which are characterized by mutually orthogonal field components. Note that the E perpendicular polarization ( $E_y, H_x, E_z$ ) has an associated vertical electric field, whereas the H perpendicular, or E parallel, polarization ( $E_x, H_y, H_z$ ) has an associated vertical magnetic field. For a zero conductivity air layer, equation 2.4-10c shows that the surface horizontal magnetic field is constant for the E perpendicular polarization. Analytic solutions have been obtained for this polarization for simple geometries (d'Erceville and Kunetz, 1962; Rankin, 1962; and Weaver, 1963).

For the E parallel case, the air must be included in the solution. This complication hinders analytic solution for this polarization.

#### Transmission-surface analogy formulation

Numerical solution of equations 2.4-10 or 2.4-11 for an arbitrary two-dimensional conductivity surface requires first the discrete approximation of the equations and of the continuous cross-section by a finite grid. Neves (1957) used a finite difference approach on the wave equation (actually a Helmholtz equation). This thesis uses a transmission-surface analogy to represent the continuous conductivity

cross-section as an equivalent transmission surface (Slater, 1942), then uses network solution techniques on the lumped-circuit approximation.

The one-dimensional transmission line equations of equation 2.2-15 can be extended for a two-dimensional transmission surface to

$$\begin{cases} \frac{dV}{dz} = -Z I \\ \frac{dI}{dz} = -Y V \end{cases} \Rightarrow \begin{cases} \text{grad } V = -Z I \\ \text{div } I = -Y V \end{cases} \quad 2.4-12$$

where  $V = \text{volts}$

$I = \text{amps}$

$Y = \text{admittance/meter}$

$Z = \text{impedance/meter}$

where  $V = \text{volts}$

$I = \text{amps/meter}$

$Y = \text{admittance/meter}^2$

$Z = \text{impedance}$

These expand into component equations which are similar in form to equations 2.4-10 and equations 2.4-11

$$\frac{\partial I_y}{\partial y} + \frac{\partial I_z}{\partial z} = -Y V \quad 2.4-13a$$

$$\frac{\partial V}{\partial z} = -Z I_z \quad 2.4-13b$$

$$\frac{\partial V}{\partial y} = -Z I_y \quad 2.4-13c$$

The necessary associations are motivated by noting that for each polarization one field component is linearly polarized in the strike direction, so it can be represented as the scalar quantity in the network - the voltage.

For the E perpendicular case, the energy conservation condition requires

$$VI_z \Delta y = -E_y H_x \Delta x \Delta y \quad 2.4-14$$

$$VI_y \Delta z = +E_z H_x \Delta x \Delta z \quad 2.4-15$$

The associations are

$$\begin{aligned} E_y & \langle \Rightarrow \rangle -I_z \\ E_z & \langle \Rightarrow \rangle I_y \\ H_x & \langle \Rightarrow \rangle V \end{aligned} \quad 2.4-16$$

where  $\Delta x$  can be absorbed by making all parameters per unit length in the strike direction. Note that the components of E are equivalent to different geometrical components of I. The distributed parameters are obtained by comparing equation 2.4-10 and 2.4-13, as

$$\begin{aligned} Z &= \sigma \left( 1 - \frac{k_x^2}{k^2} \right) \\ Y &= -i\omega\mu \end{aligned} \quad 2.4-17$$

This represents a transmission surface with resistive impedances between nodes and capacitive admittances to ground.

For the air, the distributed impedance is zero since the conductivity is negligible. Therefore, the voltage must be constant along the line in the network representing the earth's surface. This restriction on the network is consistent with the  $H_x = \text{constant}$  boundary condition.

The H perpendicular polarization network is characterized by the following associations and distributed parameters

$$\begin{aligned} E_x &\langle \Rightarrow \rangle V \\ H_y &\langle \Rightarrow \rangle I_z \\ H_z &\langle \Rightarrow \rangle -I_y \end{aligned} \qquad 2.4-18$$

plus

$$Z = -i\mu\omega \left(1 - \frac{k_x^2}{k^2}\right) \qquad 2.4-19$$

$$Y = \sigma \qquad 2.4-20$$

This represents a transmission surface with inductive impedances between nodes and resistive admittances to ground. Therefore, the equivalent networks for the two polarizations are both low-pass systems as required by electromagnetic propagation in the earth.

Because long horizontal wavelengths were not indicated in the observed fields,  $k_x = 0$  was assumed in the calculations.

Although the E parallel expressions appear to resemble those for the E perpendicular polarization, significant difficulties arise in applying boundary conditions. Whereas in the E perpendicular case the air above the earth could be ignored because of the infinite impedance contrast, in the E parallel case the air layer is modeled by a sheet of inductances and the currents couple across the boundary. The horizontal magnetic field in the air is independent of the conductivity of a layered earth. Moreover, for an air layer sufficiently thick, any perturbations in this magnetic field component caused by two-dimensional conductivity structure are smoothed out by the Laplace equation solutions for the air layer. Thus, because it is constant far from regions of laterally inhomogeneous conductivity structure, the horizontal magnetic field can be thought of as a source. In other words, the air layer of inductances must be thick enough to present a constant impedance to the source.

#### Network solution for theoretical apparent resistivities

To form a network, the two-dimensional earth model must

be sectioned into a grid of rectangles and the lumped circuit parameters must be determined. The grid spacing must be chosen smaller than a wavelength within each block, as discussed in Appendix 1. Note that this spacing restriction changes with each frequency considered. Although this restriction would appear to limit the complexity of the model, the long wavelengths in air allow the air layer to be modeled by only a few thick spacings, and the use of logarithmically increasing spacing with depth allows one model to be applicable for a wide range of frequencies.

Since the lumped impedance is proportional to the distance between nodes and inversely proportional to the width of surface associated with the nodes, the vertical and horizontal impedances will be different for arbitrary grid spacing. The lumped admittance is proportional to the area of surface. These parameters are defined as

$$\text{vertical impedance, } ZV_{ij} \equiv Z \Delta z_i / \Delta y_j \quad 2.4-21$$

$$\text{horizontal impedance, } ZH_{ij} \equiv Z \Delta y_j / \Delta z_i \quad 2.4-22$$

$$\text{admittance, } Y_{ij} \equiv Y \Delta y_j \Delta z_i \quad 2.4-23$$

where  $Z, Y$  = distributed parameters

$\Delta z_i$  = vertical spacing between nodes

$\Delta y_j$  = horizontal spacing between nodes

$i = 1, \dots, N$   $j = 1, \dots, M$  for an  $N$  by  $M$  grid

The lumped terminal impedances are calculated from the characteristic impedance by

$$ZT_j \equiv \sqrt{Z/Y} / \Delta y_j = \sqrt{\frac{ZV_{Nj}}{Y_{Nj}}} \quad 2.4-24$$

where the conductivities along the bottom layer are taken to extend to infinity. The use of this terminal impedance, which assumes  $k_x = 0$ , is strictly correct only when the diffraction effects at depth are relatively slight.

The actual circuit elements depend upon whether the nodes are placed at the corners or in the centers of the rectangles of the grid. The circuit impedance between two nodes placed in the centers of two adjoining rectangles is the series combination of the lumped impedances (equation 2.4-21 or 2.4-22) for the two rectangles. For two nodes at the corners within the grid, the circuit impedance is the parallel combination of the lumped impedances on either side of the line connecting the nodes. The better choice is to place the nodes at the corners within the grid so that the boundary values can be directly determined.

To establish boundary conditions for the network, an arbitrary constant source is applied to the top of the grid. For E perpendicular, a constant voltage models  $H_x$  constant

at  $z = 0$ . For  $E$  parallel, a constant vertical current models  $H_y$  constant at the top of the air layer. A one-dimensional transmission line problem was solved for both sides to obtain voltage boundary values to force upon the two-dimensional solution. Therefore, the ends of the model should be far enough away from the non-horizontally layered features so that the impedance is isotropic.

For a numerical solution, the equation of current continuity

$$\sum^4 \frac{V_{\text{neighboring}} - V_{ij}}{Z_{\text{connecting}}} + Y_{ij} V_{ij} = S'_{ij} \quad 2.4-25$$

produces a  $(M \times N) \times (M \times N)$  coefficient matrix which is a very sparse, diagonally dominant, normal matrix. Relaxation techniques can be applied to such problems, but the theory is not developed for this case where the coefficient matrix is non-Hermitian. Although the relaxation solution will converge, the eigenvalues of the coefficient matrix are complex and the over-relaxation parameter for the optimum rate of convergence must be determined empirically. However, a direct solution for such coefficient matrices, which does not involve a  $(M \times N)$  by  $(M \times N)$  matrix inversion, has been developed by Greenfield (1965) and was used in this thesis.



Computational details are included in Appendix 3. Finally, theoretical apparent resistivities at the earth's surface are calculated from the solution values of V and I using the appropriate associations.

Example - theoretical apparent resistivities over a vertical contact

Figures 2.5 and 2.6 show theoretical field relationships for the simplest two dimensionality, a vertical contact, calculated for the equivalent networks for the two polarizations. The behavior of the apparent resistivities is consistent with the earlier qualitative discussion in that the E perpendicular apparent resistivity includes a discontinuity of  $(\sigma_1/\sigma_2)^2$  and the E parallel results are continuous. Note that the E-H phases do not vary markedly from  $-45^\circ$ . Greater phase shifts result where the apparent resistivity is a more rapidly changing function of frequency, as is the case for large conductivity contrasts in horizontally layered media.

Figure 2.5 compares the results of the network solution with the analytic solution of d'Erceville and Kunetz (1962) for the E perpendicular polarization over a vertical contact with a 100:1 conductivity contrast.

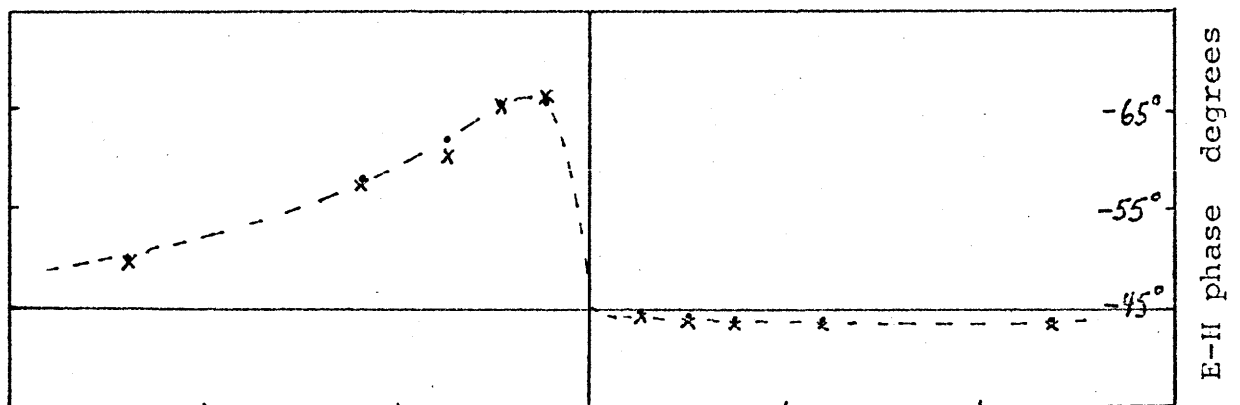
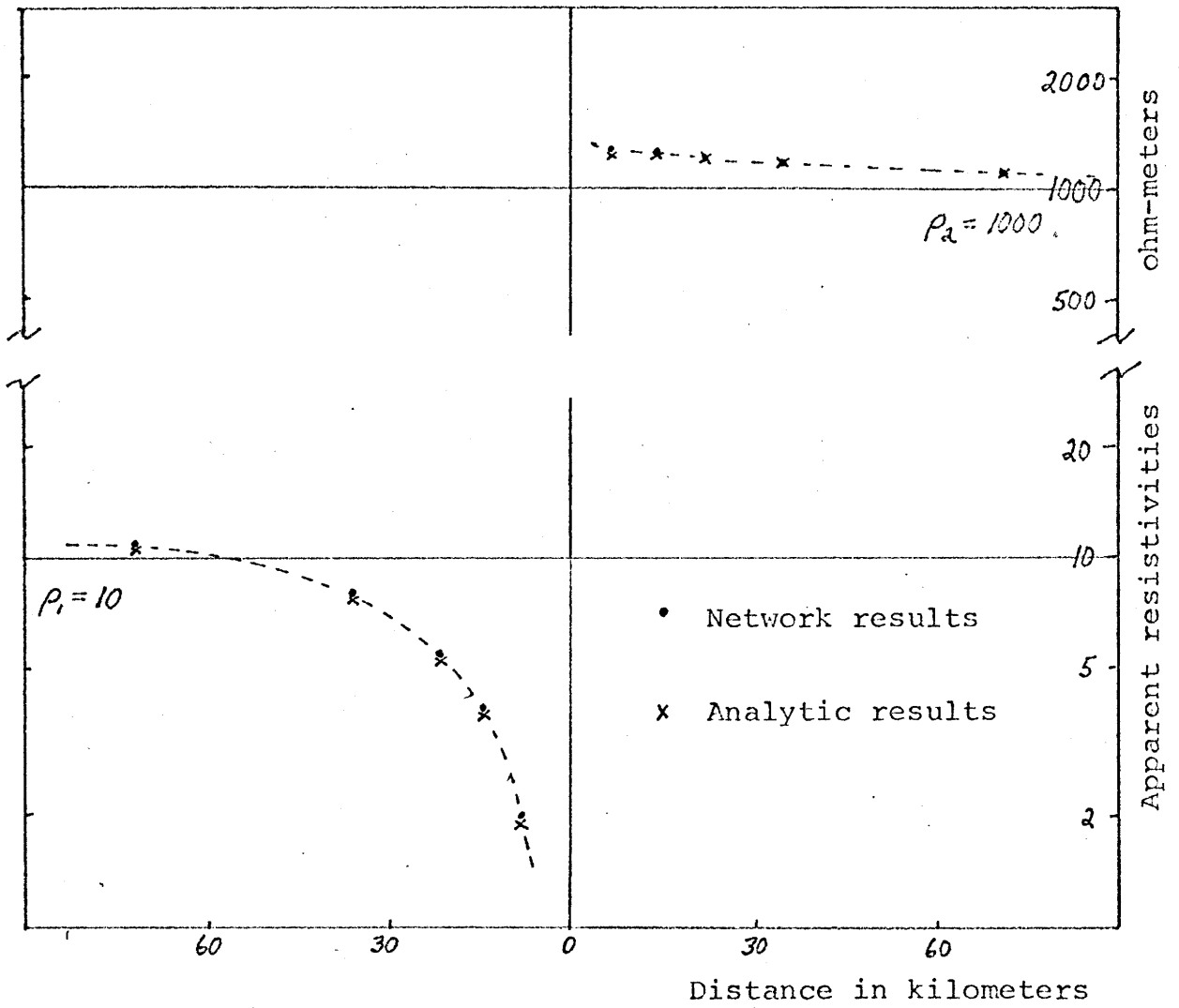
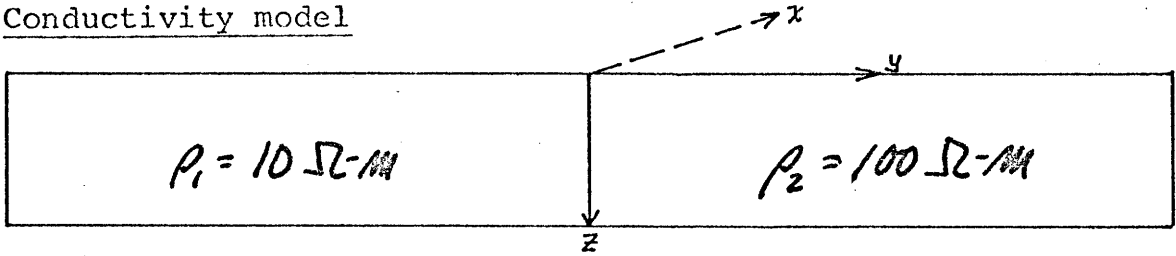


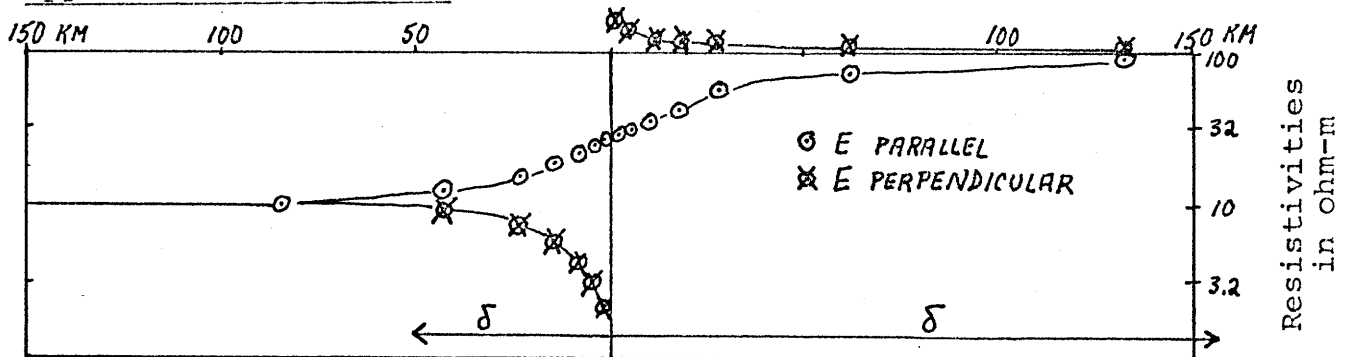
Figure 2.5 Comparison of theoretical apparent resistivities calculated by network solution and by analytic solution (d'Erceville and Kunetz, 1962) over a vertical contact. Conductivity contrast is 100:1. Frequency is  $10^{-3}$  cps.

Conductivity model

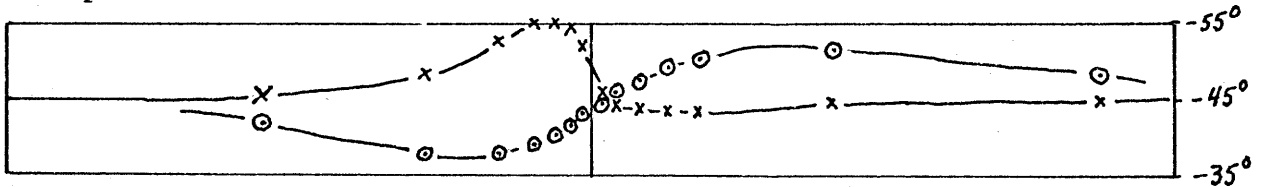


For frequency =  $10^{-3}$  cps

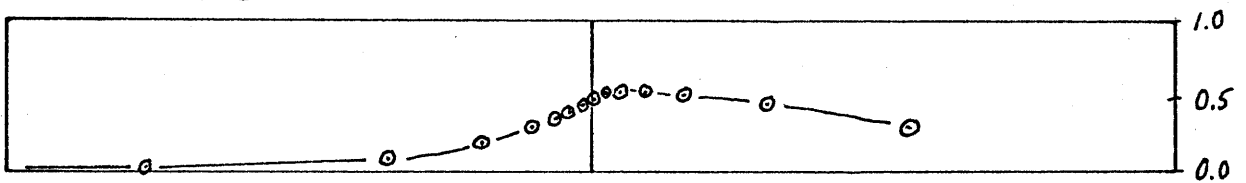
Apparent resistivities



E-H phase



H vertical/Hy



Hx (relative to value far from contact)

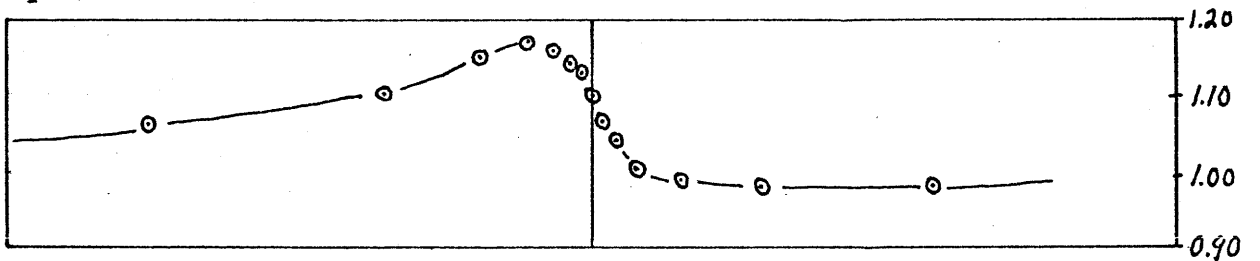


Figure 2.6 Theoretical magnetotelluric field relationships over a vertical contact.

Figure 2.6 shows the theoretical apparent resistivities, the E-H phases, the ratio  $H_{\text{vertical}}/H_y$ , and the variation of  $H_y$  over a vertical contact with a 10:1 conductivity contrast. The skin depth appropriate for each side is included to indicate its usefulness as a "range of influence" parameter.

The variation of the  $H_{\text{vertical}}/H_{\text{perpendicular}}$  ratio is the magnetic induction method indication of a lateral contrast in conductivity. Note that the delineation of the contact is much better defined by the E perpendicular apparent resistivity. Moreover, this variation, for a ocean-continent boundary model, exhibits the well-known coast effect of a more extensive  $H_{\text{vertical}}/H_{\text{perpendicular}}$  anomaly over the resistive (continental) side.

The variation of  $H_{\text{perpendicular}}$  over the contact is plotted to show the relatively small variation in the magnetic field over a laterally inhomogeneous conductivity structure. It should be emphasized that the two lower curves, for  $H_{\text{vertical}}$  and  $H_{\text{perpendicular}}$ , are for the E parallel polarization only; the magnetic field is constant for the E perpendicular polarization.

## 2.5 Properties of the magnetotelluric impedance tensor

To explain peculiar magnetotelluric field results in which the Cagniard apparent resistivities are not independent of the measured orthogonal fields or the time of measurement, the impedance must be expressed as a tensor, as formulated by Cantwell (1960):

$$\begin{bmatrix} E_x \\ E_y \end{bmatrix} = \begin{bmatrix} Z_{11} & Z_{12} \\ Z_{21} & Z_{22} \end{bmatrix} \begin{bmatrix} H_x \\ H_y \end{bmatrix} \quad 2.5-1$$

The admittance formulation, defined by  $H_i = Y_{ij}E_j$ , is mathematically equivalent to the impedance formulation, but the impedance is more commonly used because the more uniform magnetic field can be thought of as a source.

Therefore, the electric field in one direction may depend on magnetic field variations parallel to, as well as perpendicular to, its direction. Therefore, "Cagniard apparent resistivities" calculated from raw ratios  $E_x/H_y$  or  $E_y/H_x$  can vary with time as the polarization of the source field varies. As long as the source field wavelengths are sufficiently long, however, the tensor elements should be time-invariant.

Since  $Z_{12}$  and  $Z_{21}$  can be calculated for a given two-dimensional conductivity structure, magnetotelluric data

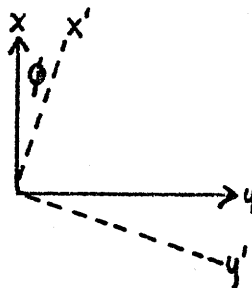
can be interpreted quantitatively if the geologic structure involved is two-dimensional and if the elements for the tensor aligned with the structure can be calculated from the data. A structure can be considered two-dimensional if a conductivity cross-section is constant along a strike direction for a distance much longer than a skin depth.

Therefore, two-dimensional tensor impedance analysis of magnetotelluric data consists of three steps: first the calculation of the impedance tensor with respect to the measuring axes, then the rotation of this tensor into the principal axes, and finally, the comparison of apparent resistivities calculated from the rotated tensor with theoretical two-dimensional results.

#### Properties of theoretical impedance tensors

Properties of theoretical impedance tensors can be obtained through matrix analysis. Complications arise because Maxwell's equations couple together the orthogonal components of E and H and, hence, the off-diagonal elements are the dominant ones.

For a cartesian rotation, when the new axes are rotated  $\phi$  degrees clockwise,



the transformed field components are

$$E' = \beta E \quad H' = \beta H \quad 2.5-2$$

where

$$\beta = \begin{bmatrix} \cos \phi & \sin \phi \\ -\sin \phi & \cos \phi \end{bmatrix} \quad 2.5-3$$

To transform the Z tensor, such that

$$E' = Z' H' \quad 2.5-4$$

then Z' must satisfy

$$Z' = \beta Z \beta^T \quad 2.5-5$$

or

$$Z'_{11} = Z_{11} \cos^2 \phi + (Z_{12} + Z_{21}) \sin \phi \cos \phi + Z_{22} \sin^2 \phi \quad 2.5-6a$$

$$Z'_{12} = Z_{12} \cos^2 \phi + (Z_{22} - Z_{11}) \sin \phi \cos \phi - Z_{21} \sin^2 \phi \quad 2.5-6b$$

$$Z'_{21} = Z_{21} \cos^2 \phi + (Z_{22} - Z_{11}) \sin \phi \cos \phi - Z_{12} \sin^2 \phi \quad 2.5-6c$$

$$Z'_{22} = Z_{22} \cos^2 \phi - (Z_{12} + Z_{21}) \sin \phi \cos \phi + Z_{11} \sin^2 \phi \quad 2.5-6d$$

For an isotropic or a layered earth,

$$Z_{11} = Z_{22} = 0, \quad Z_{12} = -Z_{21} \quad 2.5-7$$

Then upon any rotation

$$\begin{aligned} Z'_{12} &= Z_{12}, \quad Z'_{21} = Z_{21} \\ Z'_{11} &= Z'_{22} = 0 \end{aligned} \quad 2.5-8$$

This indicates the known result that for the isotropic earth case there are no  $E_x H_x$  or  $E_y H_y$  terms and the impedance is independent of the orientation of the measuring axes.

For a two-dimensional earth with the measuring axes aligned with the structure, the impedance tensor is characterized by

$$\begin{aligned} Z_{11} &= Z_{22} = 0 \\ Z_{12} &\neq Z_{21} \end{aligned} \quad 2.5-9$$

The structural strike and the perpendicular direction are defined as the principal axes of the conductivity structure. Upon rotation away from the principal direction, equations 2.5-6 indicate that diagonal elements appear, but such that

$$Z'_{11} = -Z'_{22} \quad 2.5-10$$



Two other important properties result:

- 1) For  $|Z_{12}| > |Z_{21}|$ ,  $|Z_{12}|$  is greater than any  $|Z'_{ij}|$  since it is equivalent to the major axis of the rotational ellipse for  $Z'_{ij}$ .
- 2) The magnitude of one off-diagonal element is always greater than the magnitude of the diagonal elements. Thus, a "Cagniard element" is always greatest.

Note that for an impedance tensor defined as

$$\begin{bmatrix} E_x \\ E_y \end{bmatrix} \equiv Z'' \begin{bmatrix} H_y \\ H_x \end{bmatrix}$$

equation 2.5-10 indicates that  $Z''$  is anti-symmetric.

#### Characteristics of measured impedance tensors

A common method for calculating the tensor elements involves calculating the Fourier components of E and H for two independent observations, then solving 2.5-1 for both observations simultaneously for the four elements. Madden and Nelson (1964) used the following statistical technique operating on the entire data series to yield the tensor elements. The horizontal Fourier components are related by

$$E_i = Z_{ij} H_j \quad 2.5-11$$

The tensor elements can be calculated from 2.5-11 via

$$\langle E_i \bar{H}_k \rangle = Z_{ij} \langle H_j \bar{H}_k \rangle \quad 2.5-12$$

where the cross power is expressed as  $\langle E_i \bar{H}_k \rangle$ . Therefore,

$$Z_{ij} = \langle E_i \bar{H}_k \rangle \langle H_j \bar{H}_k \rangle^{-1} \quad 2.5-13$$

When analyzing computed impedance tensors from actual field data, a simple rotation of the impedance tensor does not always yield a direction where  $Z'_{11} = Z'_{22} = 0$ , indicating that the principal axes are not cartesianally orthogonal. A similar complication with the admittance tensor has been discussed by Bostick and Smith (1962).

Because we desire to apply two-dimensional interpretation if it is possible, a method for obtaining the gross structural strike, if it exists, is required. This method should yield a meaningful direction in the presence of slight perturbations from the ideal two-dimensional impedance tensor form. The usual mathematical methods for

obtaining principal axes of an arbitrary complex matrix yield complex skew eigenvectors. The two following physical criteria yield conceptually simpler directions:

(1) the direction where an off diagonal element is maximum; and (2) the directions where a linearly polarized H produces an E in only the orthogonal direction. These criteria, which are discussed in Appendix 4, are incorporated into the data analysis described later in this thesis.

To determine whether two-dimensional interpretation is even possible, a "two-dimensionality" measure can be constructed from the elements of the impedance tensor. From equations 2.5-6, the following expressions are invariant to rotational transformations:

$$\begin{aligned} Z'_{11} + Z'_{22} &= Z_{11} + Z_{22} \\ Z'_{12} - Z'_{21} &= Z_{12} - Z_{21} \end{aligned}$$

From 2.5-10, the sum  $Z'_{11} + Z'_{22}$  should vanish for an ideal two-dimensional impedance tensor. By normalizing this sum by  $Z'_{12} - Z'_{21}$ , the invariant ratio

$$\frac{Z'_{11} + Z'_{22}}{Z'_{12} - Z'_{21}}$$

essentially measures the skewness of  $Z \cdot \begin{bmatrix} 0 & -1 \\ 1 & 0 \end{bmatrix}$  and is a useful "two-dimensionality coefficient".

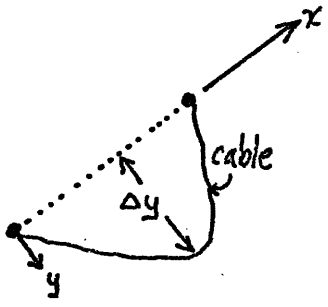
Improper impedance tensors from finite-length dipoles

Severe departures from two-dimensionality cannot be analyzed quantitatively because solutions of the three-dimensional forward problem are presently unavailable. A more fundamental problem lies in measuring the electric field with a dipole of finite length. For a one-dimensional conductivity structure with  $k_x = 0$ , the surface electrical field has a potential and the measured voltage is independent of the connecting cable. For a two-dimensional conductivity structure, not only is the surface field non-uniform, but the equipotential concept is not valid and the voltage measured between two electrodes depends upon the location of the connecting cable. This latter complication is due to the fact that  $E$  is not curl-free and the associated vertical magnetic field contributes a voltage from Faraday's Law

$$\mathcal{E} = \mu \iint \frac{\partial H_z}{\partial t} dx dy$$

2.5-15

To calculate the possible contribution from this integral, consider the following configuration:



The electric field contribution is

$$E_{(H_z)} = \frac{|\Sigma|}{x} = \mu\omega H_z \frac{\Delta y}{2} \tag{2.5-16}$$

For an area with  $H_z / (H_x^2 + H_y^2)^{1/2} = "R"$   
 and with  $\Delta y$  being " $X$ " times a skin depth,  $\delta = \sqrt{\frac{2}{\mu\omega\sigma_a}}$

$$\begin{aligned} E_{(H_z)} &\cong \frac{\mu\omega}{2} R (H_x^2 + H_y^2)^{1/2} X \sqrt{\frac{2}{\mu\omega\sigma_a}} \\ &\cong \frac{1}{\sqrt{2}} R X \left( \sqrt{\frac{\mu\omega}{\sigma_a}} H_{horizontal} \right) \\ &\cong \frac{1}{\sqrt{2}} R X (E_{horizontal}) \end{aligned} \tag{2.5-17}$$

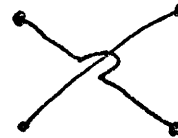
Therefore, the contribution from equation 2.5-17 as a per cent of the horizontal electric field ( $\int_{straight} E_{ds}$ ) is  $RX/\sqrt{2}$   
 For example, over an area where the H vertical/H horizontal ratio is 0.2, the cable should be less than two thirds of a skin depth away from the straight line between the electrodes to keep this contribution less than 10%.

Even with straight dipoles, the measured potential differences represent integrated electric fields corresponding to an average of the impedance tensor along the dipole.

Thus, in using 50 km electrode spacing at right angles, one dipole can span an area characterized by one Z while the other dipole spans another area 30 to 40 kms away characterized by a different Z. To obtain less distorted results, crossed dipoles should be employed:



standard



crossed

With the available electrode connections restricted to existing telephone lines, crossed dipoles could not be used in this thesis.

The measured tensor relationship is

$$\begin{bmatrix} E_A \\ E_B \end{bmatrix} = \begin{bmatrix} -(A_{12} + A_{21}) \sin \phi \cos \phi & A_{12} \cos^2 \phi - A_{21} \sin^2 \phi \\ B_{21} \cos^2 \phi - B_{12} \sin^2 \phi & (B_{12} + B_{21}) \sin \phi \cos \phi \end{bmatrix} \begin{bmatrix} H_A \\ H_B \end{bmatrix} \quad 2.5-18$$

where  $A_{ij}$  and  $B_{ij}$  are the elements of the tensor referenced to the strike direction appropriate for dipoles A and B

$\phi$  is the angle from A to principal structure axis

Upon rotation of the tensor into the structural axes, the tensor is

$$Z = \begin{bmatrix} (B_{21} - A_{21}) \sin \phi \cos \phi & A_{12} \cos^2 \phi + B_{12} \sin^2 \phi \\ B_{21} \cos^2 \phi + A_{21} \sin^2 \phi & (B_{12} - A_{12}) \sin \phi \cos \phi \end{bmatrix} \quad 2.5-19$$

This same tensor would result if the measured E field had been rotated first into the strike direction. Note that the diagonal elements do not vanish unless  $A_{ij} = B_{ij}$ .

Expression 2.5-19 was evaluated for theoretical values of  $A_{ij}$  and  $B_{ij}$  (obtained by the methods of section 2.4) for various locations over a vertical contact with a 100:1 conductivity contrast. Although two-dimensionally-improper tensors ( $Z_{11} \neq Z_{22}$ ) were obtained for almost every measuring orientation, only when the dipoles were spanning opposite sides of the contact were the skewness coefficients large and the calculated apparent resistivities and principal direction incorrect. Figure 2.7 includes some numerical results.

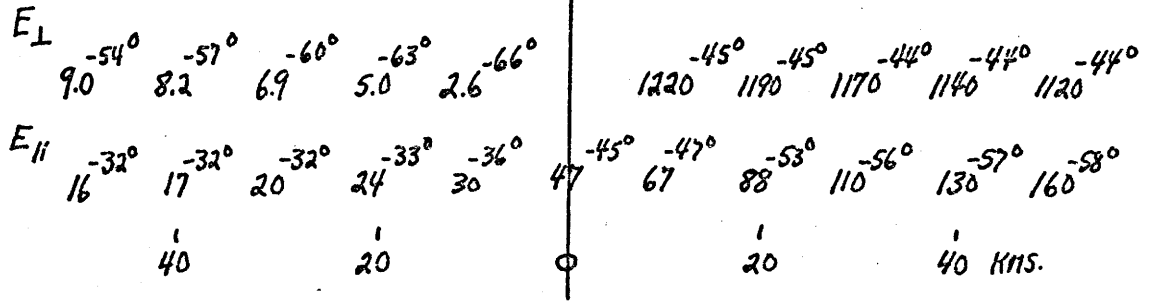
These theoretical improper tensors afford an empirical check on the skewness coefficient of equation 2.5-14. For values of the skewness coefficient less than 0.3 the calculated principal directions are good to within 10 degrees; for values greater than 0.6 the calculated principal directions are meaningless.

Example: vertical contact  $f = 10^{-3}$  cps

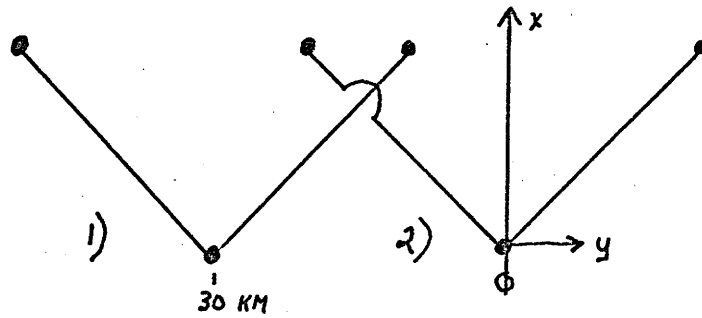
$$\rho_1 = 10$$

$$\rho_2 = 1000 \Omega\text{-M}$$

Theoretical apparent resistivities for small dipoles:



For 30 km dipoles oriented at  $45^{\circ}$  to strike:



Observed apparent resistivities:

1)	$20^{-33^{\circ}}$	2)	$520^{-46^{\circ}}$	← $\rho_1$	} TENSOR APPARENT RESISTIVITIES ALONG PRINCIPAL AXES
	$7^{-59^{\circ}}$		$3.4^{-37^{\circ}}$		
	E-W		$N66^{\circ}E$	←	Principal axis
	0.05		0.66	←	Skewness coeff.

Figure 2.7 Effect of finite-length dipoles on the measured apparent resistivities over a vertical contact



## Chapter 3 - Magnetotelluric Experiment in the Southwestern United States

During the summers of 1965 and 1966, a magnetotelluric survey occupied stations mostly along a profile from Yuma, Arizona, to Roswell, New Mexico. The recording sites are shown on a location map (Figure 3.1).

This chapter discusses the acquisition, analysis and interpretation of magnetotelluric data from these seven stations. This treatment incorporates many features not included in the initial approach by Cagniard (1953), namely, the use of magnetic data from one observatory for a number of distant telluric measurements, the use of forty mile telephone lines for electrode connections, the use of a tensor approach for calculating apparent resistivities, and the use of two-dimensional interpretation.

### 3.1 Magnetic field data

To sample upper mantle conductivity, electromagnetic variations with periods greater than one hour are required. The Tucson Coast and Geodetic Survey Geomagnetic Observatory routinely records normal magnetograms which include this period range. Since the entire region of interest in the Southwest lies within 400 miles of Tucson, the uniformity of

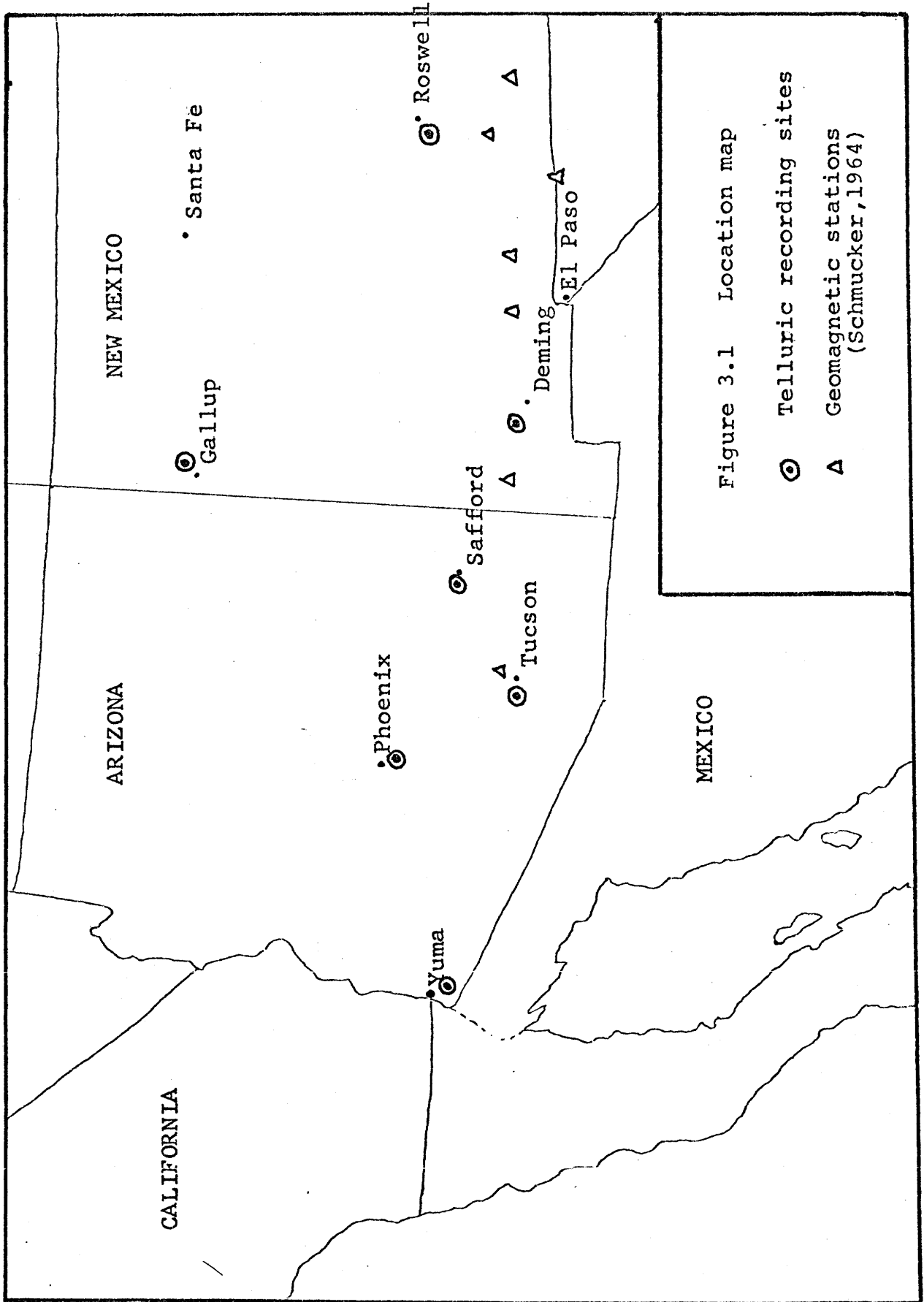
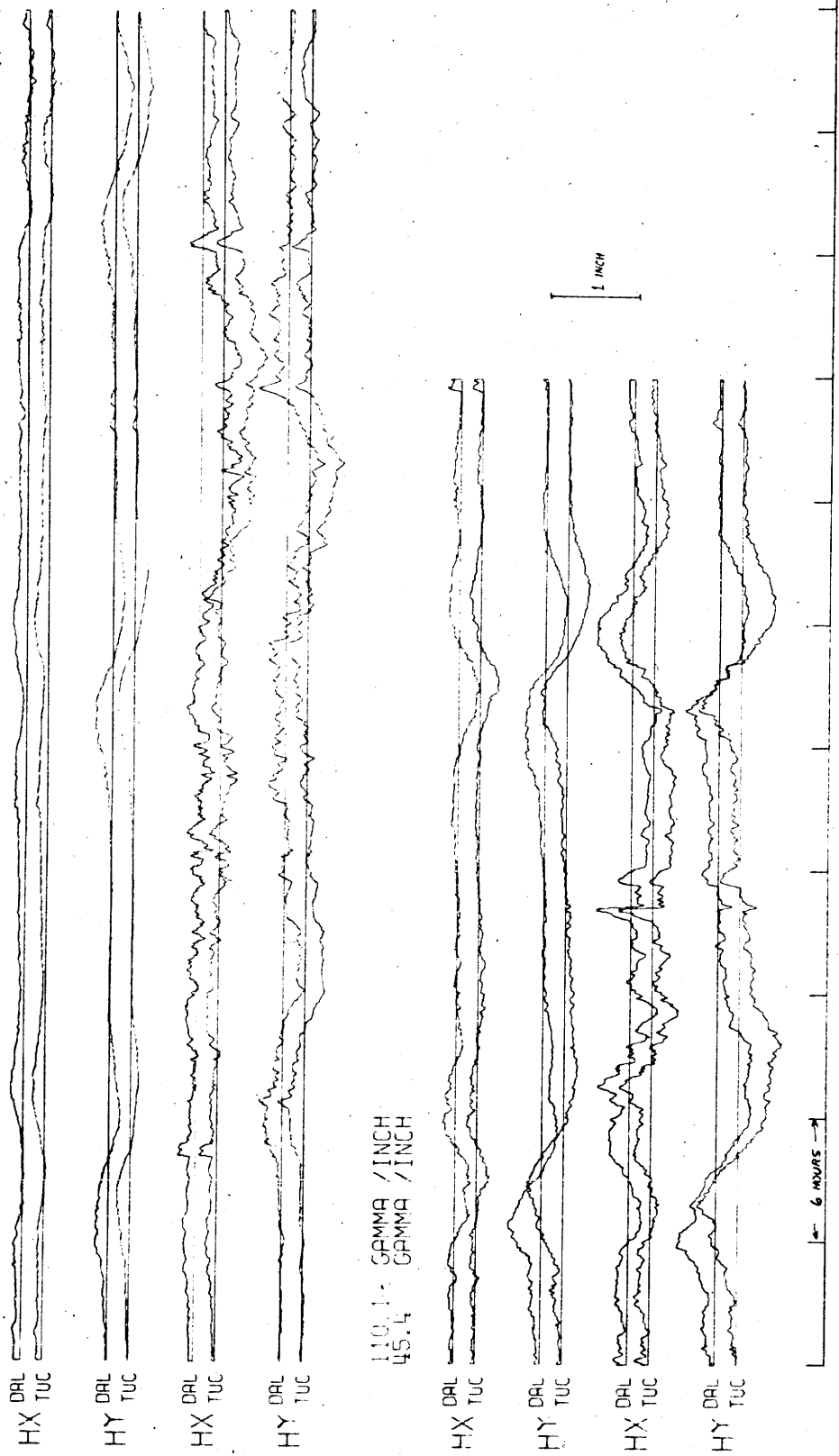


Figure 3.1 Location map  
⊙ Telluric recording sites  
△ Geomagnetic stations (Schmucker, 1964)

the magnetic field suggests that the magnetic field observed at Tucson could be used as being representative of the entire region. This strong assumption requires the horizontal wavelengths to be very long. Thus, a correlation study of geomagnetic observatory data from a few stations provides observational evidence of the horizontal wavelength structure to justify both the use of only Tucson magnetic data and the assumption of a plane-wave incident field in later interpretation.

In Figure 3.2, the magnetic observatory data from Tucson and Dallas, stations 800 miles apart, are plotted together for comparison for two time periods of six and four days. Observatory data from Boulder, Colorado, appear to be similarly correlated with the Tucson and Dallas data. The correspondence between the data shown in Figure 3.2 is striking; the diurnal variation shows a phase shift appropriate to the lateral separation of the stations, the higher frequency variations appear to be simultaneous.

The results of a quantitative correlation study of the magnetic field components at Tucson and Dallas are shown in Figure 3.3. Coherency, phase shift, and power ratio (Dallas/Tucson) are plotted as a function of frequency for the two horizontal components. The shortest horizontal



GEOMAGNETIC OBSERVATORY DATA  
 DALLAS, TEXAS  
 TUCSON, ARIZONA  
 JUNE 9-9, 1965  
 JUNE 12-17 (NOON), 1965

Figure 3.2 Geomagnetic Observatory Data  
 Dallas, Texas, and Tucson, Arizona

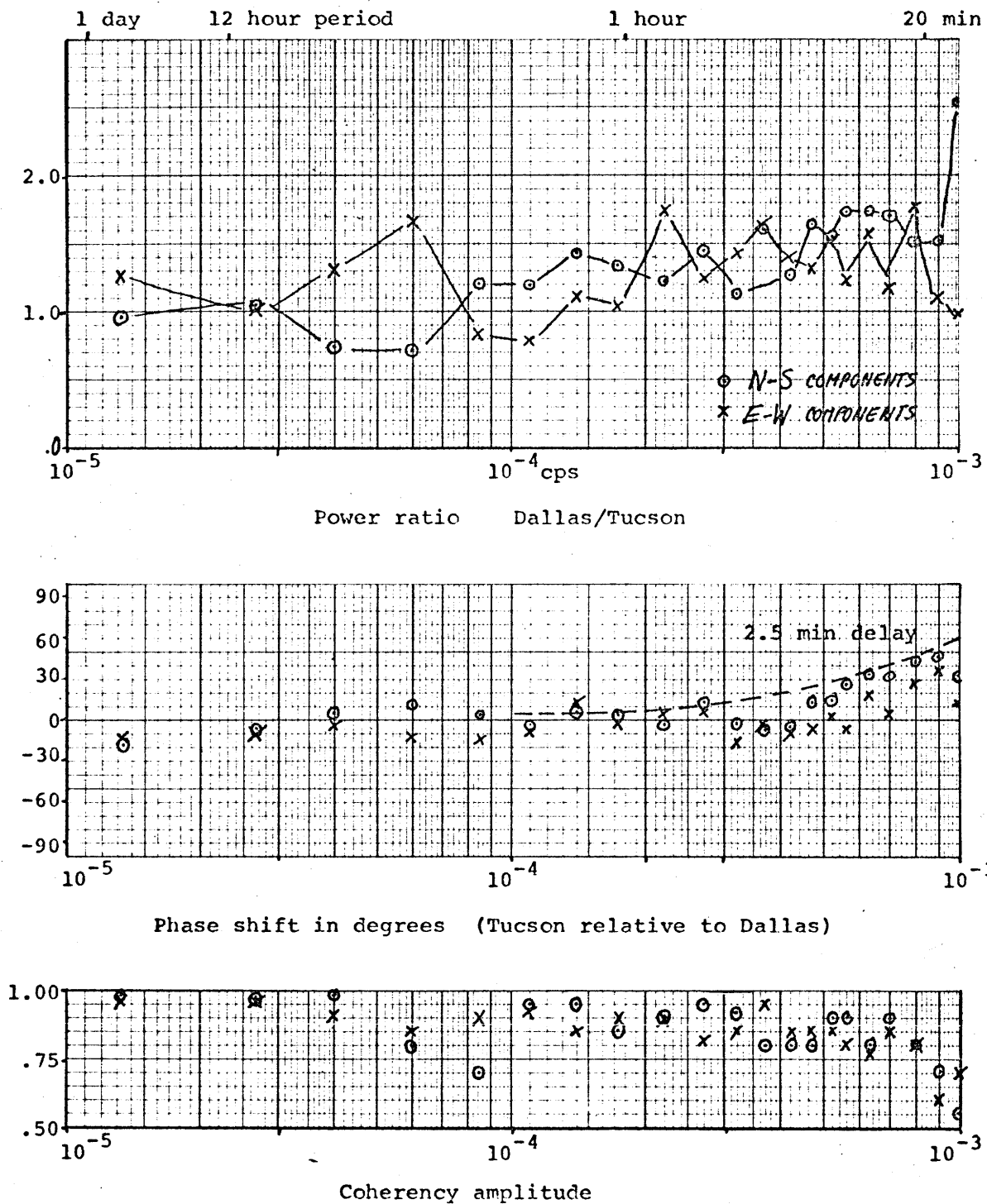


Figure 3.3 Coherency analysis of magnetic fluctuations, Dallas and Tucson data, June 12-17, 1965

wavelengths suggested from these results are about 10,000 km for the high frequency end. The diurnal phase shift represents a true delay with a horizontal wavelength of the earth's circumference. The higher frequency phase shift could be explained by a 2.5 minute delay due to an accounting error, since the digitizing sampling rate was 2.5 minutes. The power ratios vary over a factor of two, but a single total horizontal component ratio would be significantly flatter.

The flat power ratio and low phase shift, together with the high coherency, validates the long wavelength assumption. It should be emphasized that this amplitude correlation between magnetic fields from two separated observatories does not apply to the vertical component, which is far more sensitive to the subsurface conductivity structure.

The major benefit of using the Tucson magnetic data is that only the telluric measurement had to be made. The magnetic data was recorded on well-calibrated variometers and was digitized by NASA. Thus, digitized magnetic data, sampled every 2.5 minutes, consisting of H (magnetic intensity) in gammas and D (magnetic declination) in tenths-minutes, was available for use in the magnetotelluric investigation.

### Sources of the incident magnetic field

The magnetic field data plotted in Figure 3.2 clearly represent two source mechanisms, the diurnal variation and magnetic storm activity. Detailed discussions of these mechanisms are found in Chapman (1964) and Paghis (1965), for example.

The magnetic diurnal variation is caused by the dynamo current system in the E-layer of the ionosphere which is set up by solar heating of the day-side ionosphere. For Tucson at the summer solstice, the horizontal component of the diurnal variation is roughly elliptically polarized with a major WNW component and rotates in a clockwise sense.

Magnetic storm activity is directly correlated with the bulk velocity of the solar wind (Snyder, 1963), and is ultimately due to enhanced particle emissions from the sun. The enhanced solar wind perturbs the entire magnetosphere so that disturbances, which propagate down through the ionosphere as hydromagnetic waves, occur nearly simultaneously over the globe. The major characteristics of a magnetic storm are well shown in the June 12-17, 1965, data of Figure 3.2. The sudden commencement, the sudden increase in the field, is due to a sudden increase in the solar wind pressure which causes a compression of the magnetosphere

and the field lines. The later main phase, the extended decrease in the field, is due to either the ring current drift of energetic particles in the magnetosphere or transport of field lines into the tail. Other sources of low-frequency fluctuations are ionospheric currents induced by electric fields associated with disturbed magnetospheric plasma. Isolated "bay" variations are caused by solar-flare induced, temporary enhancement of polar D-layer ionization.

Although these mechanisms produce long horizontal wavelengths at low latitudes, the polar and equatorial electrojets plus increased over-all activity in the auroral regions are more local sources with shorter horizontal wavelengths. Magnetotelluric investigations in these regions must consider the finite source length (Spitznogle, 1966).



### 3.2 Electric field measurement

For the low frequency range investigated in this thesis, the skin depths are large (50-500 km) and the associated electric fields at the surface are weak. Large electrode separations in the measurement of the electric field are required to average out the irregularities in the surface conductivity structure in order to unmask the effects of the deeper features of interest. Telephone lines, which have been used occasionally (Rooney, 1935), provide such large separations. The stations shown in Figure 3.1 are those locations between southeastern California and the Texas panhandle where it was possible to obtain two long telephone lines at approximately right angles. For many of these electrode configurations, local crustal structures, particularly sedimentary grabens, are the same scale as the dipole length. Therefore, the electrode separations are not long enough to average out the surface conductivity variations. As discussed in section 2.4, this situation may result in a distorted measured field. Data from additional stations at El Paso, Texas, and Santa Fe, New Mexico, were corrupted by commercial noise.

At each station, all-metal land lines without intermediate-stage amplification and filtering carried the

signal from the electrodes into the central telephone office where the recording equipment was kept. Lead plates, 6" by 8" in size, buried about three feet in moist sandy soil, provided electrode pairs with resistance usually less than 600 ohms. The telluric lines were from 16 to 85 kilometers in length. Typical measured voltage fluctuations of 0.1 volt are well above the low lead-electrode noise levels.

The recording instrumentation consisted of a variable gain amplifier incorporating a two-pole low pass Chebyshev filter ( $\xi = 0.25$ ) and three Rustrak recording voltmeters for each channel. Amplifier response is given in Figure 3.4. To allow unattended recording, two recording voltmeters, at 3"/hour chart speed, were of different sensitivities (1 and 5 volt full scale) to record large variations in rms amplitude. The third recording voltmeter (5 volt full scale) ran at 1"/hour chart speed to provide a monitor recording for comparison with the magnetograms. Table 3.1 lists the recording details - recording dates, electrode sites, dipole lengths, and gain settings.

The data were hand digitized at a 2.5 minute sampling interval to correspond to the sampling interval of the magnetic data. Orthogonal north and east components of the telluric field were calculated from the non-orthogonal

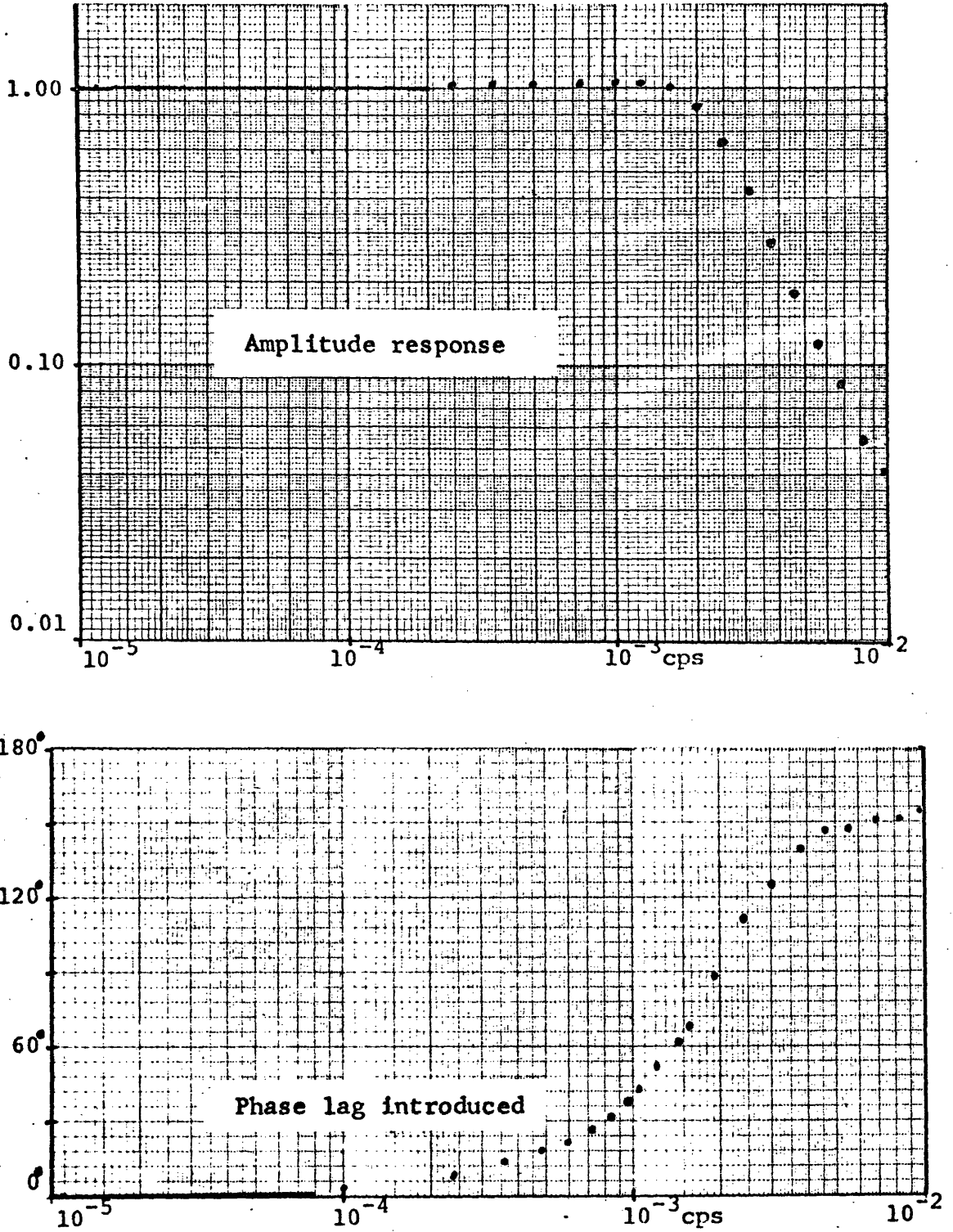


Figure 3.4 Gain response of telluric instrumentation

Station	Recording Dates	Electrode Sites	Gain
Roswell, N.M.	6/11(7 PM)-6/17(5 PM), 1965	Ground at Roswell telephone office Hondo, N.M., 71.6 km to N88°W Artesia, N.M., 63.8 km to S11°E	7.9X 10.5X
Deming, N.M.	6/7(5 PM)-6/14(4 PM), 1966	Ground in Wilna, N.M. Silver City, N.M., 62.8 km to N1°E Deming, N.M., 49.9 km to N85°E	20.0X 20.0X
Safford, Ariz.	6/26(noon)-7/5(9 PM), 1965	Ground at base of Swift Trail Rd. Pima, Ariz., 20.8 km to N34°W Morenci, Ariz., 24.1 km to N66°E	25.4X 27.0X
Tucson, Ariz.	6/15(noon)-6/27(noon), 1966	Ground at Fort Lowell Ruins, Tucson Red Rock, Ariz., 48.3 km to N52°W Sahuarita, Ariz., 35.4 km to S10°W	20.0X 50.0X
Phoenix, Ariz.	7/6(9 PM)-7/23(2 PM), 1965	Ground at Surprise, Ariz. Litchfield, Ariz., 16.1 km to S16°N Apache Jct., Ariz., 73.4 km to S75°E	18.3X 7.3X
Yuma, Ariz.	6/28(1 PM)-7/21(noon), 1966	Ground at Maricopa, Ariz. Sun City, Ariz., 69.2 km to N23°W Apache Jct., Ariz., 61.2 km to N46°E	20.0X 20.0X
	6/5(6 PM)-6/10(9 AM), 1965	Ground at Yuma telephone office Somerton, Ariz., 20.7 km to S38°W Ligurta, Ariz., 29.9 km to S79°E	11.5X 15.5X
Gallup, N.M.	7/22(9 AM)-8/1(9 AM), 1966	Ground at Gallup telephone office Newcomb, N.M., 85.3 km to N3°E Thoreau, N.M., 51.6 km to S77°W	20.0X 20.0X

Table 3.1 Telluric Recording Data

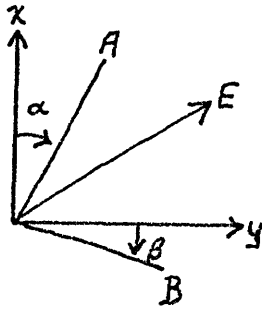
measurements by

$$E_x = (A \cos \beta - B \sin \alpha) / \cos(\alpha - \beta)$$

$$E_y = (A \sin \beta + B \cos \alpha) / \cos(\alpha - \beta)$$

3.2.1

where



### 3.3 Method of data analysis

Spectral and coherency analysis were used to reduce the magnetotelluric data of this thesis through computer programs written by T. R. Madden and the author. Spectral analysis of low-frequency electromagnetic data has been discussed by Madden (1964).

Two separate analyses were applied to the data, in which the frequency content ranges from the diurnal ( $10^{-5}$  cps) to the Nyquist ( $.33 \times 10^{-2}$  cps). For the higher frequencies, a digital-sonogram analysis results in power spectra, coherencies, impedance tensor elements, and apparent resistivities as a function of time. Hopkins and Smith (1966) have also presented running power spectra as a part of magnetotelluric investigation. For the lower frequency decade, the typical six-day data series is not sufficient for a meaningful running spectral analysis. Moreover, for the low frequency energy, which is dominated by the harmonics of the regular diurnal variation, the lack of random signals produces a high  $H_x H_y$  coherency which causes the tensor elements computed from equations 3.3-3 to be unstable. Therefore, the data were rotated into the principal directions, as determined by the higher frequency analysis, before spectral computations.

To calculate power spectral estimates of magnetotelluric data Cantwell (1960) and Ellis (1964) assumed stationary data series and calculated power spectra by Fourier transforming the auto- and cross-correlation functions. An alternate approach to the calculation of power spectra, which is particularly efficient if many inter-related cross-spectra are desired, is through the Fourier spectra of the individual data series:

Fourier spectra:  $E_x(\omega)$ ,  $E_y(\omega)$ ,  $H_x(\omega)$ ,  $H_y(\omega)$

Power spectra:  $\langle E_x \bar{E}_x \rangle$ , etc.

Cross spectra:  $\langle E_x \bar{H}_y \rangle$ , etc.

where  $\bar{E}_x(\omega)$ , etc. = conjugate Fourier spectra and the brackets represent averaging in time for finite band-widths. This scheme substitutes computationally quick multiplications for time-consuming correlations and was used in both approaches.

#### Higher frequency analysis

For frequency components between  $1.1 \times 10^{-4}$  cps (2 1/2 hours) and  $1.7 \times 10^{-3}$  cps (10 minutes), the four data series were high-pass filtered, then fed continuously into a bank of twenty constant-Q digital recursive filters spanning the frequency band. Constant-Q filters, which measure power

density as power per octave, effectively "flatten" geomagnetic power spectra with rough 1/f characteristics. The filter outputs were corrected for recording instrument response (for  $E_x$  and  $E_y$ ), plotted as single frequency polarization ellipses for the electric and magnetic fields, and then used to obtain the following auto-power and cross-power spectra as a function of time within the data set.

$$\text{Auto spectra: } \langle E_x \bar{E}_x \rangle, \langle E_y \bar{E}_y \rangle, \langle H_x \bar{H}_x \rangle, \langle H_y \bar{H}_y \rangle$$

$$\text{Cross spectra: } \langle E_x \bar{E}_y \rangle, \langle E_x \bar{H}_x \rangle, \langle E_x \bar{H}_y \rangle \\ \langle E_y \bar{H}_x \rangle, \langle E_y \bar{H}_y \rangle, \langle H_x \bar{H}_y \rangle$$

Computational details, including a more specific description of the filters, can be found in Appendix 5.

These spectra were used to calculate coherencies, which are required to calculate the impedance tensor elements where:

$$\text{coherency (AB)} = \frac{\langle A\bar{B} \rangle}{(\langle A\bar{A} \rangle \langle B\bar{B} \rangle)^{1/2}} \quad 3.3-1$$

The coherency is a quantitative measure of the amount of linear relationship between two data series. Thus, the coherency measures the consistency of the phase difference between the two data series.



Now the impedance elements can be calculated from equation 2.4-4

$$Z_{ij}(\omega) = (\langle E_i \bar{H}_k \rangle) (\langle H_j \bar{H}_k \rangle)^{-1} \quad 3.3-2$$

Expansion yields

$$Z_{11} = \frac{|E_x|}{|H_x|} \left( \frac{\text{coh } E_x H_x - \text{coh } E_x H_y \text{ coh } H_y H_x}{1 - |\text{coh } H_x H_y|^2} \right) \quad 3.3-3a$$

$$Z_{12} = \frac{|E_x|}{|H_y|} \left( \frac{\text{coh } E_x H_y - \text{coh } E_x H_x \text{ coh } H_x H_y}{1 - |\text{coh } H_x H_y|^2} \right) \quad 3.3-3b$$

$$Z_{21} = \frac{|E_y|}{|H_x|} \left( \frac{\text{coh } E_y H_x - \text{coh } E_y H_y \text{ coh } H_y H_x}{1 - |\text{coh } H_x H_y|^2} \right) \quad 3.3-3c$$

$$Z_{22} = \frac{|E_y|}{|H_y|} \left( \frac{\text{coh } E_y H_y - \text{coh } E_y H_x \text{ coh } H_x H_y}{1 - |\text{coh } H_x H_y|^2} \right) \quad 3.3-3d$$

where  $|E_x| = \langle E_x \bar{E}_x \rangle^{1/2}$  etc., the Fourier amplitude spectra. From these impedance elements, principal axes and principal values were calculated using the methods outlined in Appendix 4.

Standard Cagniard resistivities are simply calculated from the power spectra as

$$P_{a_{xy}}(f) \equiv \frac{0.2}{f} \frac{\langle E_x \bar{E}_x \rangle}{\langle H_y \bar{H}_y \rangle} \quad 3.3-4$$

$$P_{a_{yx}}(f) \equiv \frac{0.2}{f} \frac{\langle E_y \bar{E}_y \rangle}{\langle H_x \bar{H}_x \rangle} \quad 3.3-5$$

where the frequency,  $f$ , is in cps, the electric power is in  $(\text{mv}/\text{km})^2$ , and the magnetic power is in  $(\gamma)^2$ . As discussed in Chapter 2, however, meaningful apparent resistivities for two-dimensional structures must be calculated from the principal values of the impedance tensor.

$$P_{a_k}(f) = \frac{0.2}{f} |Z_k|^2 \quad k=1,2 \quad 3.3-6$$

where  $Z_k$  = principal values of  $Z_{ij}$

The digital sonogram analysis yields power spectra, coherencies, and apparent resistivities as a function of time, and, thus, exhibits the time variations of the characteristics of the source field and the calculated apparent resistivities. The coherency between orthogonal E and H components, which can be used as a "reliability criterion" for the calculated apparent resistivities over layered-media geometries, can be deceptively low over

two-dimensional conductivity structures and, thus, must be replaced by a criterion which involves all four horizontal components. A useful measure of predictability is the coherency between  $E$  and  $E^{\text{predicted}}$  for the two components,  $E_x$  and  $E_y$ .

$$\text{coh} (E_i^{\text{Predicted}} E_i) \equiv \frac{\langle E_i^{\text{Pred}} \bar{E}_i \rangle}{(\langle E_i^{\text{P}} \bar{E}_i^{\text{P}} \rangle \langle E_i \bar{E}_i \rangle)^{1/2}} \quad 3.3-7$$

where  $E_i^{\text{Pred}} = Z_{i1} H_x + Z_{i2} H_y$  3.3-8a

and  $\langle E_i^{\text{Pred}} \bar{E}_i \rangle = Z_{i1} \langle H_x \bar{E}_i \rangle + Z_{i2} \langle H_y \bar{E}_i \rangle$  3.3-8b

Upon expansion this expression becomes

$$\text{coh}(E_i^{\text{P}} E_i) = \frac{|H_x| Z_{i1} \text{coh}(H_x E_i) + |H_y| Z_{i2} \text{coh}(H_y E_i)}{[|Z_{i1}|^2 |H_x|^2 + |Z_{i2}|^2 |H_y|^2 + 2 |H_x| |H_y| \text{Re}(Z_{i1} Z_{i2} \text{coh} H_x H_y)]^{1/2}} \quad 3.3-9$$

These coherencies were also calculated as running parameters.

### Lower frequency analysis

To calculate results for frequency components between  $10^{-5}$  cps (1 day) and  $1.3 \times 10^{-4}$  cps (2 hours), the data were first rotated into the principal directions for the measuring site as determined by the tensor analysis of the

higher frequency analysis. Fourier transforms of the four complete data series were calculated, then the same four auto-power and six cross-power spectra as in the higher frequency analysis.

Cagniard apparent resistivities, coherencies, tensor elements,  $E - E^{\text{predicted}}$  coherencies, and principal value tensor apparent resistivities were calculated using the expressions presented above. When a high  $H_x H_y$  coherency causes the tensor elements to be unstable, as is the usual situation, the Cagniard apparent resistivities are more reliable since the reference axes have been alligned approximately with the principal axes.

#### Sources of error

Errors in the data analysis are more likely due to bias and high sensitivity to noise than statistical errors in the computational estimates. The problem of estimating the statistics of a stationary process are not applicable since low-frequency magnetotelluric signals have transient characteristics. The running spectra emphasize the non-stationarity of the data. Other digital analyses of magnetotelluric data over many decades of frequency have pre-whitened the data to reduce spectral spill-over (Ellis,

1964; Hopkins and Smith, 1966). Pre-whitening, other than the use of power/octave in the sonogram analysis, did not improve the results in this investigation.

High sensitivity to noise in the digital data can result from poor digitizing resolution at times of low signal level, from calculating relatively small tensor elements for severe anisotropy, or from calculating the impedance elements when the  $H_x H_y$  coherency is high. Actually, the form of the expression for  $Z_{ij}$  (Equation 3.3-3) is a strong argument for using the impedance rather than the admittance, because the denominator of the expression for  $Y_{ij}$  contains  $(1 - |\text{coh } E_x E_y|^2)$ . The preferred current direction caused by two-dimensional conductivity structure causes the  $E_x E_y$  coherency to be greater than the  $H_x H_y$  coherency and, hence, division by  $(1 - |\text{coh } E_x E_y|^2)$  can be very unstable.

Bias error on the electric channels could be introduced by an E field miscalibration, an inaccurate dipole length, a non-straight telephone line connection between electrodes, or an E field distortion. Except for stations with very high skewness coefficients, this combined error should be less than 20%.

Worse bias error can be introduced by the use of the

Tucson data as representative of the magnetic field at the telluric recording sites. The variations between magnetic data from Dallas and Tucson shown in Figure 3.3 are reflected in apparent resistivities calculated using Roswell telluric data and magnetic data first from Tucson, and then from Dallas. Apparent resistivities differ by factors up to 2.5 but averaging 0.2, while the associated E-H phases differ by amounts up to  $70^{\circ}$  but averaging  $15^{\circ}$  (Figures 3.9 and 3.11). Differences between the magnetic data are due to real changes of the field at two locations 1300 km apart at slightly different geomagnetic latitude, plus possible high frequency contamination from different instrument responses and digitizing and aliasing error. Since the separation between Dallas and Tucson is more than twice as great as the distance from Tucson to the telluric stations, the error in using the Tucson data as representative can be up to 60% in apparent resistivity values and 35% in the phase estimate, but only at the higher frequencies. As mentioned in section 2.5, laterally inhomogeneous conductivity structure can affect the magnetic field perpendicular to the structure. However, this effect is less than 2% for the theoretical models involved.

Bias error can be introduced in the calculations by an incorrect rotation angle for the low frequency Cagniard estimates and by the effect of noise on the impedance elements. To examine how added noise can effect Z, and how well the E predictability coherency detects this error, consider:

a) incoherent noise introduced on  $E_i$  such that

$$E_i^{\text{Noisy}} = E_i + N$$

$$\langle E_i \bar{N} \rangle = 0$$

$$\langle H_j \bar{N} \rangle = 0$$

$$|E_i^{\text{Noisy}}| \equiv c_i |E_i|$$

3.3-10

Then the coherency is given as

$$\text{coh}(E_i^{\text{Noisy}} H_j) = \frac{\langle E_i \bar{H}_j \rangle + \langle N \bar{H}_j \rangle}{(\langle E_i^N \bar{E}_i^N \rangle \langle H_j \bar{H}_j \rangle)^{1/2}}$$

3.3-11

$$\therefore \text{coh}(E_i^N H_j) = \frac{1}{c_i} \text{coh}(E_i H_j)$$

For  $\text{coh}(H_x H_y)$  small, as was usually chosen, the impedance elements (from equations 3.3-3) are

$$Z_{ij} = \frac{|E_i|}{|H_j|} \text{coh}(E_i H_j)$$

3.3-12

From 3.3-10 and 3.3-11,  $Z^{\text{noisy}}$  is given as

$$Z_{ij}^{\text{Noisy}} = \frac{C_1 |E_i|}{|H_j|} \frac{\text{coh}(E_i H_j)}{C_1} = Z_{ij} \quad 3.3-13$$

Therefore, the impedance elements are unaffected by incoherent noise on the E channel.

For  $\text{coh}(H_x H_y) = 0$ , the E predictability coherency of equation 3.3-7 reduces to

$$\text{coh}(E_i^{\text{Pred}} E_i) = \sqrt{|\text{coh}(E_i H_1)|^2 + |\text{coh}(E_i H_2)|^2} \leq 1 \quad 3.3-14$$

For noise-free data,  $\text{coh}(E_i^{\text{pred}} E_i) = 1.0$ ; for noisy data, from equation 3.3-11,

$$\text{coh}(E_i^{\text{Pred}} E_i) = \frac{1}{C_1} = \frac{|\text{signal}|}{|\text{signal} + \text{noise}|} \quad 3.3-15$$

Thus, a  $E_i$  predictability coherency of 0.8 can be explained by 25% added noise power to  $E_i$ .

b) incoherent noise introduced on  $H_j$  such that

$$\begin{aligned} H_j^{\text{Noisy}} &= H_j + N \\ \langle E_i \bar{N} \rangle &= 0 \\ \langle H_j \bar{N} \rangle &= 0 \\ |H_j^{\text{Noisy}}| &\equiv C_2 |H_j| \end{aligned} \quad 3.3-16$$



The effect on the coherency is

$$\text{coh}(E_i H_j^{\text{Noisy}}) = \frac{1}{c_2} \text{coh}(E_i H_j) \quad 3.3-17$$

The effect on the E predicted coherency, as given by equation 3.3-14 is

$$\text{coh}(E_i^{\text{Pred}} E_i) = \sqrt{1 - (1 - \frac{1}{c_2^2} \text{coh}^2(E_i H_j))} \quad 3.3-18$$

or for similar percentages of incoherent noise added to both magnetic channels

$$\text{coh}(E_i^{\text{Pred}} E_i) = \frac{1}{c_2} = \frac{| \text{signal} |}{| \text{signal} + \text{noise} |} \quad 3.3-19$$

The good correlation between  $E_x$  predictability and  $E_y$  predictability (see Figure 3.7) suggests that any noise is being introduced equally into  $E_x$  predicted and  $E_y$  predicted. Because this pattern remained on using independent electric channels, noise on the magnetic channels is indicated.

The effect of noise in H on Z is, for small  $\text{coh}(H_x H_y)$ ,

$$Z_{ij}^{\text{Noisy}} = \frac{|E_i|}{c_2 |H_j|} \frac{\text{coh}(E_i H_j)}{c_2} = \frac{1}{c_2^2} Z_{ij} \quad 3.3-20$$

Therefore, the tensor elements are reduced for added noise on the magnetic channel. For an E predictability of 0.8, the indicated noise power is 25% of the magnetic power, and the impedance elements are reduced 36%.

For a significant coh ( $H_x H_y$ ) and/or a significant amount of coherent noise on the H channels, a change in the denominator of the expressions for Z (equations 3.3-3) can further affect the impedance elements. For an E predictability of 0.8, which allows a 25% added noise power, and restricting the computed coh  $H_x H_y$  to be less than 0.5, incoherent noise can introduce a decrease of 25% to  $Z_{ij}$ ; whereas the same amount of coherent noise can produce an increase of 25%. This additional factor to the previous 36% reduction results in the overall effect - for an E predictability of 0.8 the effect of noise on  $Z_{ij}$  can range from no effect to a 45% reduction in Z or a 70% reduction in the apparent resistivity. Moreover, unequal effects on the various  $Z_{ij}$  elements can result in a distorted tensor.

In actual practice, low scatter in the apparent resistivity values and in the principal axis direction accompanied a good predictability of E as measured by a high E - E predicted coherency. Although E predictabilities of greater than 0.95 were available for frequencies between

$1.1 \times 10^{-4}$  and  $6.1 \times 10^{-4}$  cps, lower E predictabilities at higher frequencies suggest that H field noise might cause the increased scatter and a general lowering of apparent resistivity estimates at the higher frequencies, as shown in the next section.

### 3.4 Magnetotelluric apparent resistivity results

In this section the results of the data analysis are presented station by station, first from east to west along the profile and then Gallup (see Figure 3.1). Discussion and interpretation follow in the next section. Electrode site information is included in Table 3.1. Note that  $x$  and  $y$  refer to north and east, respectively.

The Roswell, New Mexico, data will be fully discussed first to illustrate the analysis procedures.

#### Roswell, New Mexico

The four-component magnetotelluric field data for Roswell, rotated into N-S and E-W reference directions, are plotted in Figure 3.5. In this and other field data figures, the magnetic values are from the Tucson observatory. As example outputs of the digital-sonogram analysis on the higher frequencies, Figure 3.6 shows the power density spectra of these four components and the  $E_x H_y$ ,  $E_y H_x$ ,  $E_x E_y$ , and  $H_x H_y$  coherencies. Figure 3.7 shows the  $E_x - E_x$  predicted and the  $E_y - E_y$  predicted coherencies. Note that the analysis in both Figures 3.6 and 3.7 starts 36 hours into the data shown on Figure 3.5.

The across-the-board increase in power (at 45 hours

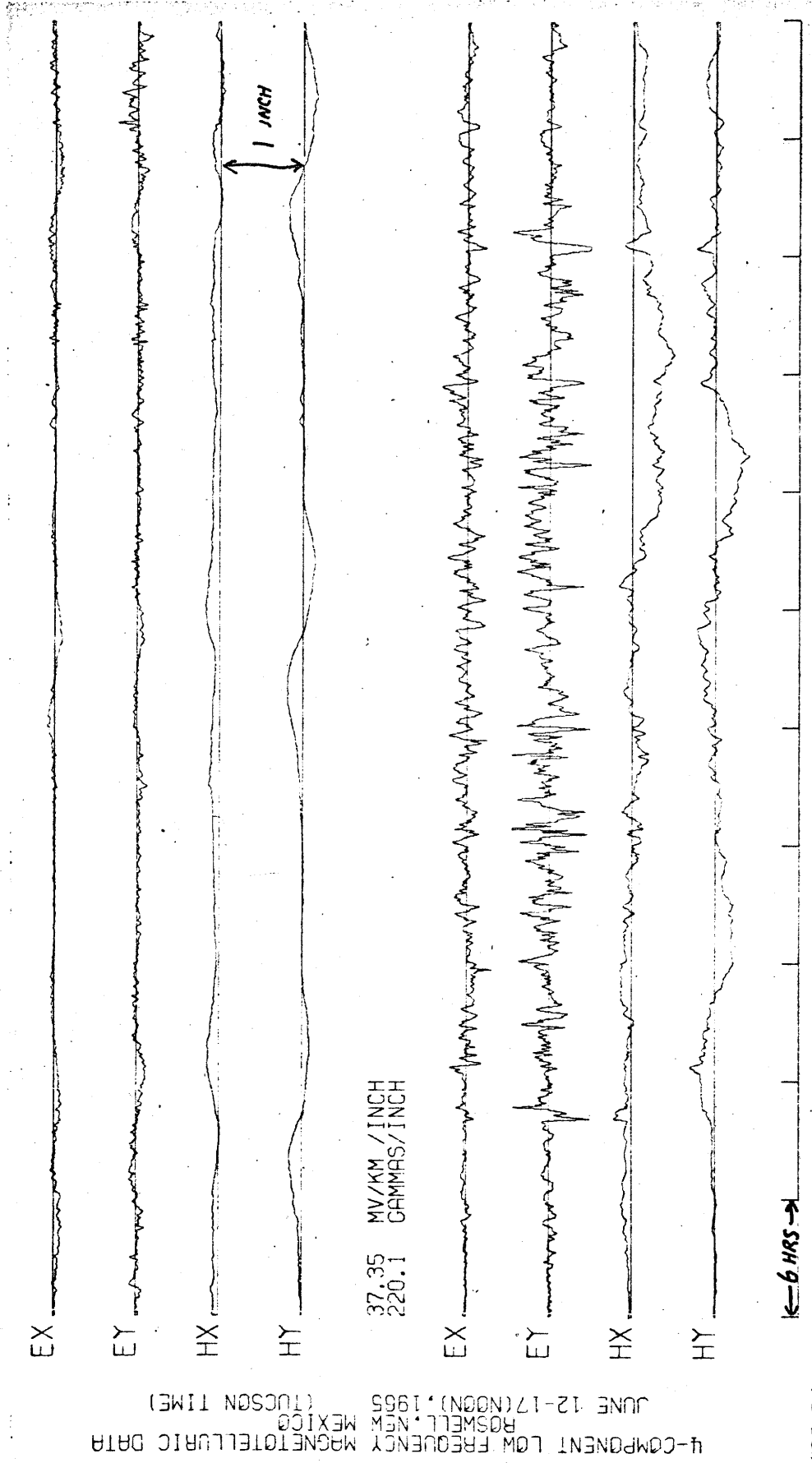


Figure 3.5 Magnetotelluric field data, Roswell, N.M.

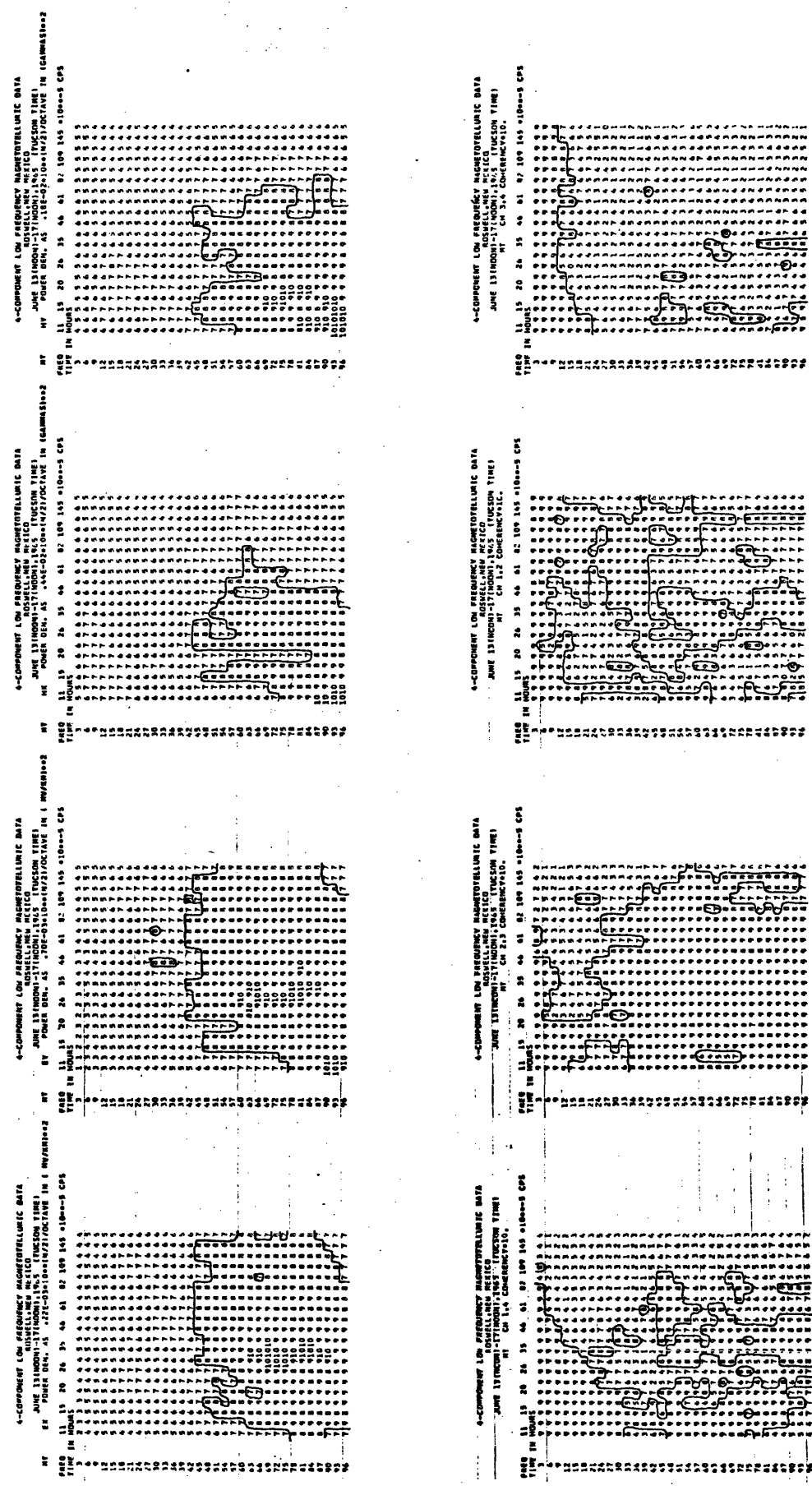


Figure 3.6 Power spectra and coherencies, Roswell, N.M.

4-COMPONENT LOW FREQUENCY MAGNETOTELLURIC DATA  
ROSWELL, NEW MEXICO  
JUNE 13 (NOON)-17 (NOON), 1965 (TUCSUN TIME)

COHERENCY BETWEEN EX AND EX PREDICTED FROM H VIA IMPEDANCE TENSOR

FREQ TIME	11	15	20	26	35	46	61	8	109	145	*10***-5	CPS
3	1010101010101010101010	910101010	9	9	9	9	9	9	9	9	9	9
6	1010101010101010101010	9	8	7	7	7	7	7	7	7	7	7
9	1010101010101010101010	9	9	9	9	9	9	9	9	9	9	9
12	1010101010101010101010	9	9	9	9	9	9	9	9	9	9	9
15	1010101010101010101010	9	9	9	9	9	9	9	9	9	9	9
18	91010101010101010101010	9	8	8	8	8	8	8	8	8	8	8
21	9	9	9	9	9	9	9	9	9	9	9	9
24	91010101010101010101010	9	9	9	9	9	9	9	9	9	9	9
27	101010101010101010101010	9	9	9	9	9	9	9	9	9	9	9
30	9	9	9	9	9	9	9	9	9	9	9	9
33	8	9	9	9	9	9	9	9	9	9	9	9
36	8	9	9	9	9	9	9	9	9	9	9	9
39	8	9	9	9	9	9	9	9	9	9	9	9
42	9	9	9	9	9	9	9	9	9	9	9	9
45	910	9	9	9	9	9	9	9	9	9	9	9
48	101010101010101010101010	9	9	9	9	9	9	9	9	9	9	9
51	10	91010	910101010101010	9	9	9	9	9	9	9	9	9
54	9101010	9	910101010101010	9	9	9	9	9	9	9	9	9
57	9101010	91010101010101010	9	9	9	9	9	9	9	9	9	9
60	10101010	91010101010101010	9	9	9	9	9	9	9	9	9	9
63	10101010	91010101010101010	9	9	9	9	9	9	9	9	9	9
66	9101010	91010101010101010	9	9	9	9	9	9	9	9	9	9
69	9101010	91010101010101010	9	9	9	9	9	9	9	9	9	9
72	101010101010101010101010	9	9	9	9	9	9	9	9	9	9	9
75	101010101010101010101010	9	9	9	9	9	9	9	9	9	9	9
78	101010101010101010101010	9	9	9	9	9	9	9	9	9	9	9
81	101010101010101010101010	9	9	9	9	9	9	9	9	9	9	9
84	101010101010101010101010	9	9	9	9	9	9	9	9	9	9	9
87	101010101010101010101010	9	9	9	9	9	9	9	9	9	9	9
90	1010	910101010101010101010	9	9	9	9	9	9	9	9	9	9
93	101010101010101010101010	9	9	9	9	9	9	9	9	9	9	9
96	101010101010101010101010	9	9	9	9	9	9	9	9	9	9	9

4-COMPONENT LOW FREQUENCY MAGNETOTELLURIC DATA  
ROSWELL, NEW MEXICO  
JUNE 13 (NOON)-17 (NOON), 1965 (TUCSUN TIME)

COHERENCY BETWEEN EY AND EY PREDICTED FROM H VIA IMPEDANCE TENSOR

FREQ TIME	11	15	20	26	35	46	61	8	109	145	*10***-5	CPS
3	101010101010101010101010	6	9	9	9	9	9	9	9	9	9	9
6	101010101010101010101010	9	9	9	9	9	9	9	9	9	9	9
9	101010101010101010101010	8	8	8	8	8	8	8	8	8	8	8
12	101010101010101010101010	9	9	9	9	9	9	9	9	9	9	9
15	7	91010	9	91010	9	9	9	9	9	9	9	9
18	7	91010	9	91010	9	9	9	9	9	9	9	9
21	7	9	9	9	9	9	9	9	9	9	9	9
24	9	9	9	9	9	9	9	9	9	9	9	9
27	9	9	9	9	9	9	9	9	9	9	9	9
30	8	9	9	9	9	9	9	9	9	9	9	9
33	8	9	9	9	9	9	9	9	9	9	9	9
36	8	9	9	9	9	9	9	9	9	9	9	9
39	9	9	9	9	9	9	9	9	9	9	9	9
42	9	91010	91010101010101010	9	9	9	9	9	9	9	9	9
45	9101010	9101010101010101010	9	9	9	9	9	9	9	9	9	9
48	10101010	9101010101010101010	9	9	9	9	9	9	9	9	9	9
51	10101010	9101010101010101010	9	9	9	9	9	9	9	9	9	9
54	10101010	9101010101010101010	9	9	9	9	9	9	9	9	9	9
57	9101010	9101010101010101010	9	9	9	9	9	9	9	9	9	9
60	9101010	9101010101010101010	9	9	9	9	9	9	9	9	9	9
63	101010101010101010101010	9	9	9	9	9	9	9	9	9	9	9
66	101010101010101010101010	9	9	9	9	9	9	9	9	9	9	9
69	10	91010101010101010101010	9	9	9	9	9	9	9	9	9	9
72	10	91010101010101010101010	9	9	9	9	9	9	9	9	9	9
75	101010101010101010101010	9	9	9	9	9	9	9	9	9	9	9
78	101010101010101010101010	9	9	9	9	9	9	9	9	9	9	9
81	10	910	910	9101010101010101010	9	9	9	9	9	9	9	9
84	101010101010101010101010	9	9	9	9	9	9	9	9	9	9	9
87	1010	910	910	9101010101010101010	9	9	9	9	9	9	9	9
90	1010	91010101010101010101010	9	9	9	9	9	9	9	9	9	9
93	101010101010101010101010	9	9	9	9	9	9	9	9	9	9	9
96	101010101010101010101010	9	9	9	9	9	9	9	9	9	9	9

Figure 3.7 Electric field predictability, Roswell, N.M.

in Figure 3.6) is due to the pronounced magnetic storm shown on Figure 3.5. This increase accompanies an increase in the E predictability coherencies and indicates that "better" data results from times of high signal level. Note that the  $E_x$  predictability remains high while the  $E_x H_y$  coherency is scattered. The low power and high coherencies for the first few time periods are unreal, due to the finite response time of the recursive filters; however, the consistently low E predictability at high frequencies suggests that the data is noisy.

Examples of time variations of the E predictability coherency and apparent resistivity estimates are shown in Figure 3.8. Note that the tensor apparent resistivities are more stable than the Cagniard apparent resistivities, as predicted for an anisotropic impedance, and that scatter is reduced when the E predictability is high. Decreases in the apparent resistivity estimates are associated with low E predictabilities, although the actual decreases are larger than predicted.

The principal axis criterion of maximizing  $Z'_{12}$  yielded principal directions, E-H phase differences and principal value apparent resistivities which were consistent during periods of high E predictability and was used to obtain the



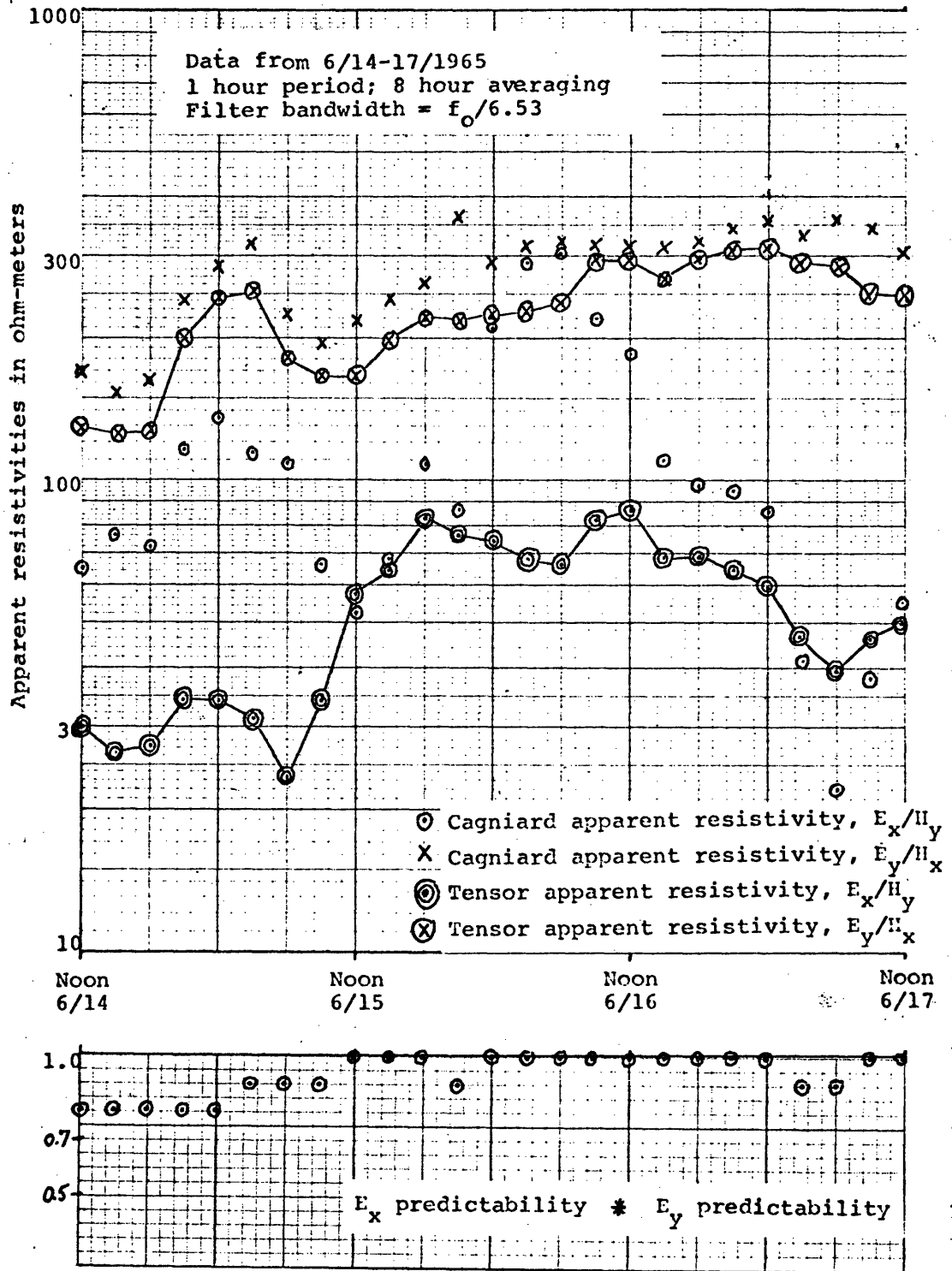
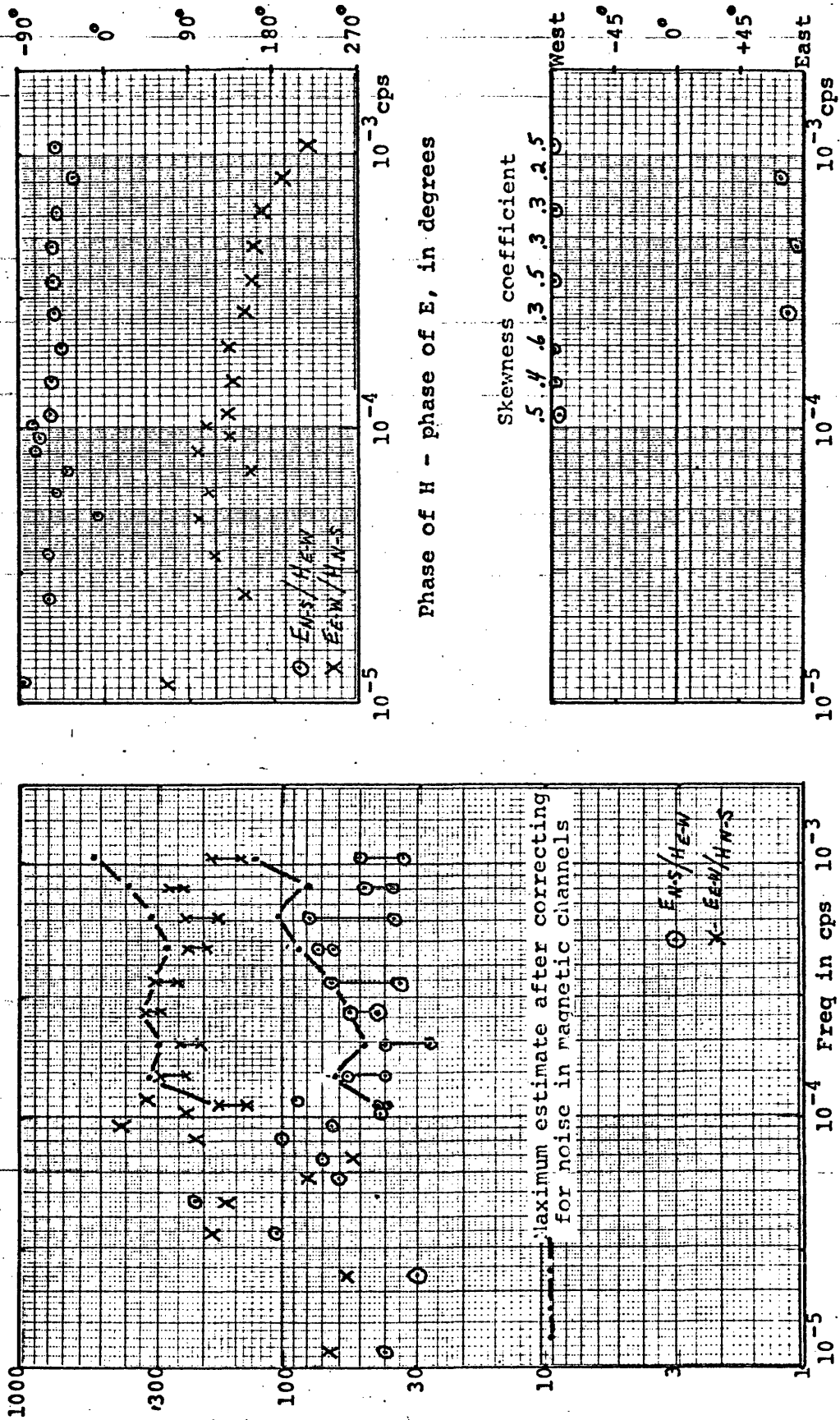


Figure 3.8 Time consistency of apparent resistivity estimates, Roswell, New Mexico.

final apparent resistivity estimates. From the sonogram analysis, data sections of 18 hours duration were selected in which the E predictability was high ( $>80\%$ ). With the prime requisite of high E predictability, these 18 hour sections were chosen such that the  $H_x H_y$  coherency was low. The values for the E-H phase difference and for the principal direction were averaged to form the final estimates. These values, along with the maximum and minimum values for the apparent resistivities over the 18 hour section, are plotted in Figure 3.9. Therefore, the range bars in the plotted apparent resistivity values signify scatter, not estimated error.

Also indicated in Figure 3.9, and included in all following apparent resistivity figures, is a correction for H field noise at the high frequencies. As discussed at the end of Section 3.3, a low E predictability probably indicates the presence of noise. Assuming that this noise is incoherently added to both magnetic channels and that it affects the individual tensor elements equally, a correction factor for the apparent resistivity estimates can be calculated from the E predictabilities. This corrected apparent resistivity represents a maximum for the estimated value. The overall effect of this correction is to up the apparent



Apparent resistivities, E-H phases, principal directions, and skewness coefficients for Poswell, New Mexico

Figure 3.9 Magnetotelluric apparent resistivities, E-H phases, principal directions, and skewness coefficients for Poswell, New Mexico

~~resistivity curve for frequencies over  $0.35 \times 10^{-3}$  cps.~~

The principal direction, corresponding to the direction of the greater principal value apparent resistivity, is computed from the Roswell data as E-W. Therefore, standard Cagniard apparent resistivities and E-H phase differences for the frequency range  $10^{-5}$  to  $10^{-4}$  cps were calculated on data rotated 0 degrees, as outlined in the last section, and are included on Figure 3.9. Note the increased scatter in the estimates at these low frequencies.

The skewness coefficient, the two-dimensionality measure of equation 2.5-14, is averaged for the impedance tensors of the 18 hour section and is included in Figure 3.9 above the principal directions. The average skewness coefficient of 0.4 for the Roswell data indicates that the E-W principal direction may be in error. Electric and magnetic field polarization ellipses, or hodographs, which are shown in Figure 3.10 both for unfiltered data and for filtered frequency components, show a roughly linear polarization of the electric field striking roughly  $N70^{\circ}E$ . The skewness coefficient is probably reflecting the discrepancy between this direction and the computed principal direction.

The Roswell telluric data were also analyzed with magnetic data from Dallas. Although the E predictability

is not significantly improved and the apparent resistivities are comparable (see Figure 3.11), the principal direction is now calculated at  $N70^{\circ}E$  and the skewness coefficient is now about 0.2. A slight rotation of the magnetic field ellipse between Dallas and Tucson could produce this difference in the principal direction without affecting the high coherency and small phase shifts as shown in Figure 3.3.

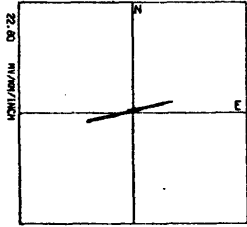
Figure 3.10 - Electric and magnetic field hodographs,  
Roswell, New Mexico

For a homogeneous earth, Maxwell's equations predict the electric field to be orthogonally related to the magnetic field. For inhomogeneous conductivity structure, a preferred current direction exists either perpendicular or parallel to the structural strike. In the upper left, six hours of unfiltered data shows the magnetic storm sudden commencement. Individual frequency polarization ellipses below show the pronounced preferred direction for the electric field. In the upper right, a quiet-day diurnal variation is plotted. In the lower right, unfiltered and filtered polarization ellipses from a more randomly polarized signal also indicate the  $N70^{\circ}E$  preferred direction. Note that

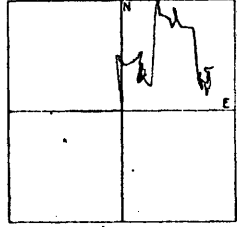
.000128 cps = 2.5 hr period

.001253 cps = 15 min period

4-COMPONENT LOW FREQUENCY MAGNETOTELLURIC DATA  
ROSWELL, NEW MEXICO  
DC- 0.002 CPS 0-600 6/15/1965

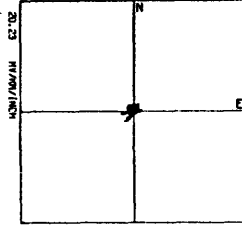


ELECTRIC POL ELLIPSE

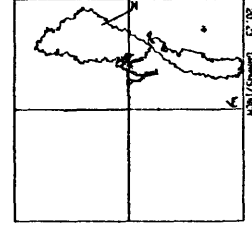


MAGNETIC POL ELLIPSE

4-COMPONENT LOW FREQUENCY MAGNETOTELLURIC DATA  
ROSWELL, NEW MEXICO  
DC- 0.002 CPS JUNE 13, 1965

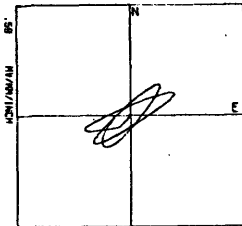


ELECTRIC POL ELLIPSE

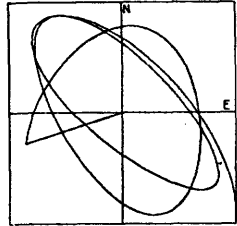


MAGNETIC POL ELLIPSE

4-COMPONENT LOW FREQUENCY MAGNETOTELLURIC DATA  
ROSWELL, NEW MEXICO  
JUNE 13 (NOON)-17 (NOON), 1965 (TUCSON TIME)  
SIX HOUR SEGMENT NO. 7 FREQ= .000128 CPS

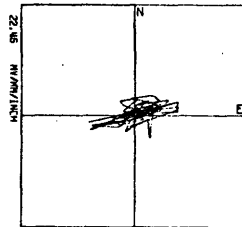


ELECTRIC POL ELLIPSE

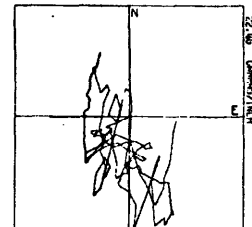


MAGNETIC POL ELLIPSE

4-COMPONENT LOW FREQUENCY MAGNETOTELLURIC DATA  
ROSWELL, NEW MEXICO  
DC- 0.002 CPS 1800-2400 6/15/1965

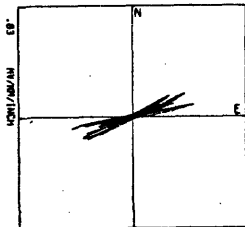


ELECTRIC POL ELLIPSE

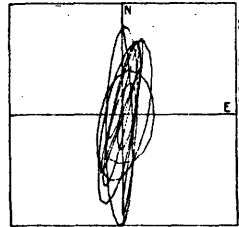


MAGNETIC POL ELLIPSE

4-COMPONENT LOW FREQUENCY MAGNETOTELLURIC DATA  
ROSWELL, NEW MEXICO  
JUNE 13 (NOON)-17 (NOON), 1965 (TUCSON TIME)  
SIX HOUR SEGMENT NO. 7 FREQ= .000401 CPS

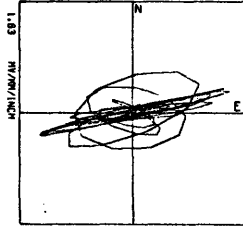


ELECTRIC POL ELLIPSE

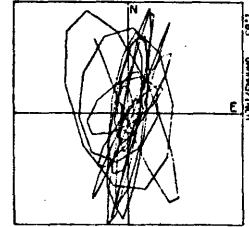


MAGNETIC POL ELLIPSE

4-COMPONENT LOW FREQUENCY MAGNETOTELLURIC DATA  
ROSWELL, NEW MEXICO  
JUNE 13 (NOON)-17 (NOON), 1965 (TUCSON TIME)  
SIX HOUR SEGMENT NO. 10 FREQ= .000709 CPS

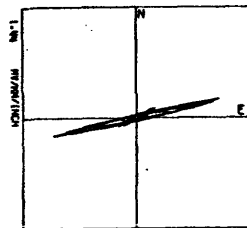


ELECTRIC POL ELLIPSE

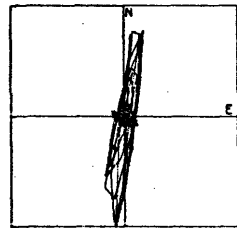


MAGNETIC POL ELLIPSE

4-COMPONENT LOW FREQUENCY MAGNETOTELLURIC DATA  
ROSWELL, NEW MEXICO  
JUNE 13 (NOON)-17 (NOON), 1965 (TUCSON TIME)  
SIX HOUR SEGMENT NO. 7 FREQ= .001253 CPS

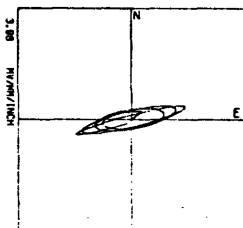


ELECTRIC POL ELLIPSE

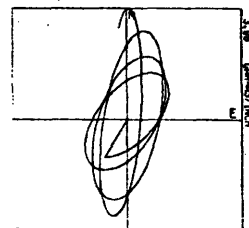


MAGNETIC POL ELLIPSE

4-COMPONENT LOW FREQUENCY MAGNETOTELLURIC DATA  
ROSWELL, NEW MEXICO  
JUNE 13 (NOON)-17 (NOON), 1965 (TUCSON TIME)  
SIX HOUR SEGMENT NO. 10 FREQ= .000170 CPS



ELECTRIC POL ELLIPSE



MAGNETIC POL ELLIPSE

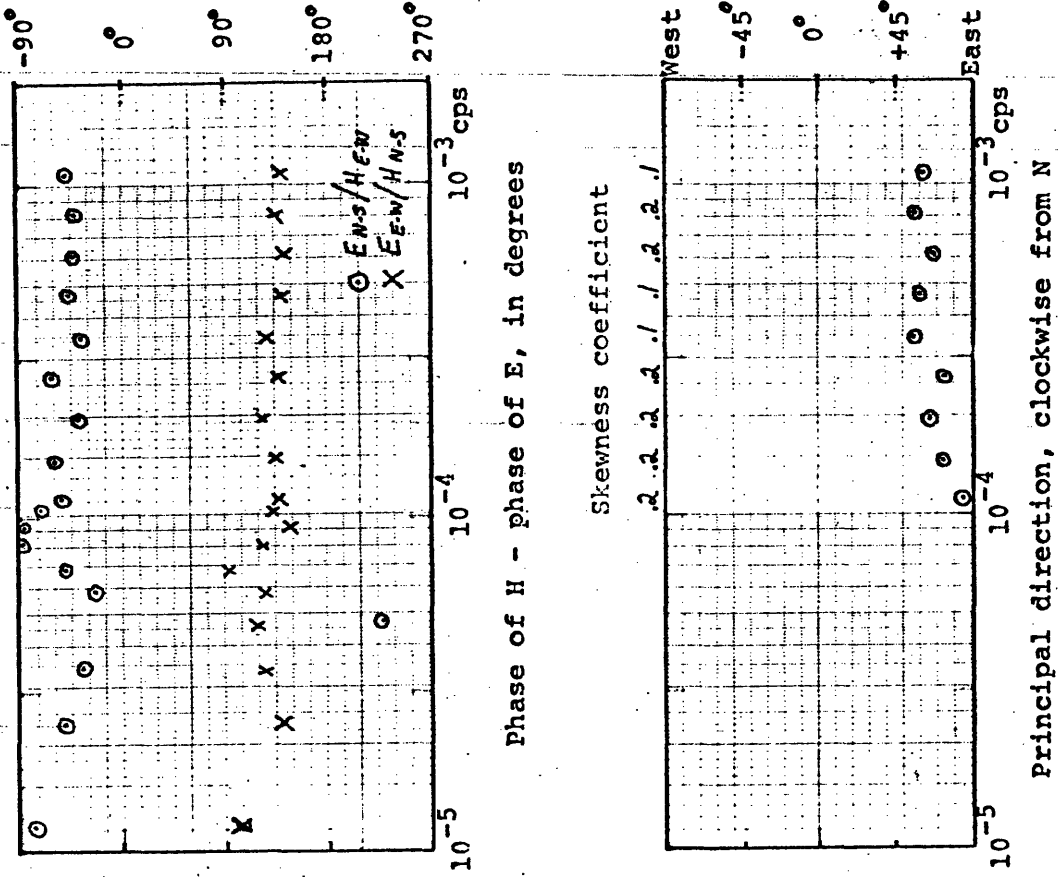


Figure 3.11 Magnetotelluric apparent resistivity estimates using Dallas magnetics, Roswell, New Mexico

Apparent resistivities in ohm-meters

Principal direction, clockwise from N

Maximum estimate after correcting for noise in magnetic channels

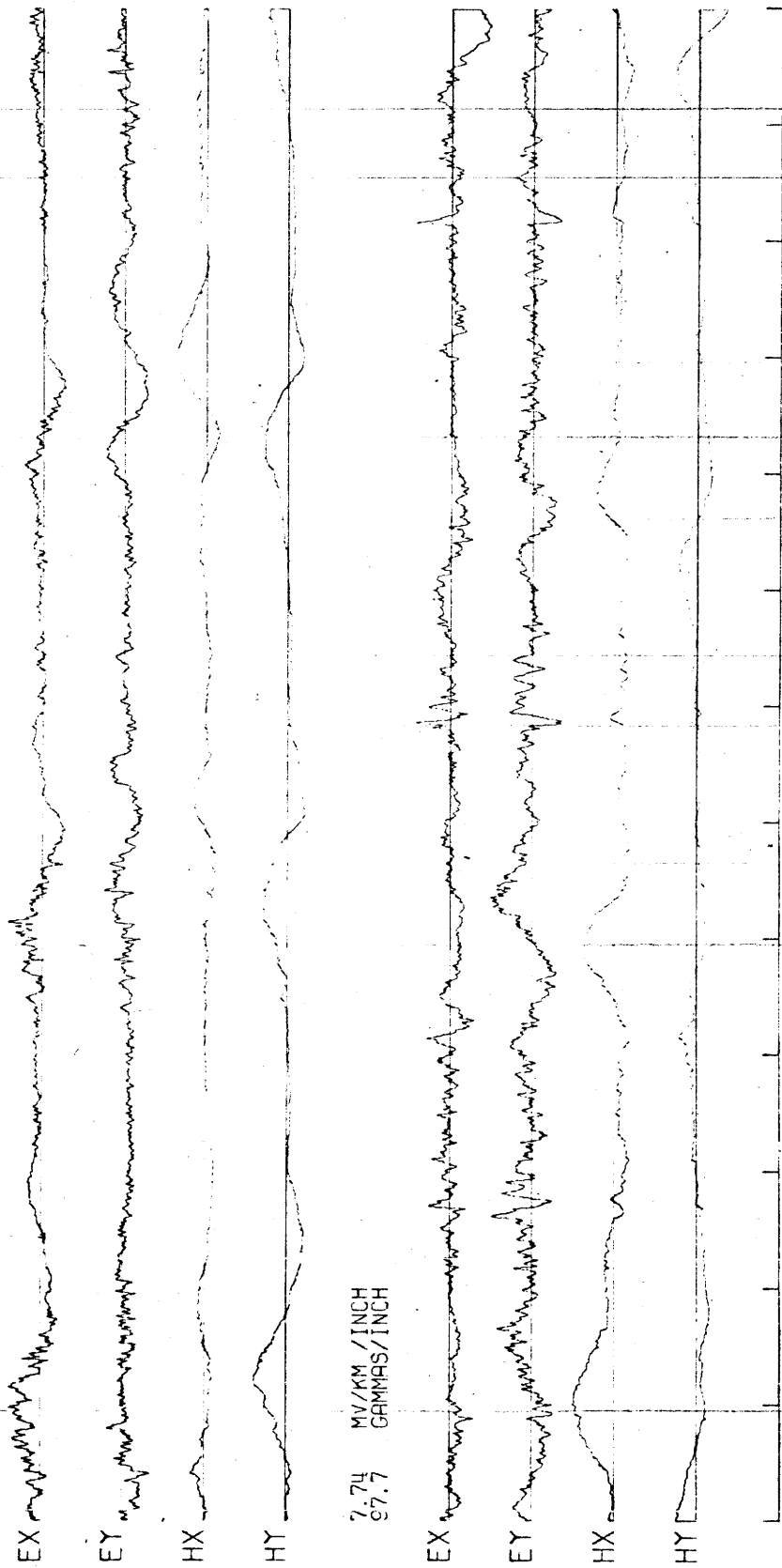
$\circ E_{NS}/H_{EW}$   
 $\times E_{EW}/H_{NS}$



Deming, New Mexico

The usefulness of the tensor impedance approach is indicated by the results of the analysis of the magnetotelluric field data from Deming, which are plotted in Figure 3.12. The Cagniard apparent resistivities are equal for N-S and E-W reference axes, suggesting an isotropic impedance and a layered-earth structure. Tensor analysis, however, yields a principal direction of  $N45^{\circ}W$  and anisotropic apparent resistivities for reference axes rotated into that direction. The apparent resistivities, E-H phases, principal directions and skewness coefficients for Deming are plotted in Figure 3.13. The low skewness coefficients suggest that the conductivity structure at Deming can be considered two-dimensional.

The principal direction of  $N45^{\circ}W$  is similarly indicated as the preferred direction in the electric and magnetic field hodographs for the Deming data, shown in Figure 3.14. For example, for the 0.00017 cps (2 hr.) frequency component plotted in the lower left of the figure, the strongly elliptically polarized magnetic field and the circularly polarized electric field indicate a NW preferred electric field direction for a circularly polarized magnetic field.



4-COMPONENT LOW FREQUENCY MAGNETOTELLURIC DATA  
 DEMING, NEW MEXICO  
 JUNE 8-14 (NOON), 1966  
 (TUCCSON TIME)

7.74 MV/KM / INCH  
 97.7 GAMMAS / INCH

Figure 3.12 Magnetotelluric field data, Deming, N.M.

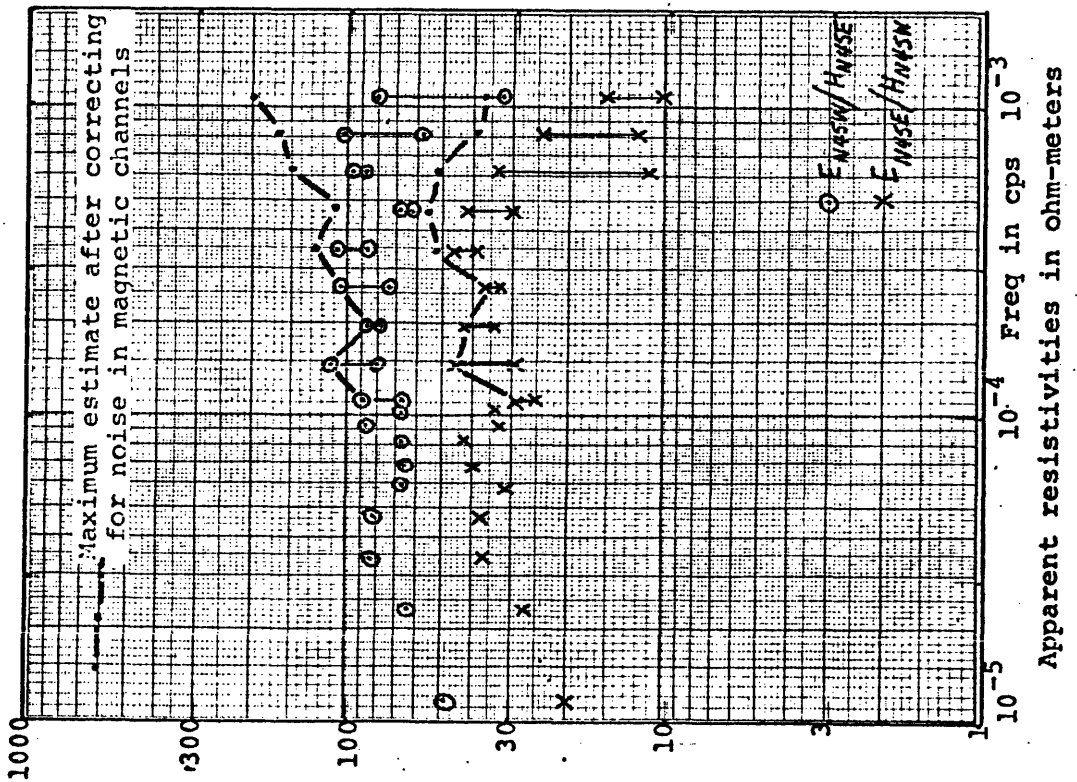
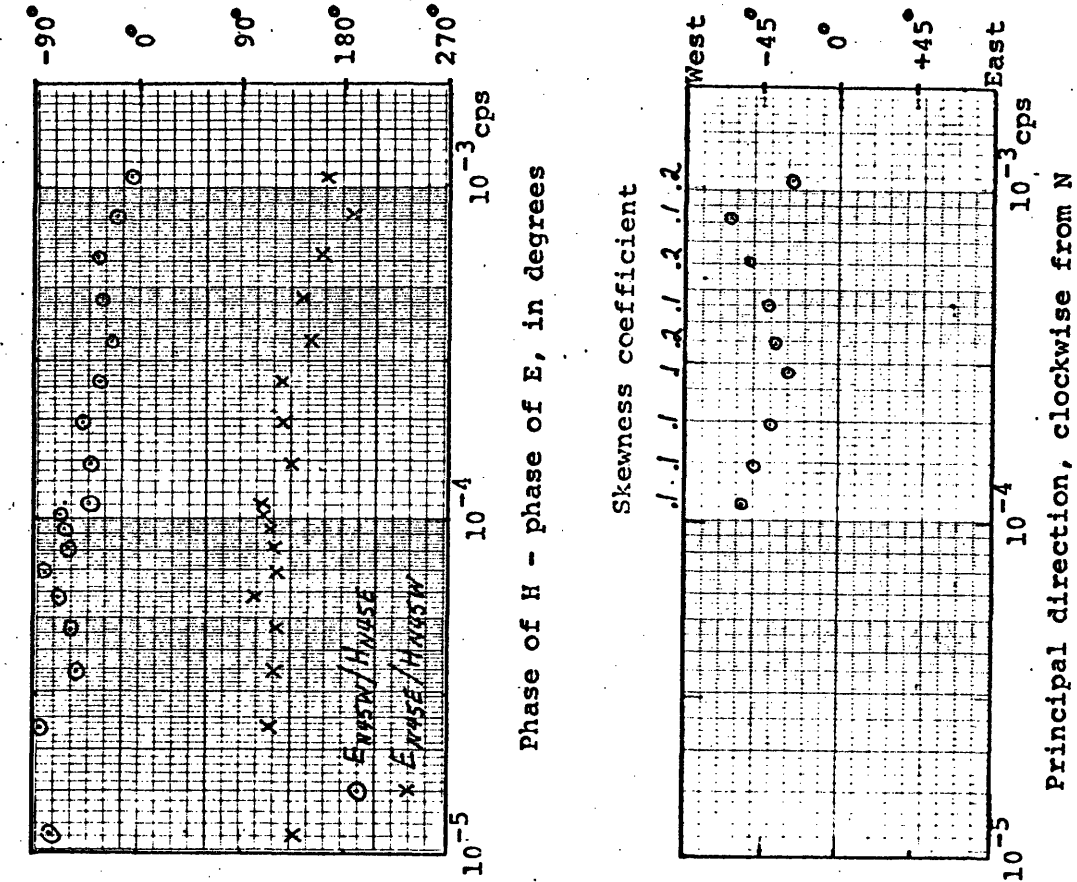
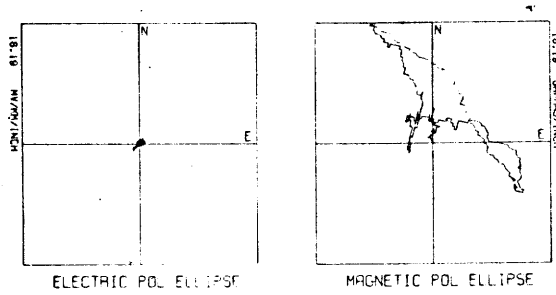


Figure 3.13 Magnetotelluric apparent resistivities, E-H phases, principal directions, and skewness coefficients for Deming, New Mexico

4-COMPONENT LOW FREQUENCY MAGNETOTELLURIC DATA  
DEMING, NEW MEXICO  
DC- 0.002 CPS 000-2400 6/10/1966



4-COMPONENT LOW FREQUENCY MAGNETOTELLURIC DATA  
DEMING, NEW MEXICO  
DC- 0.002 CPS 1800-2400 6/11/1966

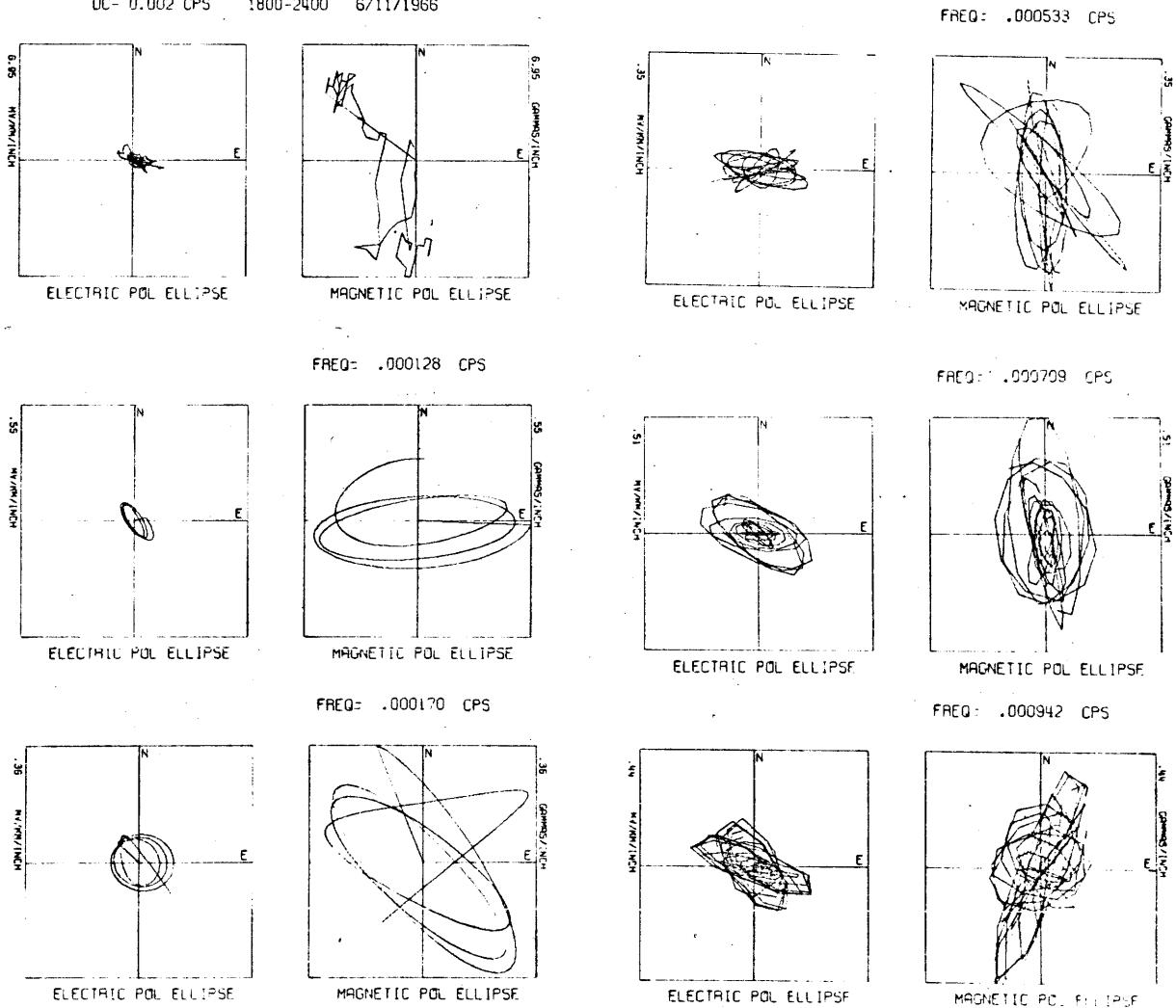
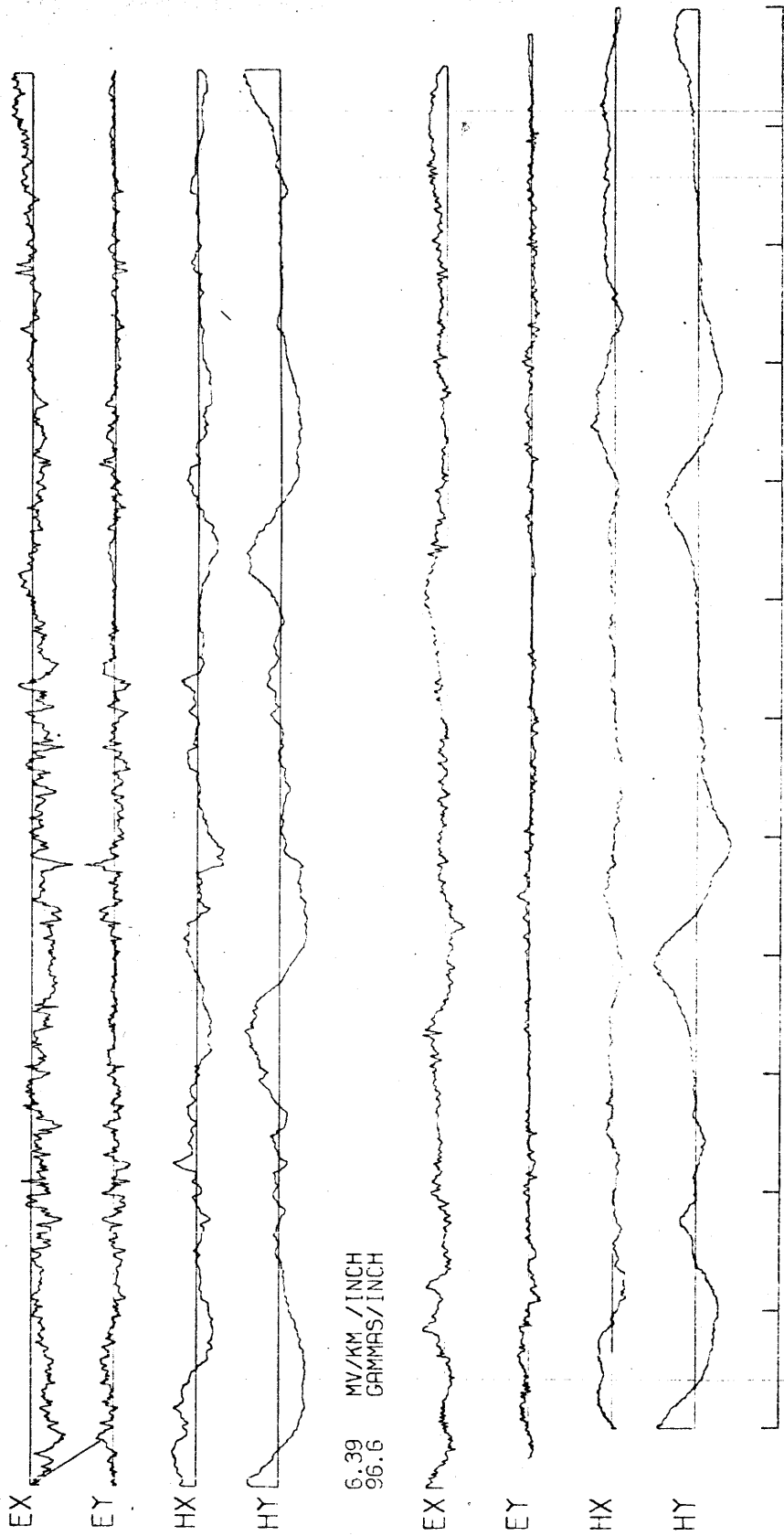


Figure 3.14 Electric and magnetic field hodographs, Deming, N.M.

Safford, Arizona

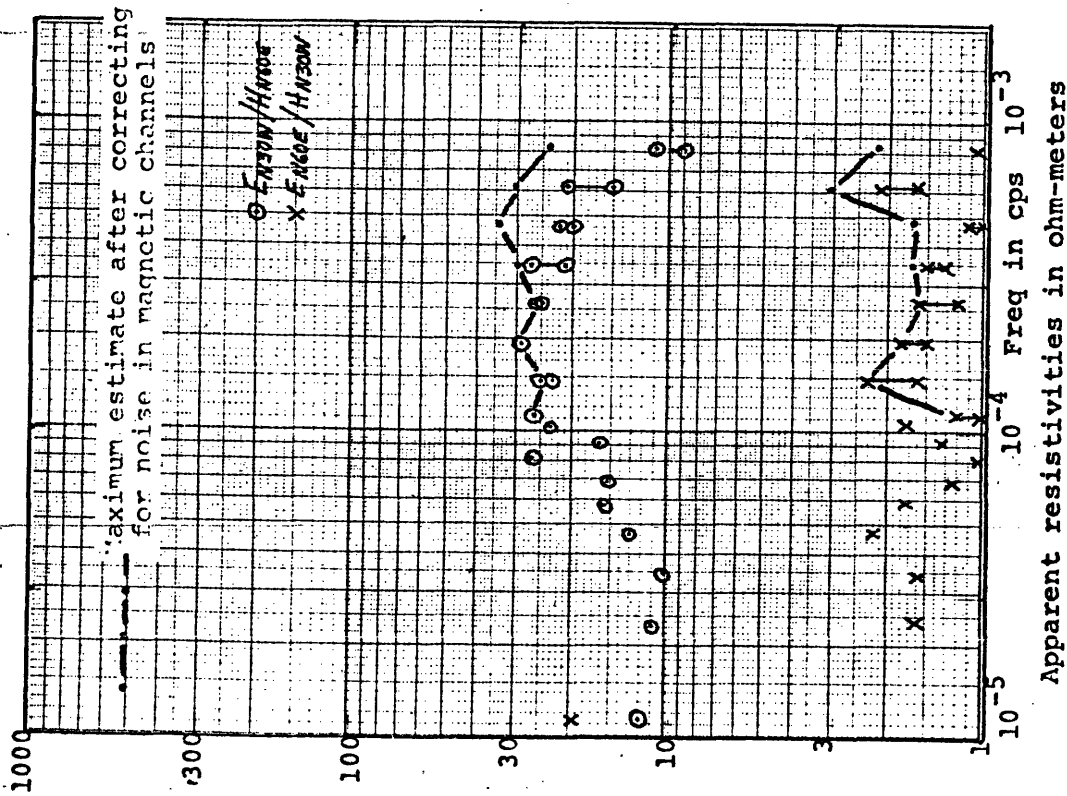
The magnetotelluric field data for Safford are plotted in Figure 3.15. The resultant measured apparent resistivities, E-H phases, principal directions, and skewness coefficients are shown in Figure 3.16. The apparent resistivities are strongly anisotropic; the skewness coefficients indicate a good approximation to two-dimensionality. A calculated principal direction of  $N30^{\circ}E$  corresponds to the preferred current direction indicated by the field hodographs of Figure 3.17.

Both the apparent resistivity and the phase estimate for the diurnal frequency for the  $E(N60^{\circ}E)/H(N30^{\circ}W)$  component appear to be in error, possibly due to spectral spill-over, and should not be relied upon.

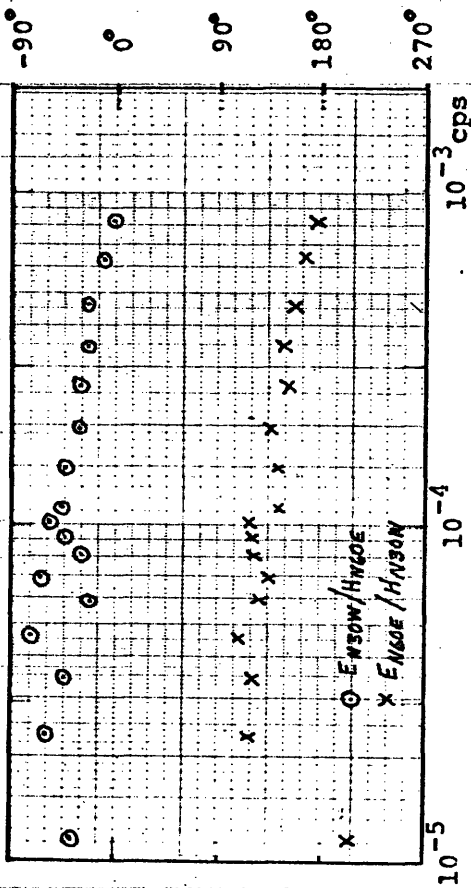


4-COMPONENT LOW FREQUENCY MAGNETOTELLURIC DATA  
SAFFORD, ARIZONA  
JUNE 29(9AM)-JULY 5(9AM), 1965 (TUCCSON TIME)

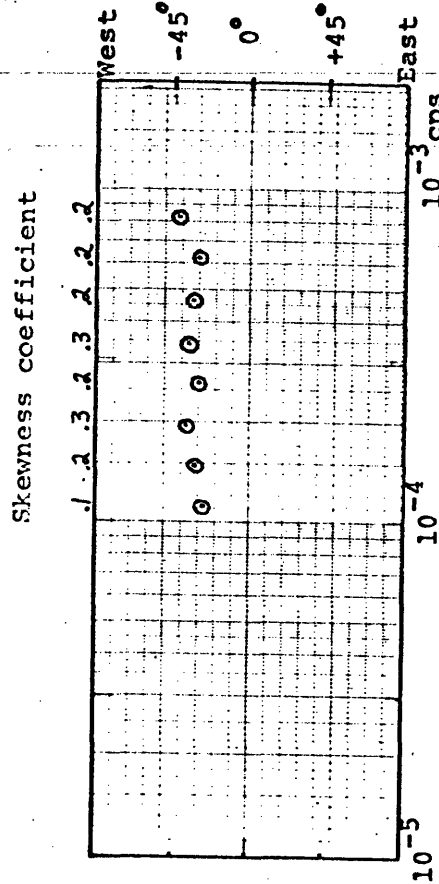
Figure 3.15 Magnetotelluric field data, Safford, Arizona



Apparent resistivities in ohm-meters



Phase of H - phase of E, in degrees



Skewness coefficient

Principal direction, clockwise from N

Figure 3.16 Magnetotelluric apparent resistivities, E-H phases, principal directions, and skewness coefficients for Safford, Arizona

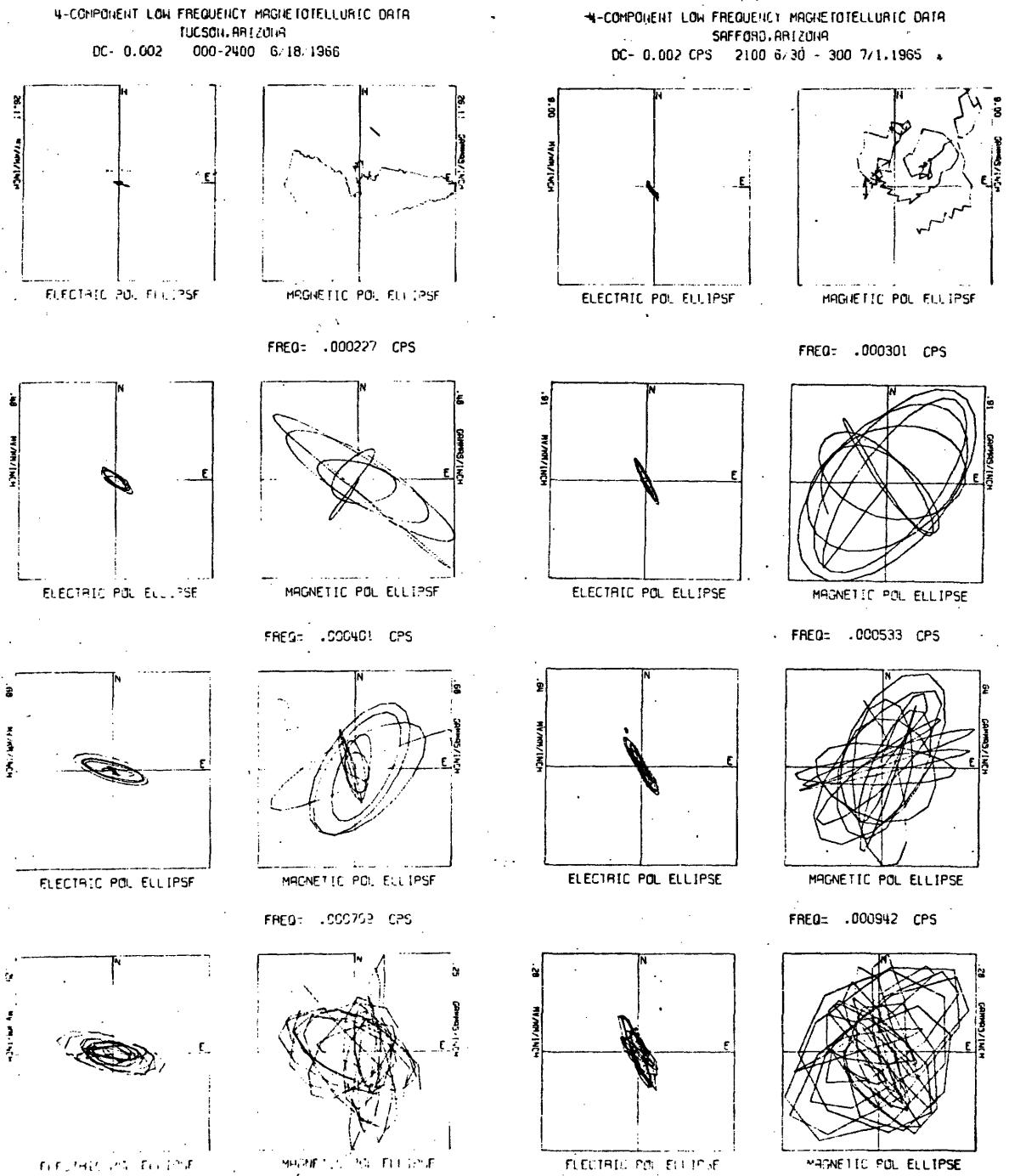


Figure 3.17 Electric and magnetic field hodographs, Safford and Tucson, Arizona



Tucson, Arizona

The magnetotelluric data for Tucson are plotted in Figure 3.18. Although the higher frequency signal level appears to be low, similar results were obtained for the higher frequencies from another short data segment of higher signal level. Measured apparent resistivities, E-H phases, principal directions, and skewness coefficients are shown in Figure 3.19.

Although both the calculated principal directions and the preferred current directions, inferred from Figure 3.17, are consistently N60°W, the high skewness coefficients indicate that this principal direction may be misleading and that the subsurface conductivity structure cannot be considered two-dimensional. The high scatter in the weaker apparent resistivity estimates reflects the lack of accuracy expected for highly anisotropic data.

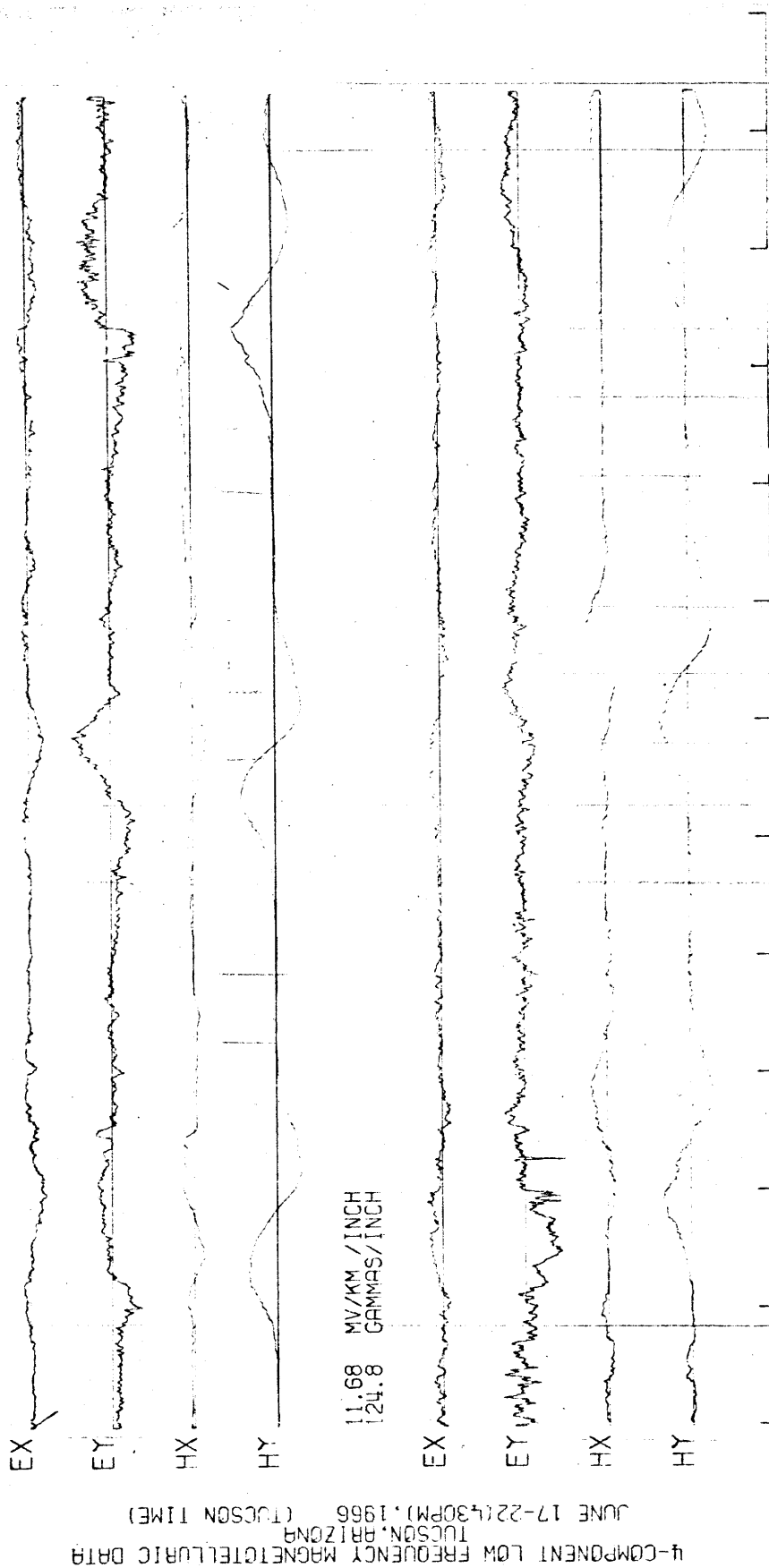


Figure 3.18 Magnetotelluric field data, Tucson, Ariz.

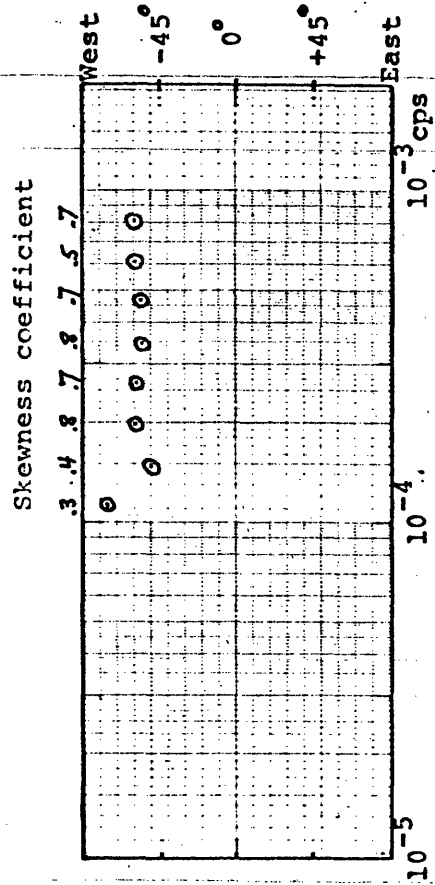
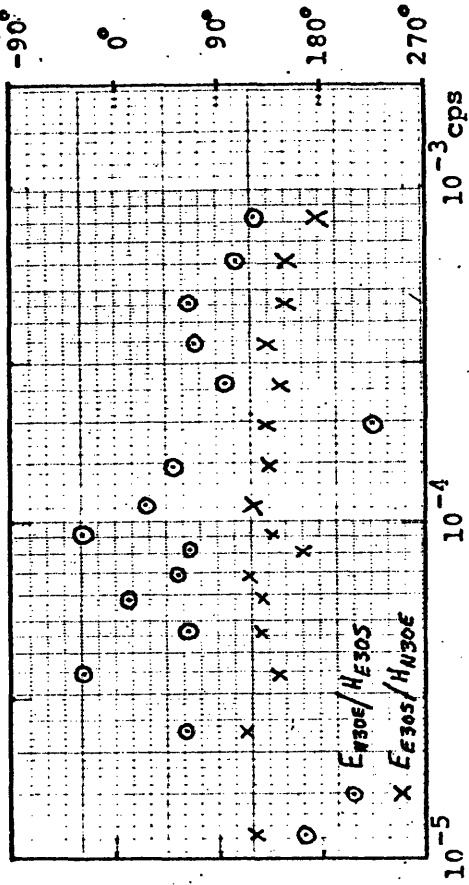
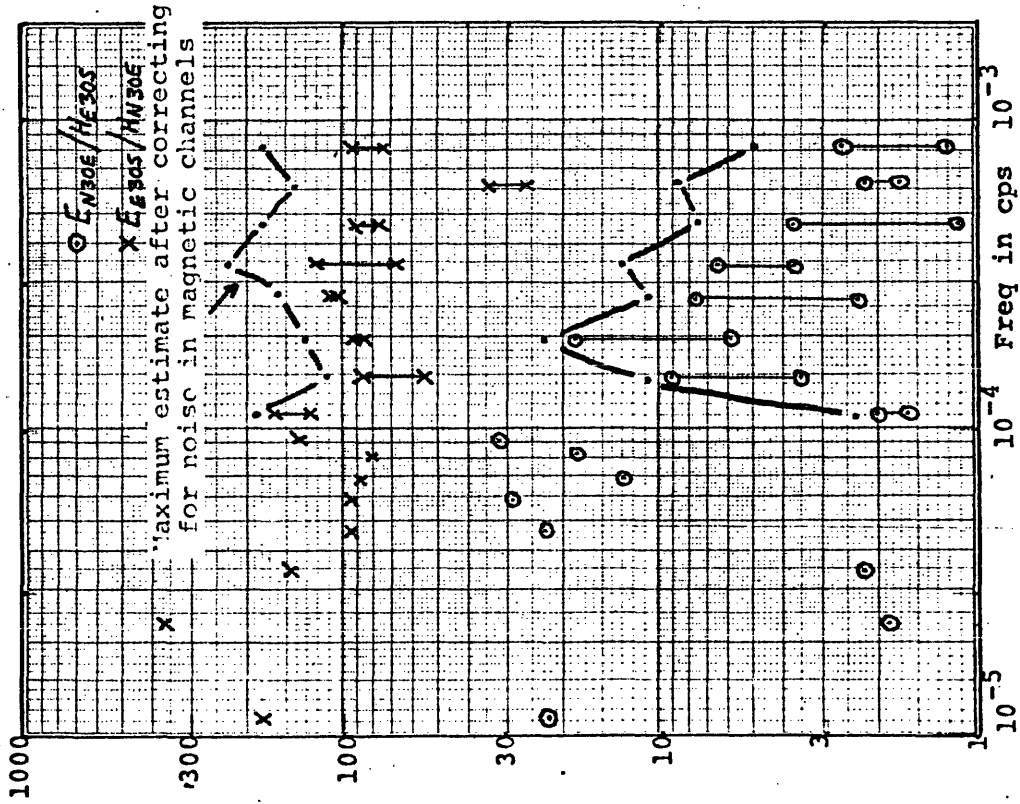
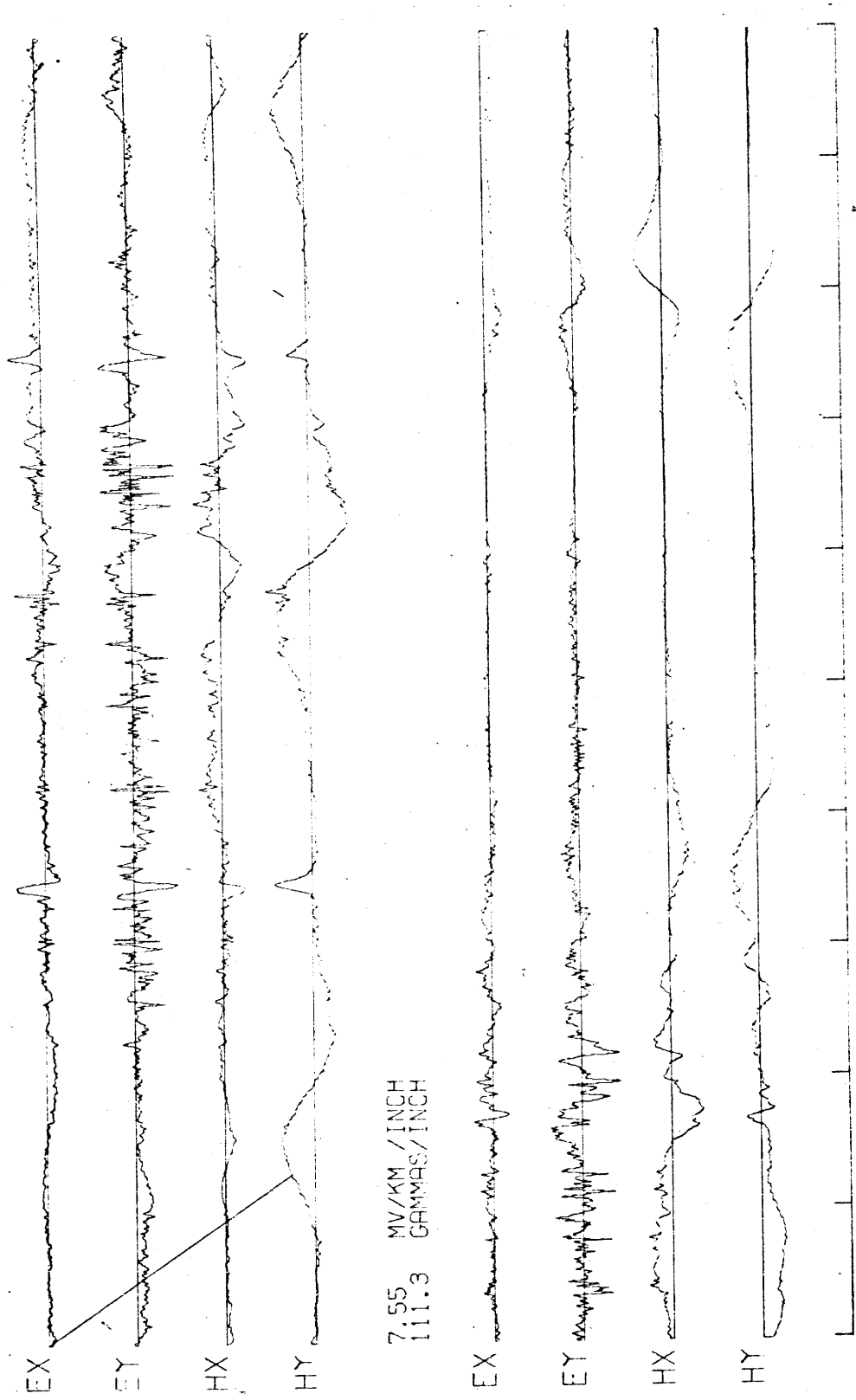


Figure 3.19 Magnetotelluric apparent resistivities, E-H phases, principal directions, and skewness coefficients for Tucson, Arizona

Phoenix, Arizona

As indicated in Table 3.1, two different sets of data were obtained at Phoenix, corresponding to two different electrode configurations at two different measuring periods. The magnetotelluric field data from Phoenix for 1965 are plotted in Figure 3.20, and for 1966 in Figure 3.21. The computed apparent resistivities, E-H phases, principal directions, and skewness coefficients for the two data sets are shown in Figures 3.22 and 3.23. Principal directions of  $N60^{\circ}W$  for the 1965 data and  $N30^{\circ}W$  for the 1966 data are consistent with the polarization ellipses of Figure 3.24.

Although apparent resistivities and principal directions are different for each set, the low skewness coefficients indicate good two dimensionality for both sites. The difference is due to the sensitivity of the measured apparent resistivities to the exact location of the electrodes in areas of considerable surface conductivity structure. This effect will be elaborated upon in the next section.



4-COMPONENT LOW FREQUENCY MAGNETOTELLURIC DATA  
PHOENIX, ARIZONA  
JULY 6(11PM)-11(11PM), 1965 (TUCCSON TIME)

7.55 MV/KM / INCH  
111.3 GAMMAS/INCH

Figure 3.20 Magnetotelluric field data, July 1965, Phoenix, Ariz.

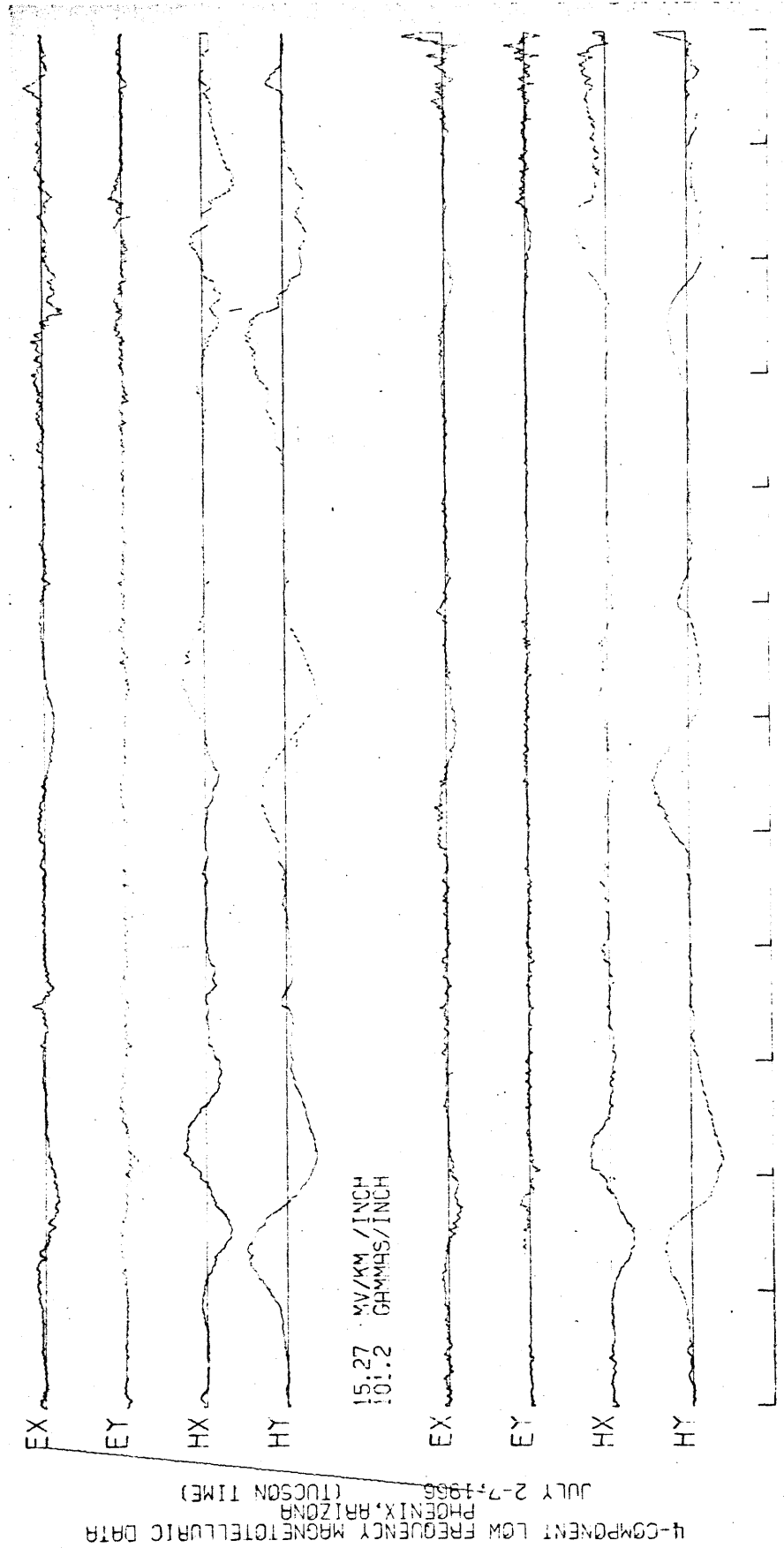
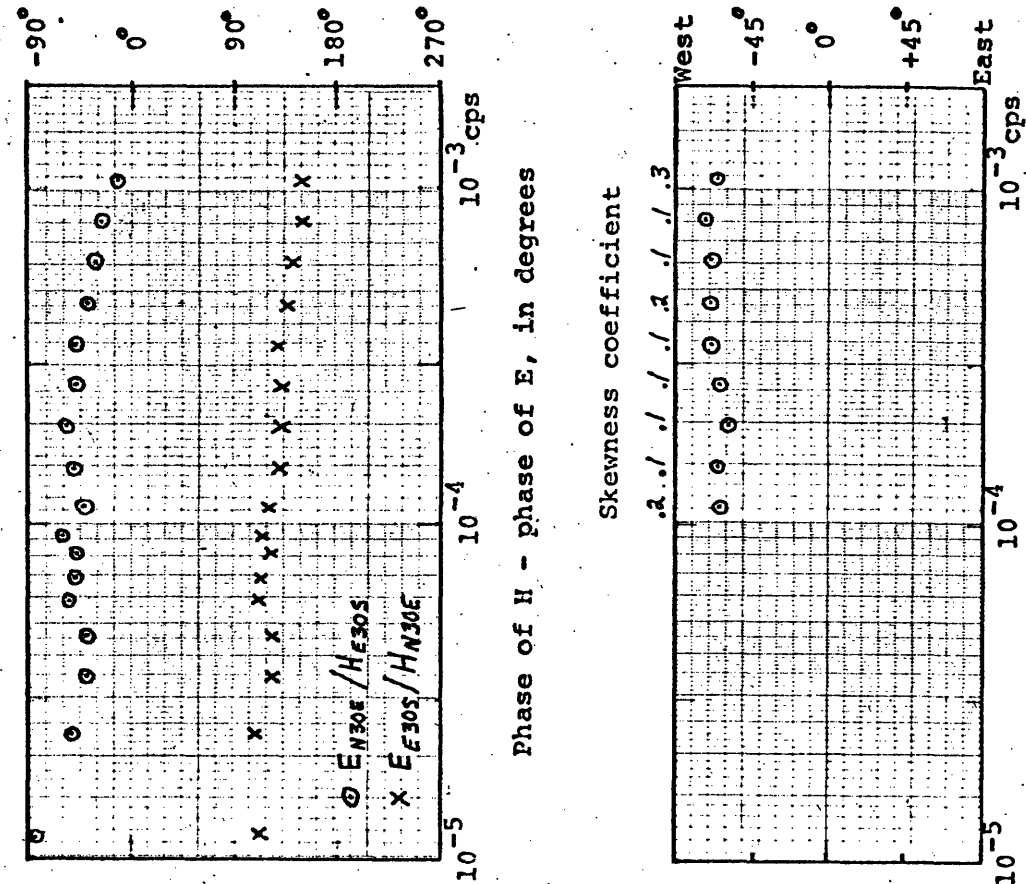
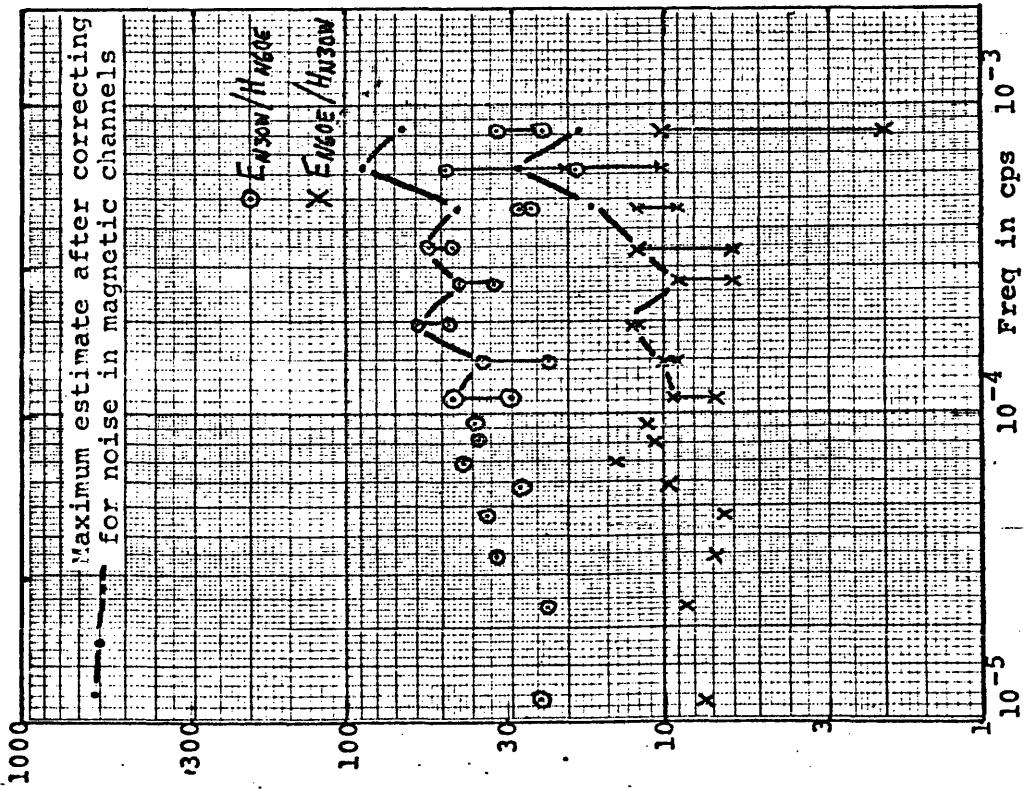


Figure 3.21 Magnetotelluric field data, July 1966, Phoenix, Ariz.



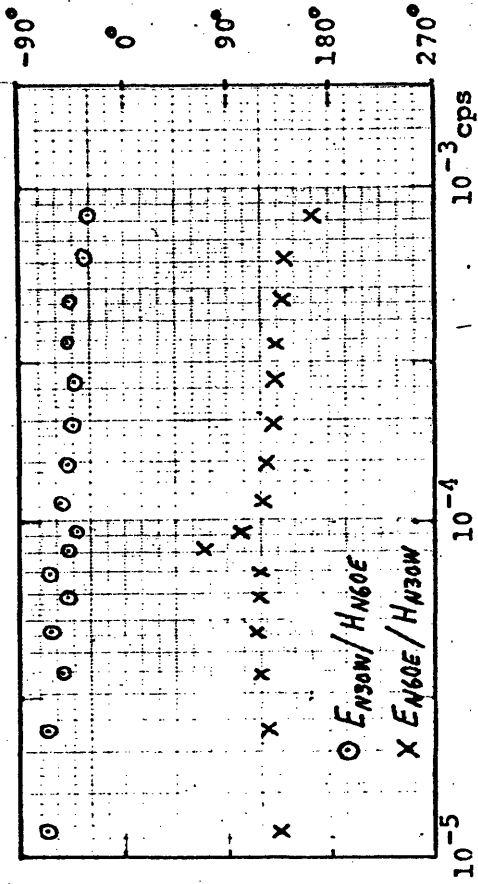
Principal direction, clockwise from N

Figure 3.22 Magnetotelluric apparent resistivities, E-H phases, principal directions, and skewness coefficients for 1965 site at Phoenix, Arizona.



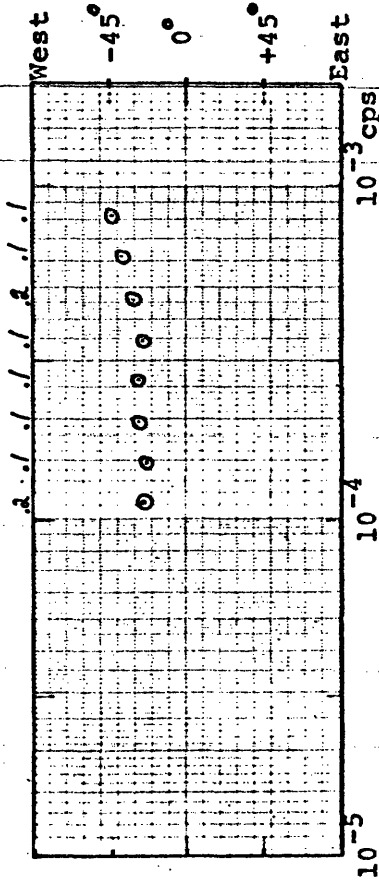
Apparent resistivities in ohm-meters

Figure 3.23 Magnetotelluric apparent resistivities, E-H phases, principal directions, and skewness coefficients for 1966 site at Phoenix, Arizona



Phase of H - phase of E, in degrees

Skewness coefficient



Principal direction, clockwise from N



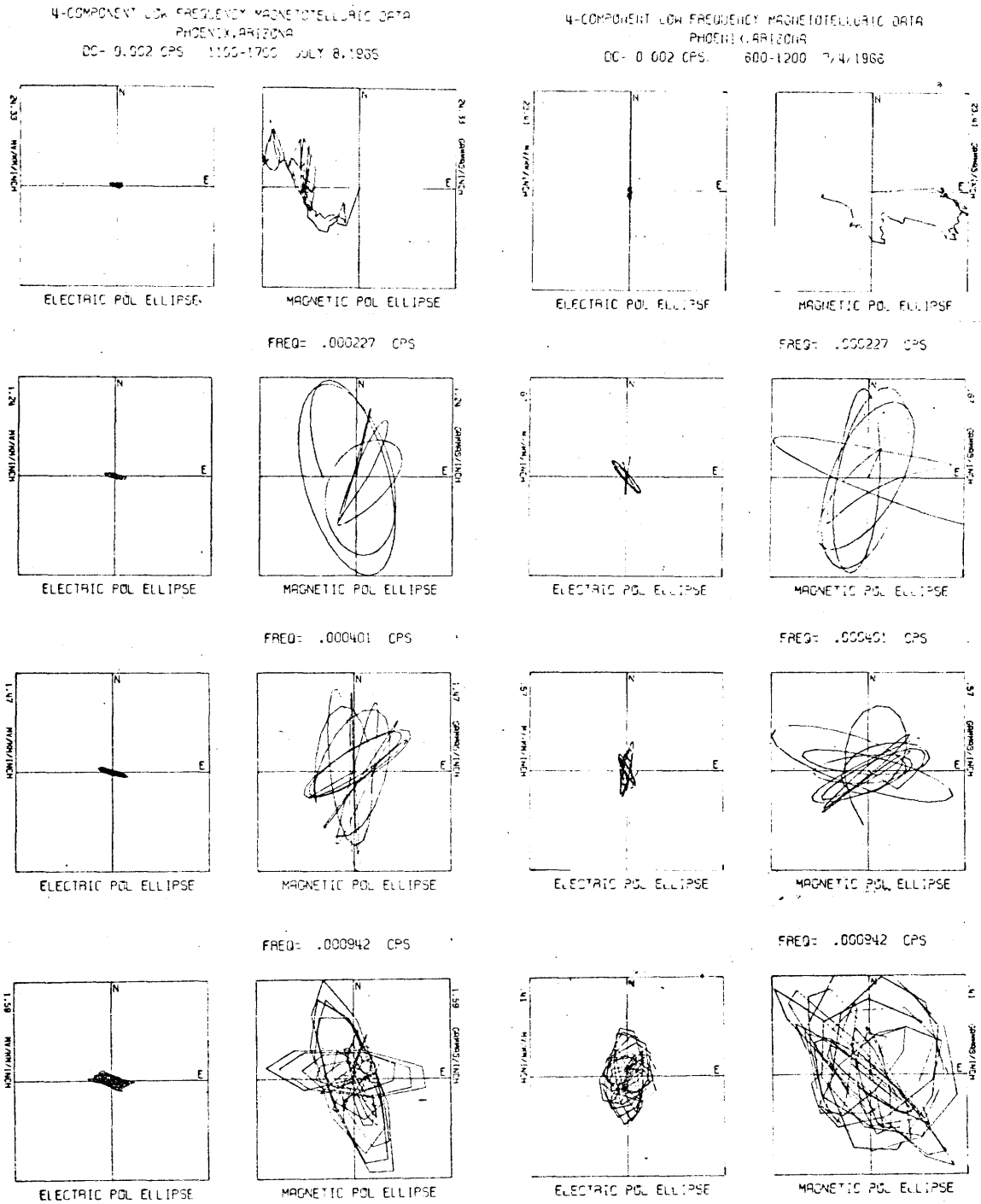


Figure 3.24 Electric and magnetic field hodographs, Phoenix, Ariz.

Yuma, Arizona

The magnetotelluric field data for Yuma are plotted in Figure 3.25. The meaningless E-H phases and highly scattered apparent resistivities shown in Figure 3.26 are associated with good E predictabilities, but with very high skewness coefficients.

Geologically, the structure near Yuma is roughly two-dimensional, with a dominant strike of  $N40^{\circ}W$  associated with the Salton Sea - Gulf of California graben. But the location of the non-orthogonal dipole spreads, one within conductive sediments (Yuma-Somerton) and one spanning a contact between these sediments and the resistive mountains to the northeast (Yuma-Liguria), were such that the measured voltages could not be used to define an E vector at one position, as discussed in Section 2.5. Rotation of the raw measured voltages into orthogonal reference axes restricts the signal to be perpendicular to the weak component. The resulting tensor operations are greatly distorted and the skewness coefficients are high.

For the computed results of Figure 3.26, the reference axes used were along  $(E11^{\circ}S)$  and perpendicular to  $(N11^{\circ}E)$  the strong signal direction and the results are dominated by this strong signal. Therefore, the greater apparent

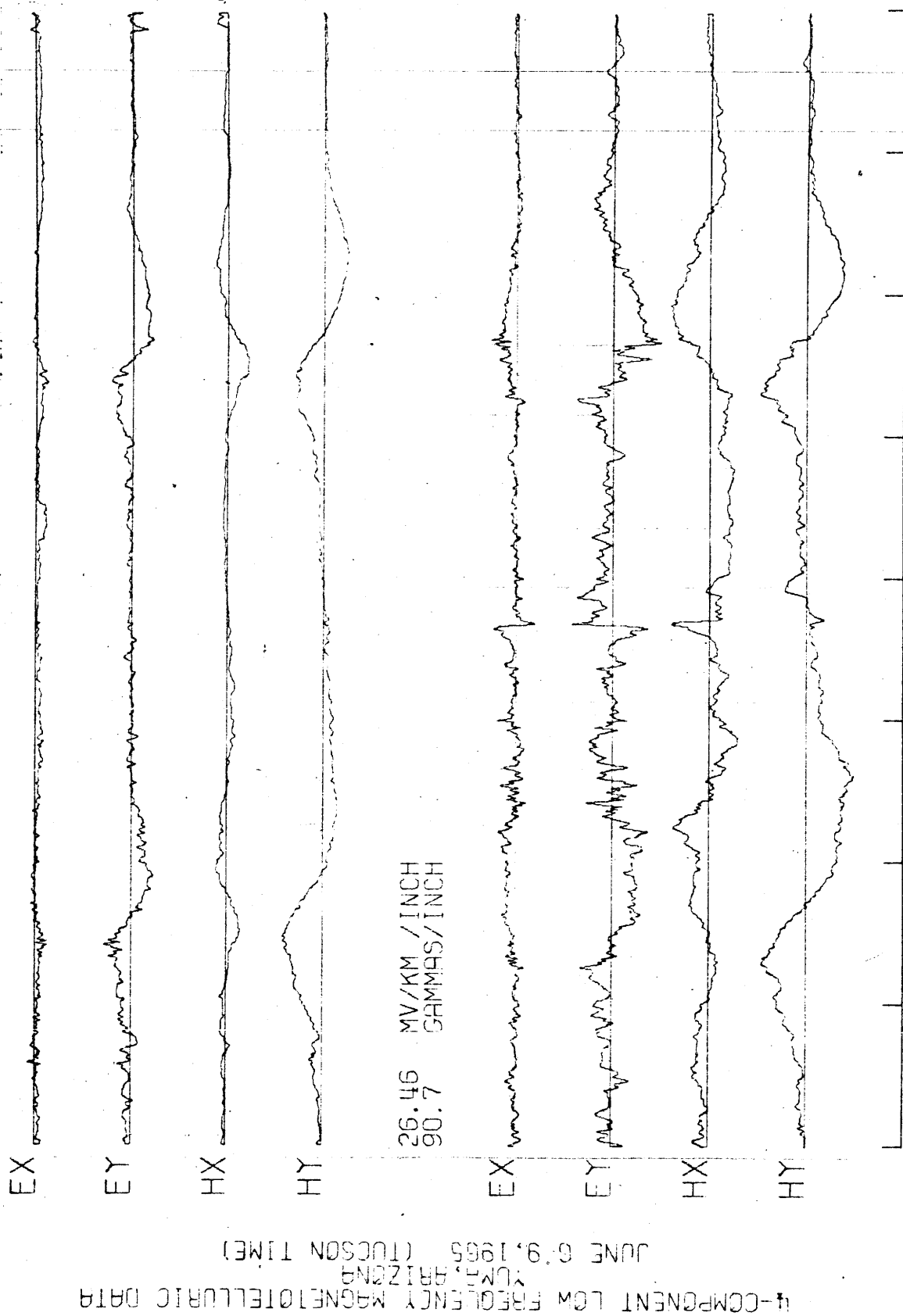
resistivity is representative for the across the strike

estimate; the lower apparent resistivity is meaningless.

The increasing apparent resistivity at the diurnal period

is a very anomalous result and requires an unusual

theoretical model to yield comparable values.



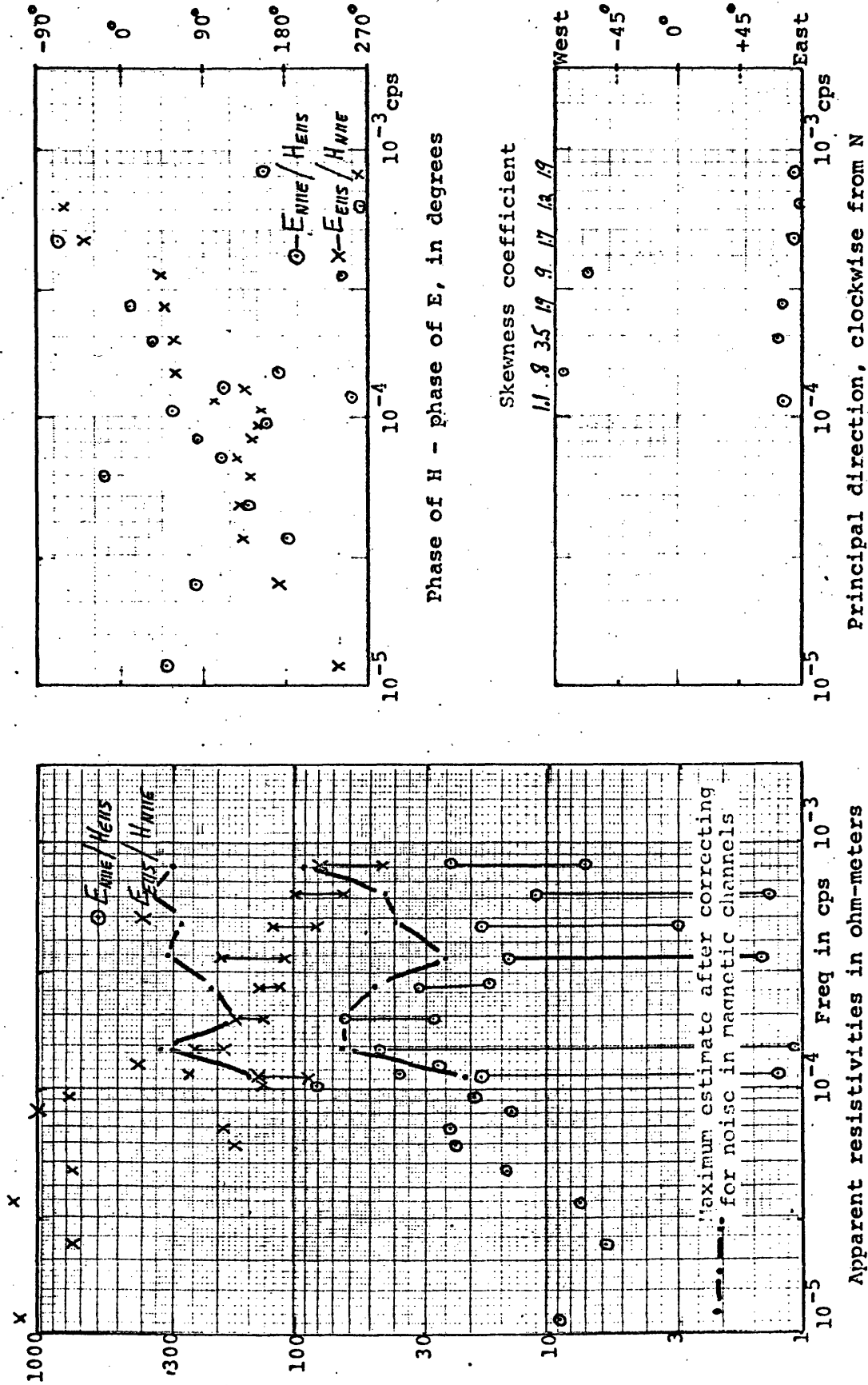


Figure 3.26 Magnetotelluric apparent resistivities, E-H phases, principal directions, and skewness coefficients for Yuma, Arizona

Gallup, New Mexico

The magnetotelluric data field from Gallup are plotted in Figure 3.27. Observed apparent resistivities, E-H phases, principal directions, and skewness coefficients are shown in Figure 3.28. Low skewness coefficients indicate that the N65°E principal direction can be used for a valid two-dimensional interpretation.

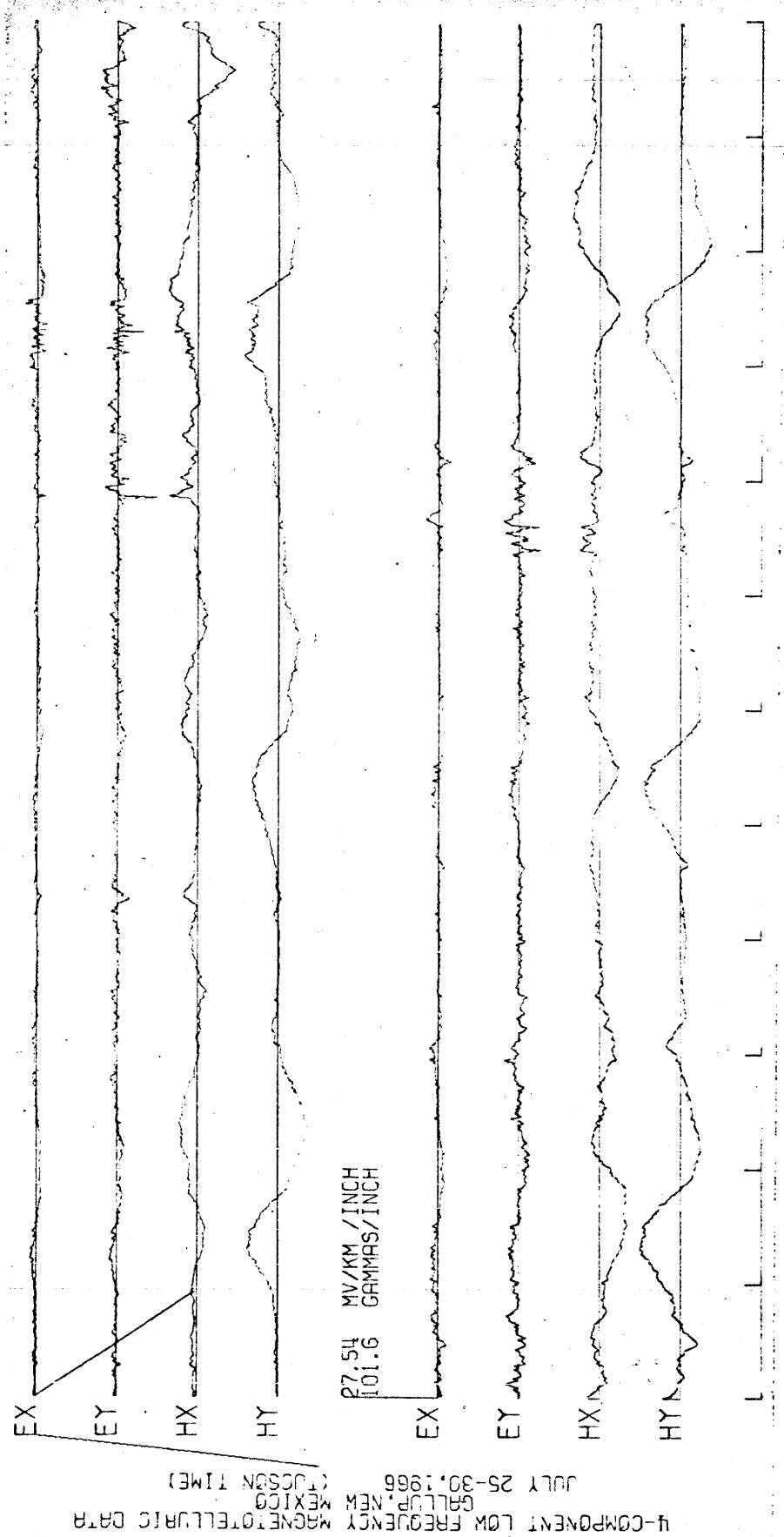


Figure 3.27 Magnetotelluric field data, Gallup, N.M.

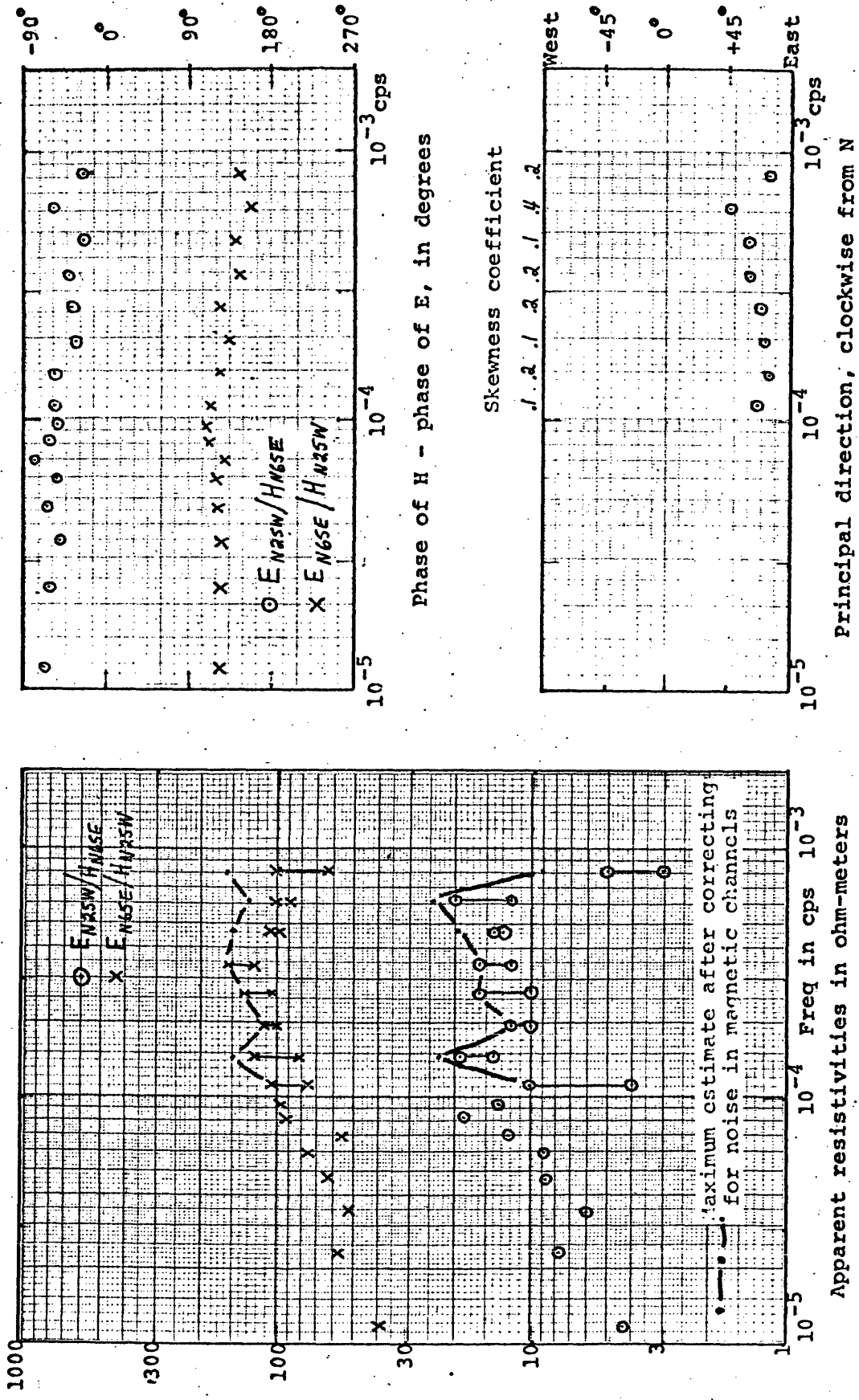


Figure 3.28 Magnetotelluric apparent resistivities, E-H phases, principal directions, and skewness coefficients for Gallup, New Mexico



### 3.5 Interpreted conductivity structure from magnetotelluric apparent resistivities

The most striking characteristic of the results presented in the previous section is that at every site the calculated apparent resistivities are significantly anisotropic. To interpret these results, it is now assumed that this anisotropy is caused by inhomogeneous conductivity structure. For the Tucson and Yuma sites, the skewness coefficients are high and the results from these sites cannot be properly interpreted.

For the other sites, where two-dimensionality is indicated, the different principal directions along the profile suggest that the structural strike of the two-dimensional feature is changing or that different sites are influenced by totally independent structures. It will shortly be shown that, even with associated skin depths of 30 to 600 kms, the apparent resistivity is strongly influenced by relatively small surface conductivity structures.

Many degrees of freedom exist for an interpretation of these results because these stations do not form a true closely-spaced profile over a two-dimensional feature, but

must be considered separately, and because only a limited frequency range is available. The great need for contiguous telluric lines to tie the profile together is very apparent when working with this data. Thus, detailed fits of observed apparent resistivity profiles to theoretical conductivity sections is not as important to the author as obtaining geologically feasible sections.

Measured crustal resistivities and crustal structure information, where available, has been incorporated into the interpretation. The surface sediments in the Southwest are mostly conductive unconsolidated deposits with resistivities of 1-30 ohm-meters (Hopkins and Smith, 1966; Keller, et al, 1966; Plouff, 1966; Vozoff, et al, 1963). As a first approximation to a mantle conductivity profile the Cantwell-McDonald profile of Figure 2.3 was used. This profile combines magnetotelluric results of Cantwell (1960) for values down to 100 km with geomagnetic attenuation results of McDonald (1957) for the mantle.

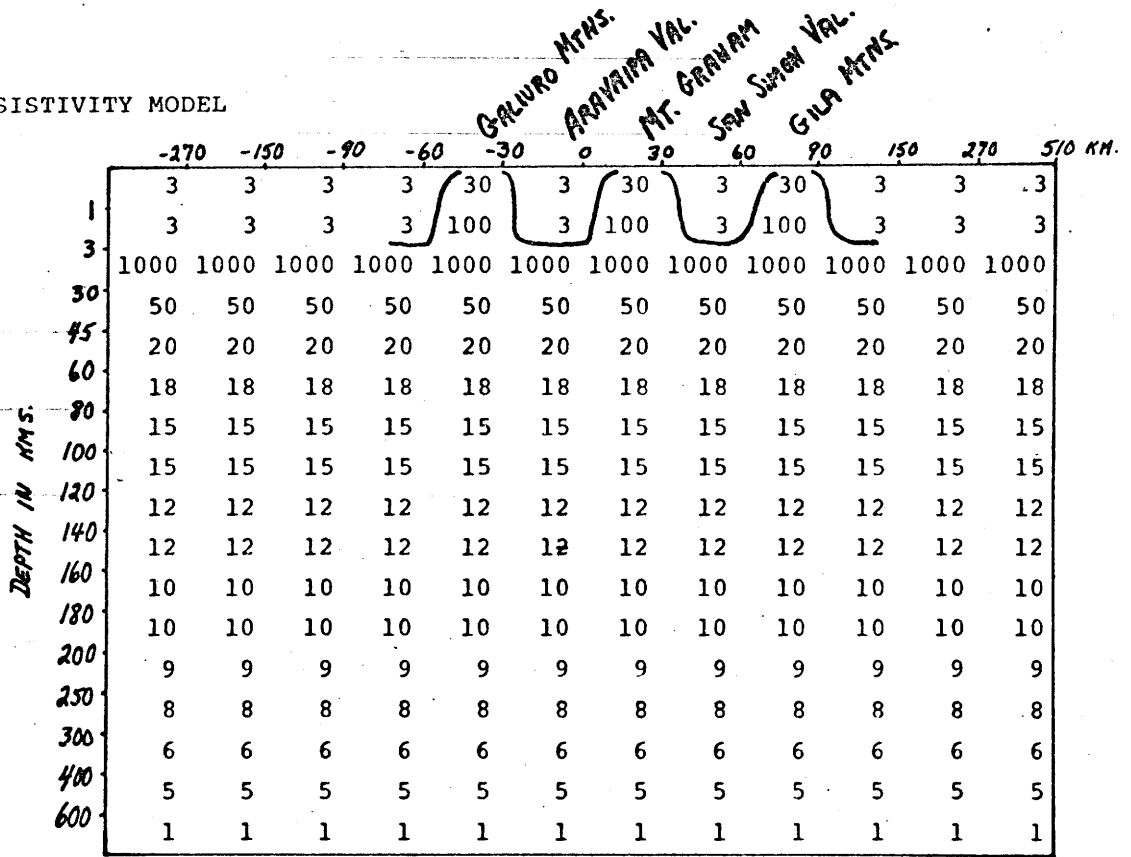
#### Interpretation of Safford results

The results for Safford (Figure 3.16) will be discussed first to indicate the effect of surface conductivity structure. Safford lies in a typical NW trending Basin and

Range graben between two mountain blocks. Crustal thickness 40 miles to the NW is 30 km (Warren, 1967). Resistivities in the Gila Mountains to the NE are about 100 ohm-meters (Vozoff, et al, 1963). Hot saline springs in the valley indicate that the resistivity of the sediments must be quite low.

The principal direction calculated for Safford corresponds to the strike of the Basin and Range structure. However, observed apparent resistivities are much lower than those indicated for a Cantwell-McDonald profile (Table 2.1). Therefore, a more conductive upper mantle is included beneath Basin and Range blocks in the two-dimensional interpretive model of Figure 3.29. The Safford results correspond to theoretical apparent resistivities within the graben. Note that the E perpendicular theoretical apparent resistivities differ drastically over the conductive and the resistive blocks, whereas the E parallel values are very little affected. Because the skin depths for these frequencies are very long, the current density across strike is roughly constant at the surface and little voltage is developed across electrodes within a conductive block. The currents parallel to strike, however, can adjust to flow in conductive zones to yield a continuous E parallel. This

RESISTIVITY MODEL



RESISTIVITIES IN OHM METERS

APPARENT RESISTIVITY CROSS-SECTION

**SAFFORD**

E perpendicular to strike

$10^{-3}$ cps	17	9.8	5.6	607	2.8	414	2.8	600	7.1	15	25
$10^{-4}$	11	6.1	3.3	370	1.5	246	1.5	367	4.3	9.7	18
$10^{-5}$	6.6	3.5	1.9	218	.9	144	.9	217	2.5	5.7	11

E parallel to strike

$10^{-3}$	24	25	27	30	29	31	29	30	26	24	24
$10^{-4}$	19	19	19	19	19	19	19	19	19	19	19
$10^{-5}$	13	13	13	13	13	13	13	13	13	13	13

Interpreted conductivity structure, Safford, Ariz.

Figure 3.29

effect results in the principal direction for Z being along the structural strike in a graben, and against the strike over a horst.

For frequencies with skin depths greater than about 200 km, the Safford valley cannot be considered strictly two-dimensional and possibly the E parallel apparent resistivities at the low frequencies are similarly depressed.

#### Interpretation of Roswell and Deming results

The Roswell and Deming results (Figures 3.9, 3.11 and 3.14) are particularly interesting because a reversal in the sign of  $H_z$  variations was detected between these sites with a line of magnetometer stations (Schmucker, 1964).

This anomaly, the "Texas Anomaly", was then interpreted to reflect a N-S striking step increase in depth to a conductive zone under eastern New Mexico. More recently, this anomaly has been called the Rio Grande anomaly to reflect a decrease in depth to a conductive zone under the Rio Grande depression (Schmucker, 1967) Locations of Schmucker's geomagnetic stations are included in Figure 3.1.

Unfortunately, telephone connections were unavailable in the Rio Grande depression, except for near El Paso where

much commercial electrical noise is introduced, and both the Deming and Roswell anisotropic apparent resistivities are influenced by surface conductivity structure. Thin sediments at Roswell thicken towards the east-southeast, until a total thickness of 5 km are reached in the Delaware Basin (Kinney, 1967). These sediments thin towards the N-S trending Southern Rocky Mountains just west of Roswell. Thus, the Roswell electrode site is on the resistive side of a lateral conductivity contrast, with an associated principal direction perpendicular (E-W) to the structure.

At Deming, the NW principal direction is probably caused by conductivity contrasts in the sediments. Consolidated sediments at the electrode site at Silver City in the foothills of the Pinos Altos and Burro Mountains grade SE downslope into conductive alluvium underlying the Deming to Wilna dipole. This contrast should enhance the Silver City to Deming signal to produce the observed principal direction.

A composite interpreted conductivity structure which yields theoretical values comparable to the observed apparent resistivities is shown in Figure 3.30. This cross-section includes crustal thickness information from



Stewart and Pakiser (1962) and Pakiser and Steinhart (1964), a slightly modified Cantwell-McDonald conductivity profile under Roswell, a postulated "Rio Grande conductive zone" with a conductivity profile similar to that interpreted for Safford, and an intermediate profile under Deming. Needless to say, this profile does not include enough control points, includes a Deming structure which has been rotated  $45^{\circ}$  to get into the roughly E-W cross-section, and should be taken as diagrammatic.

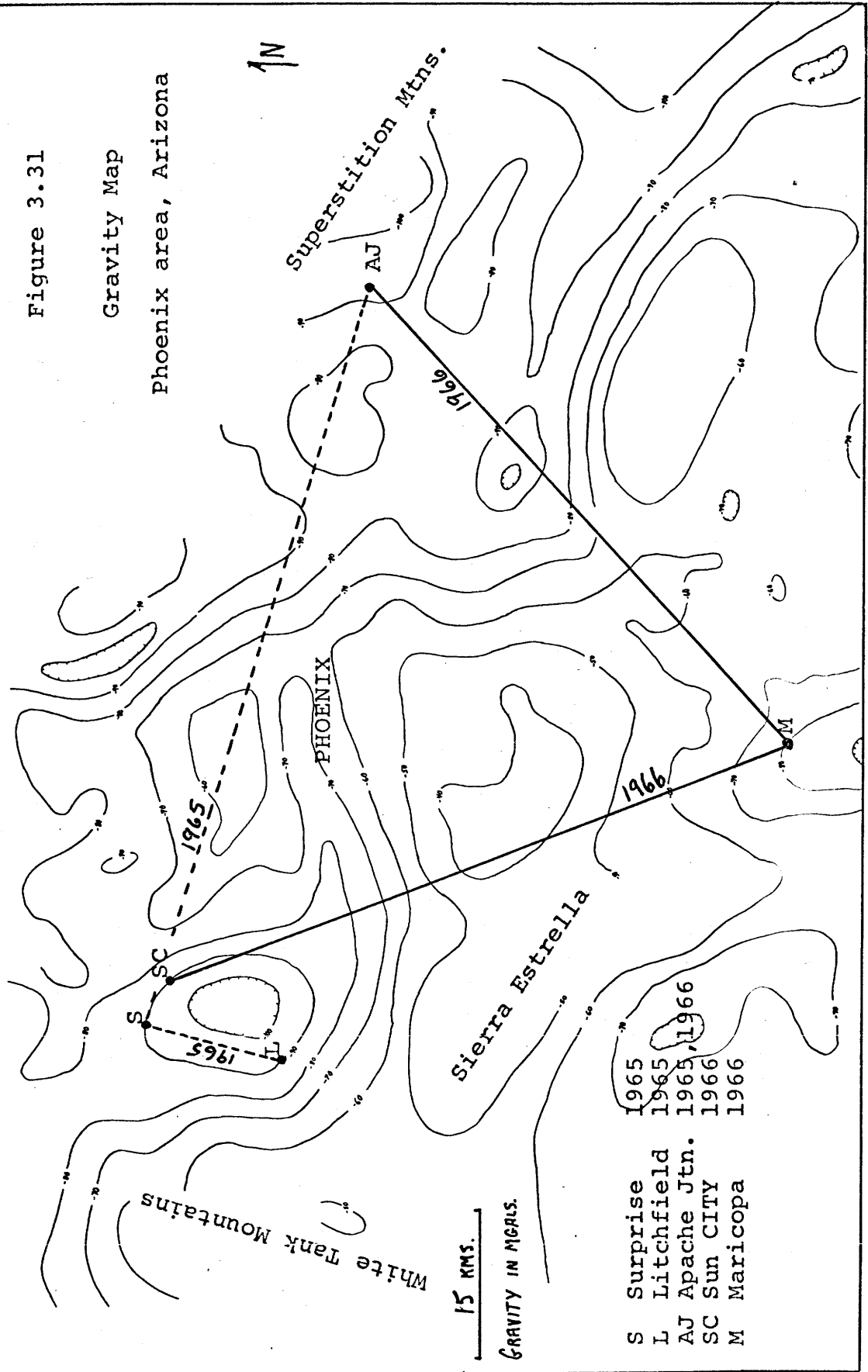
#### Interpretation of Phoenix results

The results from Phoenix also exhibit the effects of surface conductivity structures. The principal direction of  $N60^{\circ}W$  for the 1965 site is accompanied by very low apparent resistivities for the  $N30^{\circ}E$  direction (Figure 3.22). For the 1966 sites, the principal direction is  $N30^{\circ}W$  and the anisotropy is not quite so pronounced (Figure 3.23).

Analogously to the way a conductive graben affected the Safford apparent resistivities, smaller basins of conductive alluvium in the Phoenix area can electrically short out dipoles spread across these basins. Figure 3.31 shows the electrode sites on a gravity map of the Phoenix



Figure 3.31  
Gravity Map  
Phoenix area, Arizona



area (Peterson, 1965). The gravity map is characterized by isolated minima indicative of increased thicknesses of low density alluvium superimposed on a regional gradient decreasing to the NE.

Note that a 1965 dipole spans the pronounced gravity low WNW of Phoenix. Because little voltage is measured on this dipole, the calculated principal direction of  $N60^{\circ}W$  corresponds to a direction perpendicular to this low voltage line. Similarly, the 1966 dipole from Maricopa to Apache Junction crosses another deep valley of conductive alluvium. The other long dipole from Sun City to Maricopa averages over a more heterogeneous conductivity structure, and the resultant apparent resistivity profile is interpreted to more accurately reflect the upper mantle conductivity structure. Note that this apparent resistivity profile is comparable to the E parallel value from Deming.

#### Interpretation of Gallup results

Again, insufficient control exists to limit the possible two-dimensional models necessary to explain the anisotropic apparent resistivity results for Gallup (Figure 3.28). However, the known variations in thickness

of the surface sediments appear to account for the anisotropy. As indicated on a map of the elevation of the basement surface (Kinney, 1967; reproduced in Figure 3.32), sediments at Gallup thicken markedly NE towards the San Juan Basin while basement rock is exposed in the Chuska Mountains to the west and in the Zuni uplift to the south.

The observed principal direction of  $N70^{\circ}E$  is approximately perpendicular to a gross strike of exposed basement near the array (see Figure 3.32). Current flowing perpendicular to this principal direction sees a trough of sediments between two resistive blocks. Therefore, the situation at Gallup is rather unusual. Three-dimensional conductivity structure is indicated, but two different two-dimensional geometries must be used to model the conductivity structure. From Figure 3.29 we see that for current flowing along a trough (E parallel polarization in Figure 3.29) the apparent resistivities are not sensitive to the boundaries of the trough. Therefore, an E perpendicular apparent resistivity calculation for two-dimensional variations along the trough can be used as a model for the  $N70^{\circ}E$  apparent resistivity at Gallup. The current flowing in a  $N20^{\circ}W$  direction crosses a trough

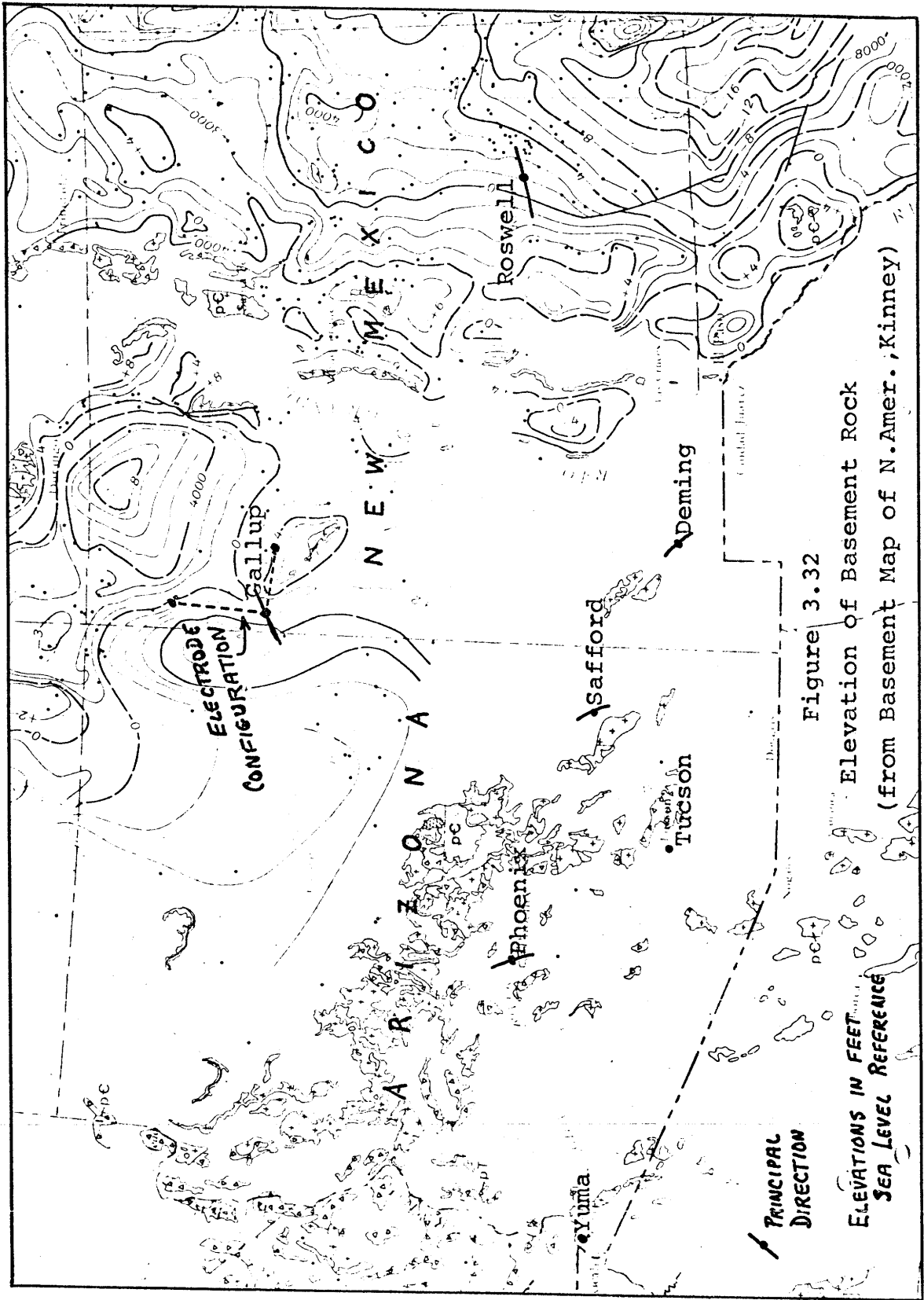


Figure 3.32

Elevation of Basement Rock  
(from Basement Map of N.Amer., Kinney)

superimposed on a wedge of sediments thickening to the northeast. For currents along the strike of a wedge, theoretical apparent resistivities approximate the appropriate one-dimensional case. Therefore, an E perpendicular calculation within a trough can model the N20°W apparent resistivity at Gallup.

Thus, the N70°E values, representative of values for the resistive side of a lateral contrast for the E perpendicular case, are enhanced. Whereas the N20°W values, being representative for E perpendicular values within a conductive trough, are depressed. An intermediate profile is therefore suggested for the one-dimensional upper mantle conductivity profile to use in the models. An upper mantle conductivity profile similar to that from Deming, a crustal thickness of 40 km (Warren, 1967; Roller, 1965), and a Colorado Plateau sediment resistivity of 10 ohm-meters (Keller, et al, 1966) are incorporated into the two resistivity models for Gallup shown in Figure 3.33. These models yield theoretical apparent resistivities comparable to the observed values of Figure 3.28.

#### Discussion of the Yuma and Tucson results

The observed results for both Yuma (Figure 3.26 and Tucson (Figure 3.19) are characterized by large skewness

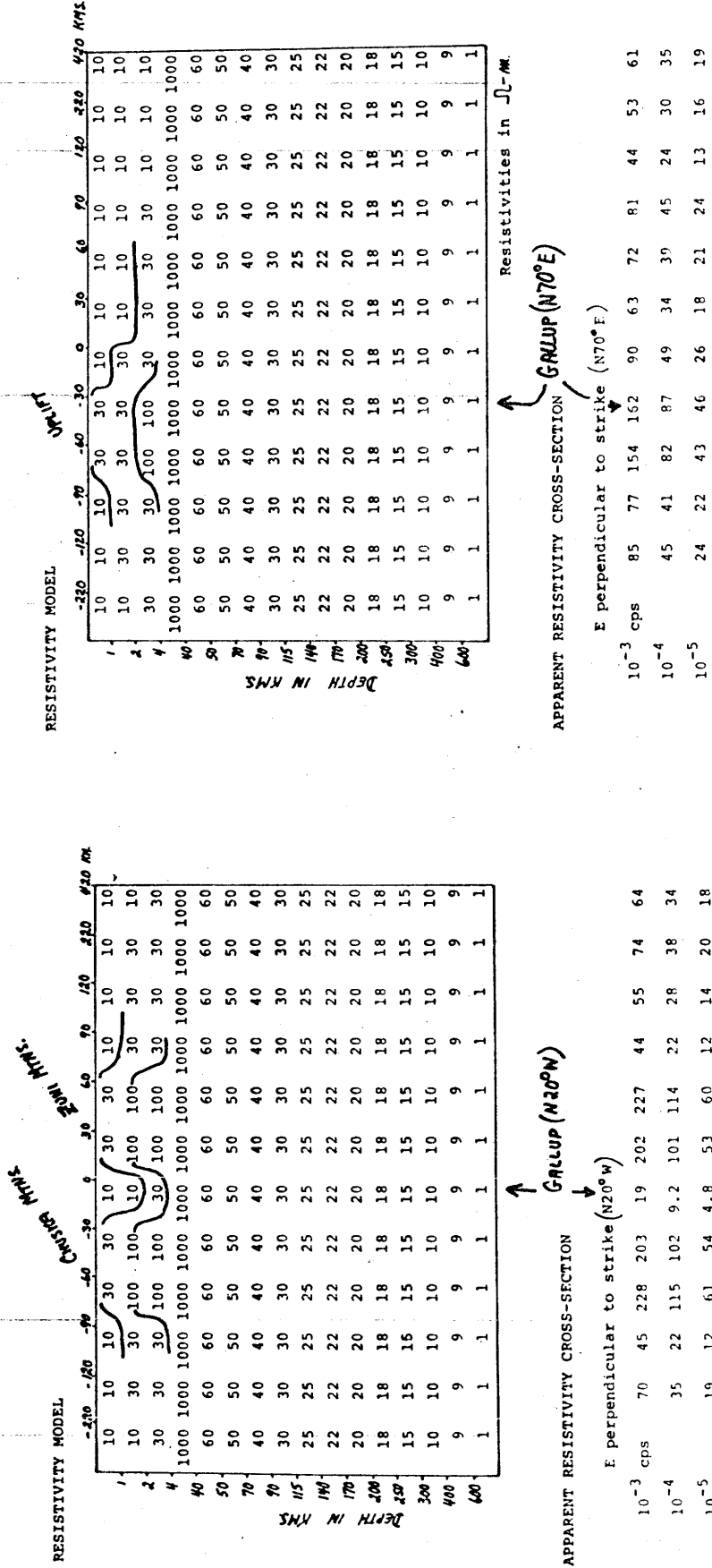


Figure 3.33 Interpreted conductivity structure, Gallup, N.M.

coefficients, widely scattered phases, and increasing apparent resistivities at the low frequencies. Possibly the electric field polarization ellipse is rotated and/or distorted by three-dimensional conductivity structure, such that the high Cagniard apparent resistivity values at these frequencies correspond to a weak H component.

Because the tensor cannot be properly measured with the lack of statistics at these frequencies, other estimates must be made. The following parameter is always less than the greater principal value apparent resistivity:

$$\rho_a^* = \frac{0.2}{f} \frac{|E_{total}|^2}{|H_{total}|^2} \quad 3.5-1$$

Even using this formula, the apparent resistivities for the diurnal frequency and the two higher harmonics remain anomalous:

<u>Period</u>	<u>Frequency</u>	$\rho_a^*$ Yuma	$\rho_a^*$ Tucson
24 hours	$0.116 \times 10^{-4}$ cps	220 $\Omega\text{-m}$	82 $\Omega\text{-m}$
12	$0.231 \times 10^{-4}$	240	39
8	$0.347 \times 10^{-4}$	320	24

The complex structure at Yuma includes the Salton Sea trough to the west, with 6 km (Biehler, et al, 1964) of very conductive sediments, and a crustal thickness between

30 km as measured under the Imperial Valley to the west (Biehler, et al, 1964) and 20 km as measured at Gila Bend 150 km to the northeast (Warren, 1967). Possibly a normal upper mantle conductivity profile exists under Yuma and southern California. The contacts with conductive zones in the upper mantle to the west under the Pacific Ocean (Filloux, 1966) and to the east at Phoenix, Safford, and Deming, cause an enhancement of voltage. Slightly anomalous magnetics have been observed near Yuma (Schmucker, 1964).

Two-dimensional models incorporating the above conductivity structure, however, do not yield theoretical apparent resistivities which increase with decreasing frequency at the diurnal frequency. To obtain such behavior, two-dimensional conductivity models are required with upper mantle conductivities which are petrologically too resistive. At this stage, with our limited areal coverage of electrical measurements and our lack of understanding of the effects of three-dimensional features, we are unable to interpret the Yuma data.

The electrical conductivity structure at Tucson was first noted as anomalous by Bartels (1939), who attributed small  $H_z$  variations to a relatively conductive zone



beneath Tucson. The  $H_z$  variations at Tucson were interpreted as low, however, only in relation to those observed at Watheroo, Australia, a coastal observatory at an equivalent geomagnetic latitude to Tucson. The following table shows the  $H_{\text{vertical}}/H_{\text{horizontal}}$  ratio for the fifteen minute to two hour disturbance field (Bartels, 1939) and the quiet day diurnal (Vestine, 1960) for Tucson and other stations.

<u>Station</u>	<u>Geomag. lat.</u>	<u><math>H_z/H_h</math> (Disturbed)</u>	<u><math>H_z/H_h</math> (Sq)</u>
Sitka	60°	.53	.30
Cheltenham	50°	.38	.22
Tucson	40°	.10	.34
San Juan	30°	.15	.27
Honolulu	21°	.24	.52
Huancayo	-1°	.10	.09
Watheroo	-42°	.57	.83

Table 3.2 Representative  $H_{\text{vertical}}/H_{\text{horizontal}}$  Ratios

As shown in this table, Huancayo is characterized by low  $H_z/H_h$  ratios, due to the presence of the equatorial electrojet which produces a large  $H_h$ . Watheroo is characterized by large ratios, probably associated with a coast effect.

The low ratio for Tucson at the disturbed field frequencies is comparable to the value of 0.07 for a one

hour period measured by Schmucker (1964). Moreover, a low value of this ratio characterizes much of western North America (Schmucker, 1964; Caner and Cannon, 1965).

The diurnal  $H_z/H_h$  ratio for Tucson, however, appears comparable to those from the other observatories. The expected ratio over a one-dimensional conductivity profile can be obtained from equation 2.4-11:

$$\frac{H_z}{H_y} = \frac{-\partial E_x / \partial y}{\partial E_z / \partial z} = \frac{-k_y}{k_z} = \frac{-2\pi/\lambda}{\sqrt{-i\mu\omega\sigma_a}} \quad 3.5-2$$

For a diurnal wavelength equal to the circumference of the earth, and assuming  $\rho_a = 30$  ohm-meters, the computed ratio is 0.1. Doubling this value to account for a  $H_z$  corresponding to the latitudinal variation results in an expected ratio of about 0.20. The difference between this value and that in Table 3.2 suggests a contribution from lateral conductivity contrasts at depth.

Cagniard apparent resistivities of 100-200 ohm-meters for Tucson calculated from telluric and magnetic diurnal variation data of Fleming (1939) are consistent with the high diurnal value measured in this investigation (Figure 3.19). These high apparent resistivities, however, are inconsistent with the simple horizontally stratified

structure of high conductivity originally envisaged by Bartels (1939). The complex geology and crustal structure at Tucson suggests that the high skewness coefficients are due to a true three-dimensional conductivity structure and not to a distortion introduced into the data as is the case at Yuma.

Tucson has been found from other geophysical evidence to be different than the rest of the Southwest. Normal heat flow (Sclater, 1967), a high  $P_n$  velocity (Herrin and Taggart, 1962), and small seismic travel-time residuals (Hales and Doyle, 1967) observed in this area would be consistent with a localized zone of normal resistive mantle under southeastern Arizona within the anomalous high conductivity zone. Nevertheless, as is the case at Yuma, we are unable to properly interpret this data.

#### Summary of interpretation

The major limitation to the interpretation, due to the restricted availability of electrode sites, is in the lack of continuous magnetotelluric coverage. The anisotropy of the measured apparent resistivities is primarily due to surface conductivity inhomogeneities. Particularly for isolated stations, the gross deep structure cannot be

uniquely determined. Nevertheless, by "correcting" for the various superficial features, an areal pattern appears that suggests an anomalously conductive upper mantle beneath southern Arizona and New Mexico.

The conductivity profiles interpreted from the magnetotelluric results are classified as

"continental" for Roswell

"intermediate" for Phoenix, Gallup, Deming

"conductive" for Safford

and are plotted in Figure 3.34 along with the Cantwell-McDonald profile. Note that the maximum conductivity differentials are at 60 km depth, that the "intermediate" curve merges with the "continental" at a depth of 200 km, and that the "conductive" profile is more conductive to 600 km.

Because the observed apparent resistivities are markedly influenced by surface conductivity inhomogeneities, one might question the sensitivity of the interpretation to differentiate between the profiles shown in Figure 3.34.

"E parallel" apparent resistivities are not so influenced by the surface structure, however, and good examples were available for the Roswell, Deming and Safford sites.

The "continental" profile is self-consistent petrologically because it corresponds to the theoretical

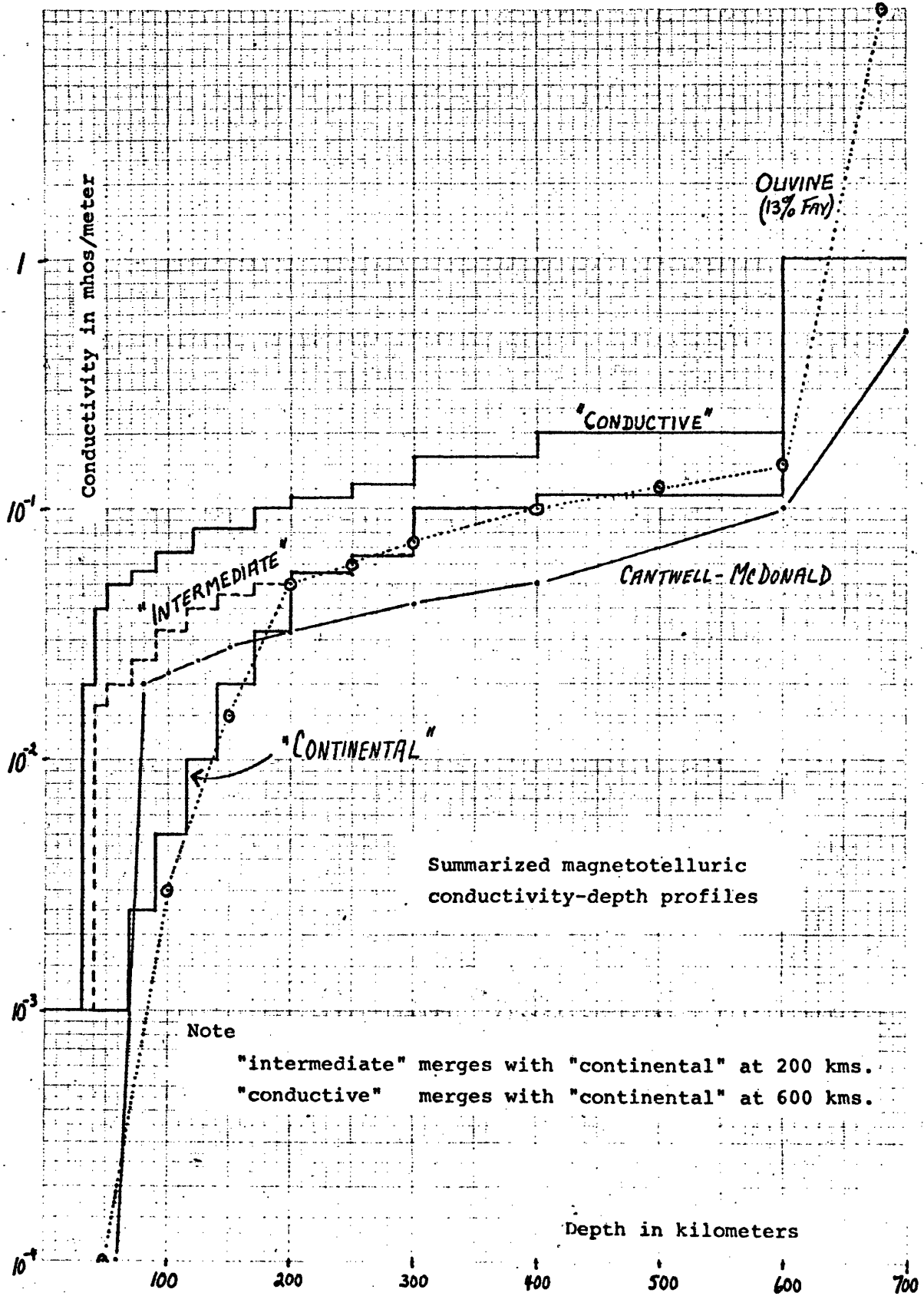
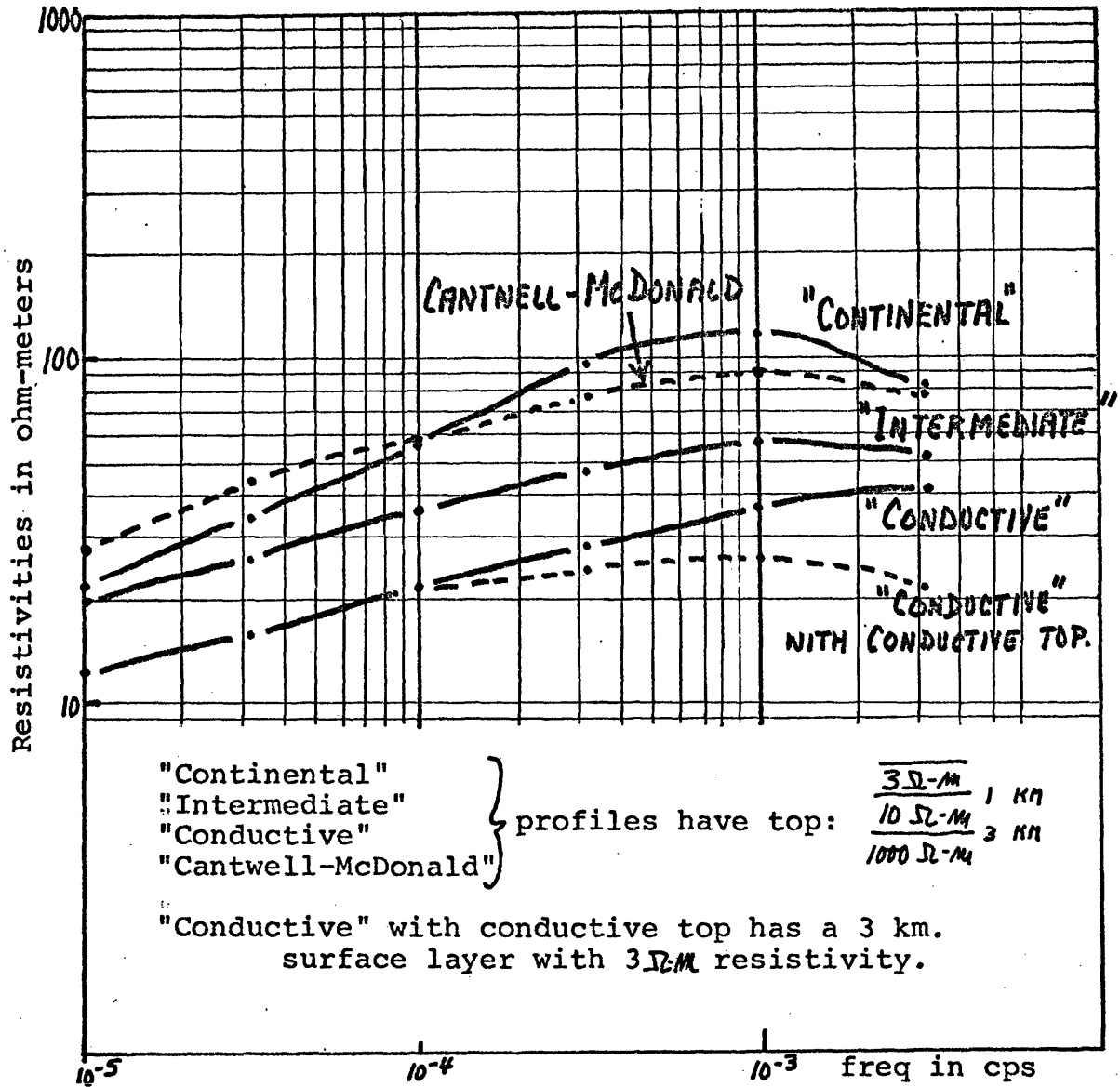


Figure 3.34

conductivity profile for an upper mantle of olivine (13% fayalite) for a typical continental geotherm (Ringwood, 1966). This conductivity profile is also included in Figure 3.34 and is discussed more fully in the next section. Note that for a typical continental conductivity profile the Cantwell-McDonald model appears too conductive above 200 km, too resistive below.

The theoretical apparent resistivity curves corresponding to a layered media with these conductivity profiles are exhibited in Figure 3.35. The frustrations of matching measured apparent resistivities over a limited frequency range to theoretical conductivity profiles is evident by observing how the significantly different olivine and Cantwell-McDonald profiles of Figure 3.34 yield apparent resistivity curves in Figure 3.35 which are similar within the limits of experimental error.



Theoretical apparent resistivity curves  
for summarized conductivity profiles.

Figure 3.35

## Chapter 4 - Interpretation of the Electrical Conductivity Anomaly

In this chapter, the electrical conductivity anomaly in the upper mantle, which has been inferred from the magnetotelluric data, is interpreted to be due to increased temperatures. In Section 4.1, information about electrical conductivity of upper mantle constituents is combined with the magnetotelluric conductivity versus depth profiles to obtain geotherms to define this anomalous zone of high temperature. In Section 4.2, this anomalous zone is correlated with other geological and geophysical data from the southwestern United States.

### 4.1 Electrical conductivity of the upper mantle

Regions of anomalous electrical conductivity must reflect regions of different composition, phase, pressure, or temperature. To force the interpretation to be acceptable petrologically, a realistic compositional model for the mantle will be assumed. Present ideas concerning the composition of the upper mantle and the associated problems of the nature of the Moho have been summarized by Clark and Ringwood (1964), Pakiser (1965)



and Ringwood (1966). The following interpretation incorporates Ringwood's "pyrolite" petrological model which satisfies seismic, density, and chemical restrictions.

Pyrolite has a chemical composition equivalent to a mixture of 75% peridotite (80% olivine ( $(\text{Mg, Fe})_2\text{SiO}_4$ ), 20% enstatite ( $\text{MgSiO}_3$ )) and 25% basalt and yields basaltic magma upon partial fusion. Figure 4.1 shows the P-T stability fields of the following pyrolite mineral assemblages:

1) Plagioclase pyrolite:

olivine + Al-poor pyroxenes + plagioclase

2) Pyroxene pyrolite:

olivine + Al-rich pyroxenes + spinel

3) Garnet pyrolite:

olivine + Al-poor pyroxenes + garnet

The pyroxene pyrolite essentially represents a transition zone between peridotite plus basalt and peridotite plus eclogite. This transition depends critically on the chemical potential of Al and requires higher pressure than for the basalt-eclogite transition (Yoder and Tilley, 1962). The phase diagram incorporates the pyrolite solidus as inferred by Ringwood (1966) and by McConnell, et al (1967). This solidus represents the beginning of

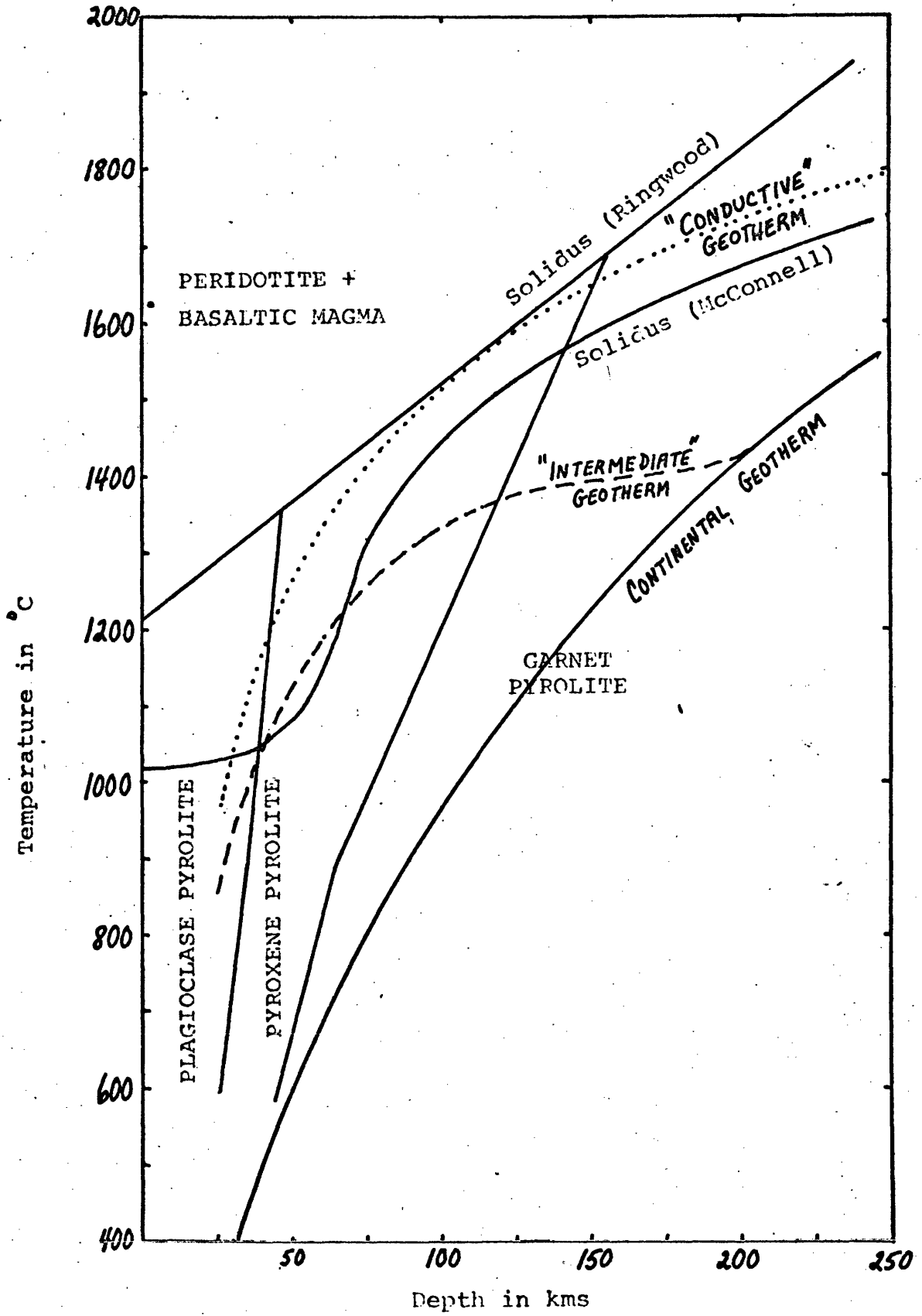


Figure 4.1 Pyrolite Stability Fields  
(after Ringwood, 1966)

melting of the basaltic fraction, not the melting of the entire rock.

In the pyrolite model, the Moho represents a chemical discontinuity between a crust of vertically separated volatile components and a more barren layer of peridotite. This barren layer is thought to contain segregations of eclogite. Beneath this barren layer, the occurrence of the various mineral assemblages in the mantle is determined by the intersection of geotherms with the stability fields of the assemblages.

Having specified a compositional model, the electrical conductivity of pyrolite must now be determined. However, there exist no laboratory measurements on the electrical conductivity of the various pyrolite assemblages. Therefore, the electrical conductivity of the upper mantle must be approached through the constituent minerals. In Figure 4.2, plots of conductivity versus temperature are shown for many mantle constituents.

The electrical conductivity of these silicates reflects a semi-conduction temperature dependence expressed as

$$\sigma = \sigma_0 e^{-E/kT}$$
, where E is the activation energy required to excite either: 1) an electron to a mobile state via impurity levels for extrinsic semi-conduction; or, 2)

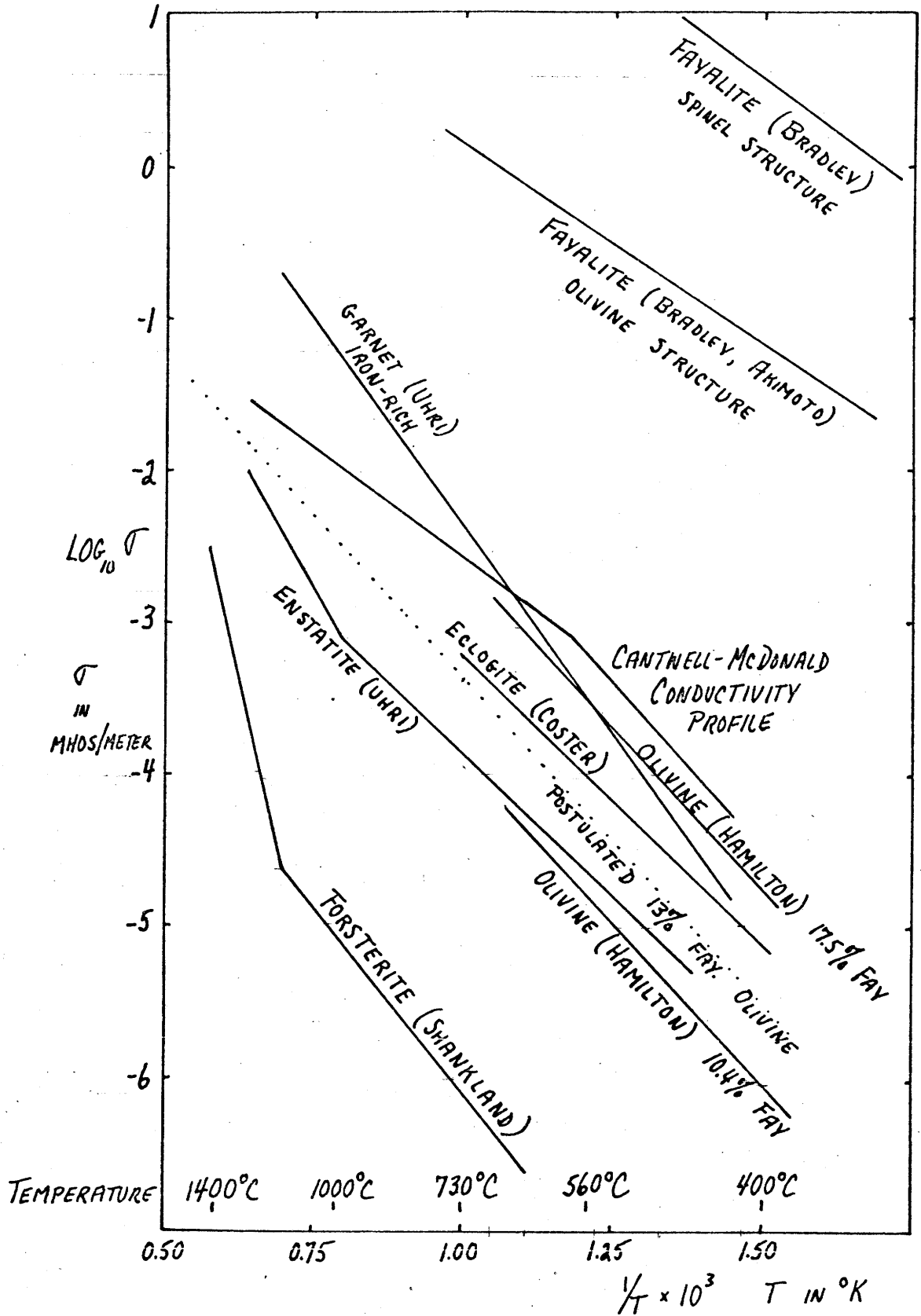


Figure 4.2 Conductivity-temperature plots for mantle constituents

an electron to a mobile state through the energy gap between the valence band and the conduction band for intrinsic electronic semi-conduction; or 3) an ion to a mobile state through the creation of defects for intrinsic ionic conduction. The smaller pressure dependence of the conductivity is usually described as the effect of pressure on this activation energy.

After much work on the conductivity of many different silicates over a wide range of temperatures, the specific conduction mechanisms are still not definitely known. Hughes (1955) found an increase in the activation energy with pressure for peridot at temperatures greater than  $1100^{\circ}\text{C}$ , an effect consistent with an ionic conduction mechanism. Bradley, et al, (1962) detected a decrease in the activation energy with pressure for olivines at temperatures below  $770^{\circ}\text{C}$ , however, and hypothesized a charge transfer process between  $\text{Fe}^{+2}$  and  $\text{Fe}^{+3}$ , in which electron mobility is increased by wave function overlap at higher pressures. Hamilton (1965) also detected a decrease in the activation energy with pressure for olivine, but could not specify a conduction mechanism. Recently, Shankland (1966) obtained relatively low conductivities for a single synthetic forsterite crystal and introduced the question of

the effect of grain boundaries on the mobility.

Very important for our problem is the marked increase in the electrical conductivity of olivine with increasing iron content. Because a pyrolite upper mantle is mostly olivine, these conductivity curves for olivine are particularly significant. It is evident that conductivity differences in pyrolite could be attributed to variations either in temperature or in the iron content of the olivine. Temperature variations are more likely for an anomalous conductivity zone associated with high heat flow. From chemical considerations, moreover, the olivine of the mantle is interpreted to have a uniform iron content of 12 - 15% (Ringwood, 1966b). Thus as a first approximation, a 13% iron content will be assumed for the olivine of the upper mantle, and the interpolated conductivity curve for this olivine is presented in Figure 4.2.

The conductivity for the pyrope garnet specified for pyrolite is probably much less than that for the iron-rich garnet included in Figure 4.2, and is probably less than that for a 13% fayalite olivine. The conductivity of enstatite is less than that for 13% fayalite olivine. The conductivity of eclogite is shown as being close to that for 13% fayalite olivine; the conductivity of basalt is

comparable to that for eclogite (Coster, 1948). Because the major component of pyrolite is as conductive as the minor components, the conductivity curve for 13% fayalite olivine can be taken as representative for pyrolite. Note that the Cantwell-McDonald conductivity profile (plotted on Figure 4.2 assuming a typical continental geotherm (Ringwood, 1966)) appears to be too conductive at the low-temperature (near surface) end.

Upper mantle temperature distribution from the electrical conductivity structure

To obtain geotherms corresponding to the earth conductivity profiles obtained in the last chapter, the conductivity curve for 13% fayalite olivine has to be extrapolated beyond the experimentally derived curves of Figure 4.2. A straight-line extrapolation assumes a constant conduction mechanism to very high temperatures. This assumption is not strictly consistent with Shankland's results of Figure 4.2. Also, at higher P-T conditions the phase transition from an olivine structure to the closer packed spinel structure is accompanied by a 100X increase in conductivity (Bradley, et al, 1962; Akimoto and Fujisawa, 1965). This phase transition should occur at

about 600-700 km, and probably accounts for the observed steep gradients in electrical conductivity and seismic velocity. With a 100X conductivity increase at about 700 km, the resulting conductivity profile for olivine for a continental geotherm is roughly consistent with McDonald's (1957) mantle conductivity profile down to 1000 km. This correspondence does not necessarily indicate the existence of a single conduction mechanism and a homogeneous iron content for the olivine of the mantle, because the combination of a decreasing activation energy and a decreasing iron content could also produce a conductivity curve for the mantle that overlies that for 13% Fe olivine.

Using the relationship from Figure 4.2 for temperature as a function of conductivity (for 13% fayalite olivine) and the summarized anomalous magnetotelluric conductivity versus depth profiles of Figure 3.34, geotherms corresponding to "continental" (Roswell), "intermediate" (Phoenix, Gallup, Deming), and "conductive" (Safford) profiles can be calculated and are plotted on the pyrolite stability field of Figure 4.1. The self-consistency of the models chosen in this interpretation is evidenced by the fact that the Roswell geotherm, corresponding to what



is interpreted to be a normal earth resistivity profile is identical to the "continental geotherm" of Ringwood (1966). Obtaining a geotherm in this fashion was first done by Tozer (1959), who used mantle conductivity estimates of Lahiri and Price (1939) and McDonald (1957) for a full mantle geotherm. Although this technique is imprecise at great depths, the precision of temperature determination from the electrical conductivity is highest in the upper mantle where the conductivity has a strong dependence on temperature.

The indicated maximum temperature deviation of the "intermediate" geotherm over the normal geotherm is about  $500^{\circ}$  at a depth of about 50 km. The "conductive" geotherm is characterized by a maximum temperature deviation of about  $650^{\circ}$  at a depth of 50 km. Both of these geotherms intersect the solidus of McConnell, et al (1967), but not the solidus of Ringwood (1966).

Although no modern measurements on the conductivity of molten basalt exist, Barus and Iddings (1892) observed only a slight reduction in the resistance between two electrodes immersed in basalt as the basalt melted. Since the conductivity of basalt is comparable to that for olivine (13% fayalite), a zone of molten basalt would not severely

effect the bulk electrical conductivity. The interconnection of the liquid basalt fraction in a solid peridotite matrix, however, would markedly increase the thermal conductivity.

Note that in this model there is no evidence for a correlation between the seismic low velocity zone and a possible high conductivity zone (Fournier, 1963).

Although limited control again restricts the interpretation, these geotherms can be plotted on a cross-section for a highly speculative temperature distribution (Figure 4.3). Also included in this temperature cross-section are the appropriate pyrolite assemblages indicated from Figure 4.1. Other geophysical evidence is examined in the next section for independent checks on this interpreted temperature distribution. Altering the interpreted conductivity-temperature curve for pyrolite, however, will only distort the isotherms of the anomalous temperature zone. An upper mantle model more conductive than 13% fayalite olivine would yield lower temperatures, whereas a less conductive upper mantle model would yield higher temperatures. An anomalous zone of increased iron content would not be consistent with other geophysical evidence.

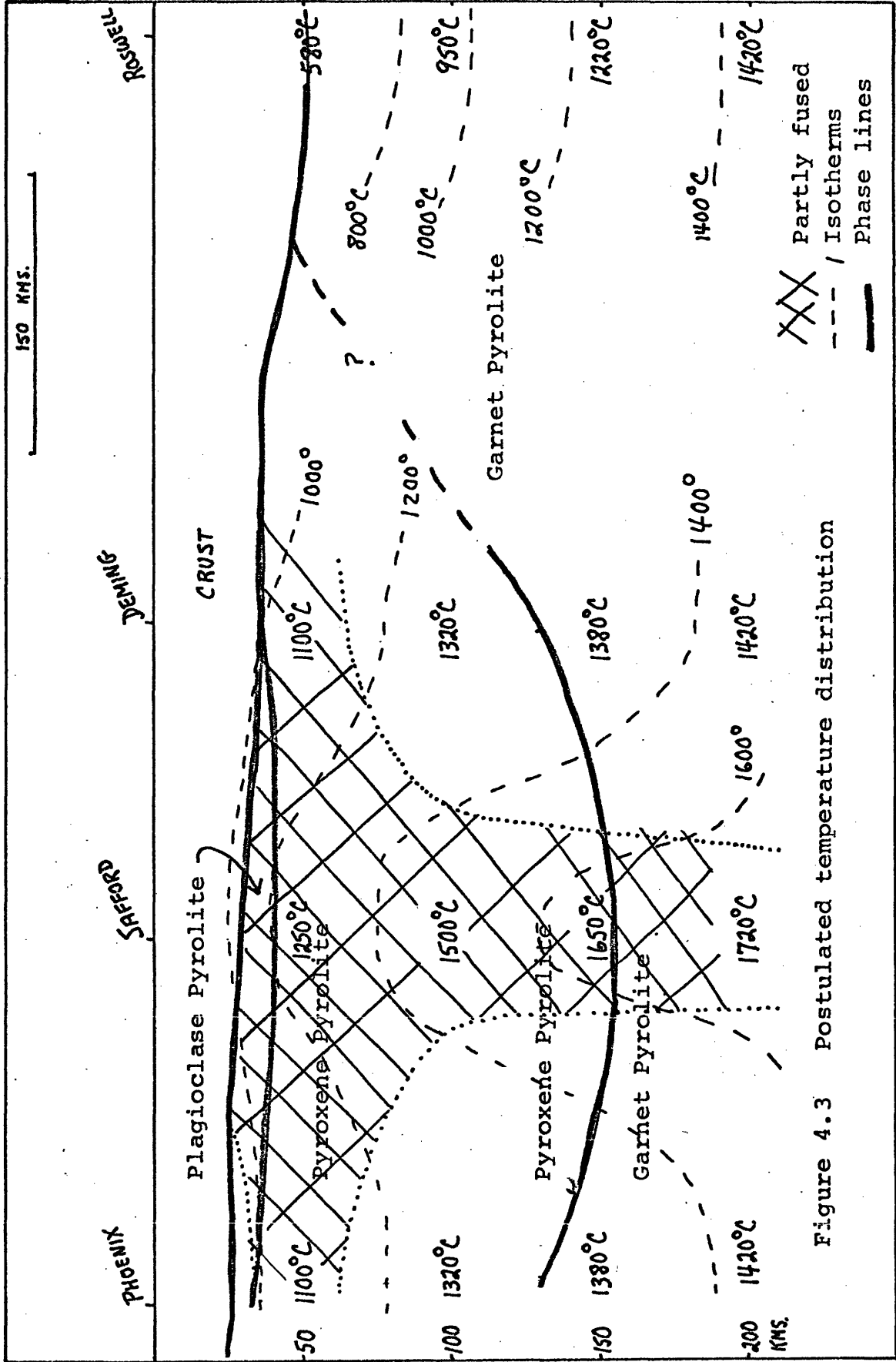


Figure 4.3 Postulated temperature distribution

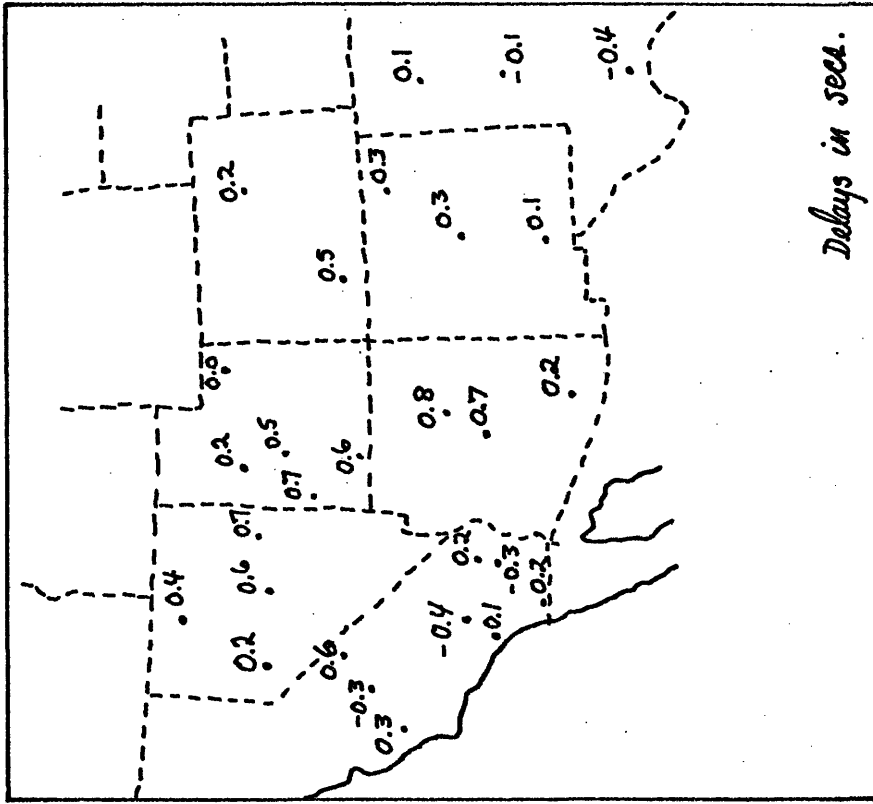
Note that for the anomalous zone the lower crust and upper mantle are above the Curie temperature for magnetite ( $578^{\circ}\text{C}$ ). Such high temperatures have been used in an interpretation by Pakiser and Zietz (1965) to explain the absence of broad magnetic anomalies in the western United States.

#### 4.2 Correlation of the high temperature zone with other geophysical data

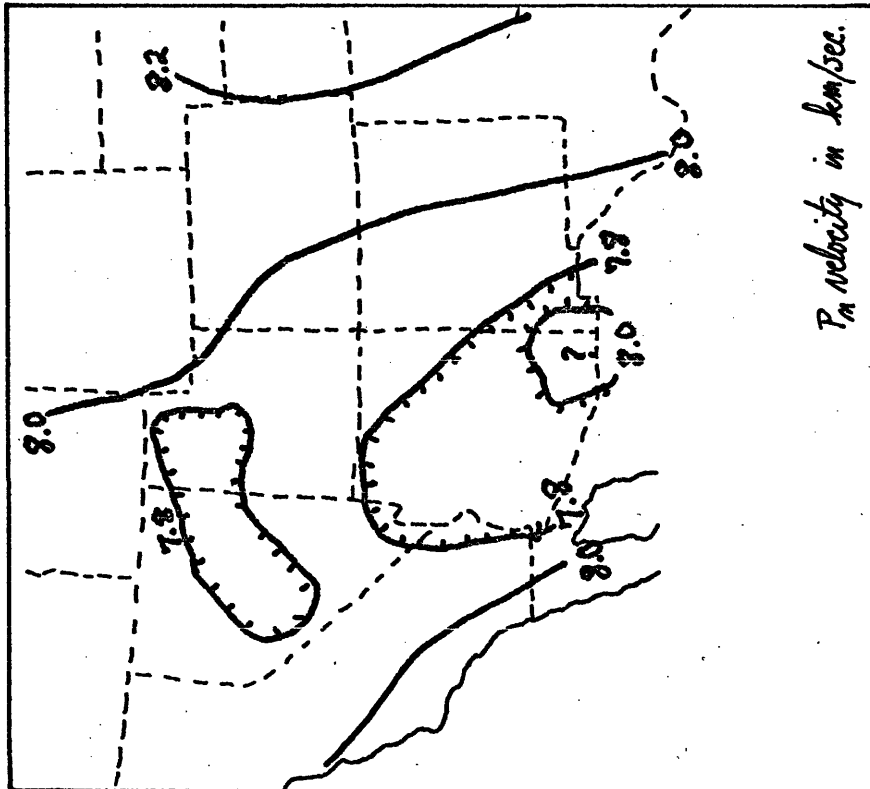
The magnetotelluric data support Schmucker's initial interpretation (1964) of a high conductivity zone in the southwestern United States. The interpretation of a conductive upper mantle due to increased temperatures is consistent with that postulated for western Canada (Caner and Cannon, 1965; Lambert and Caner, 1965). An attempt will now be made to roughly, but quantitatively, correlate this high temperature zone (a  $600^{\circ}\text{C}$  temperature differential at 50 km) with other geophysical data for the western United States.

##### Seismic evidence

Summary maps of  $P_n$  velocity below the Moho and P wave travel time residuals are presented in Figure 4.4 for the western United States. Note that the zone of high electrical conductivity corresponds to zones of low upper mantle velocities and large travel-time residuals. Hales and Doyle (1967) interpret late P and S wave arrivals to a varying shear modulus and conclude that if this is due to increased temperature one mantle component must approach melting. Abnormal S-wave attenuation has been observed for



P-wave travel time residuals  
from Hales and Doyle, 1967



$P_n$  velocity distribution  
from Herrin and Taggart, 1962  
Pakiser and Steinhart, 1964

Figure 4.4 Seismic evidence for an inhomogeneous upper mantle, Western United States

Basin and Range ray-paths (Smith, 1967).

From Figure 4.4, the  $P_n$  velocity differential is  $\Delta N_p = 8.2 \rightarrow 7.8 = -0.4$  km/sec within the anomalous region. To determine whether a temperature differential of  $600^\circ$  at a depth of 50 km is consistent with such a velocity change, the  $\left(\frac{\partial N_p}{\partial T}\right)_P$  coefficient is required. Note that if the comparison is for equal depths, the pressure term can be essentially ignored. It is difficult, however, to determine the effect of temperature on the velocity.

Because the empirical relationship (Birch, 1964)

$$\frac{\partial \rho}{\partial N_p} \approx 0.328$$

4.2-1

is more reliable than the  $\left(\frac{\partial N_p}{\partial T}\right)_P$  coefficient, we can work with the associated density differential.

For  $\Delta N_p = 0.4$  km/sec, the related  $\Delta \rho$  is computed as  $-0.13$  g/cc. This low density corresponds to the  $\Delta \rho = -0.15$  g/cc given by Pakiser and Zietz (1965) to explain the gravity data.

A change in temperature is accompanied by a change in density, as

$$\frac{\Delta \rho}{\rho} = \frac{1}{\rho} \left(\frac{\partial \rho}{\partial T}\right)_P \Delta T$$

4.2-2

where  $\left(\frac{1}{\rho} \frac{\partial \rho}{\partial T}\right)_P$  = vol. coeff. of thermal expansion  
=  $-4.0 \times 10^{-5}/\text{c}^\circ$  for olivine (10% fayalite), Clark (1966)

From 4.2-2 a  $600\text{C}^\circ$  temperature differential can produce a density change, assuming no change of phase, of  $-0.08 \text{ g/cc}$ . From equation 4.2-1, the associated velocity differential is  $-0.25 \text{ km/sec}$ .

These calculated differentials are less than those observed in the anomalous zone, and imply further reductions in the density and velocity from a phase change. From Figure 4.3, a phase change is indicated at a 50 km depth, from garnet pyrolite under Roswell to possibly partially fused pyroxene pyrolite under Safford. From Ringwood (1966), the expected properties of the pyrolite phases are:

	<u>density</u>	<u>P-wave velocity</u>	(at STP)
pyroxene pyrolite	3.33 g/cc	8.18 km/sec	
garnet pyrolite	3.38	8.38	
∴ difference	0.05	0.20	

When the effects of this phase change are added to the calculated reductions in density and velocity due to increased temperature, the observed anomalous velocity and

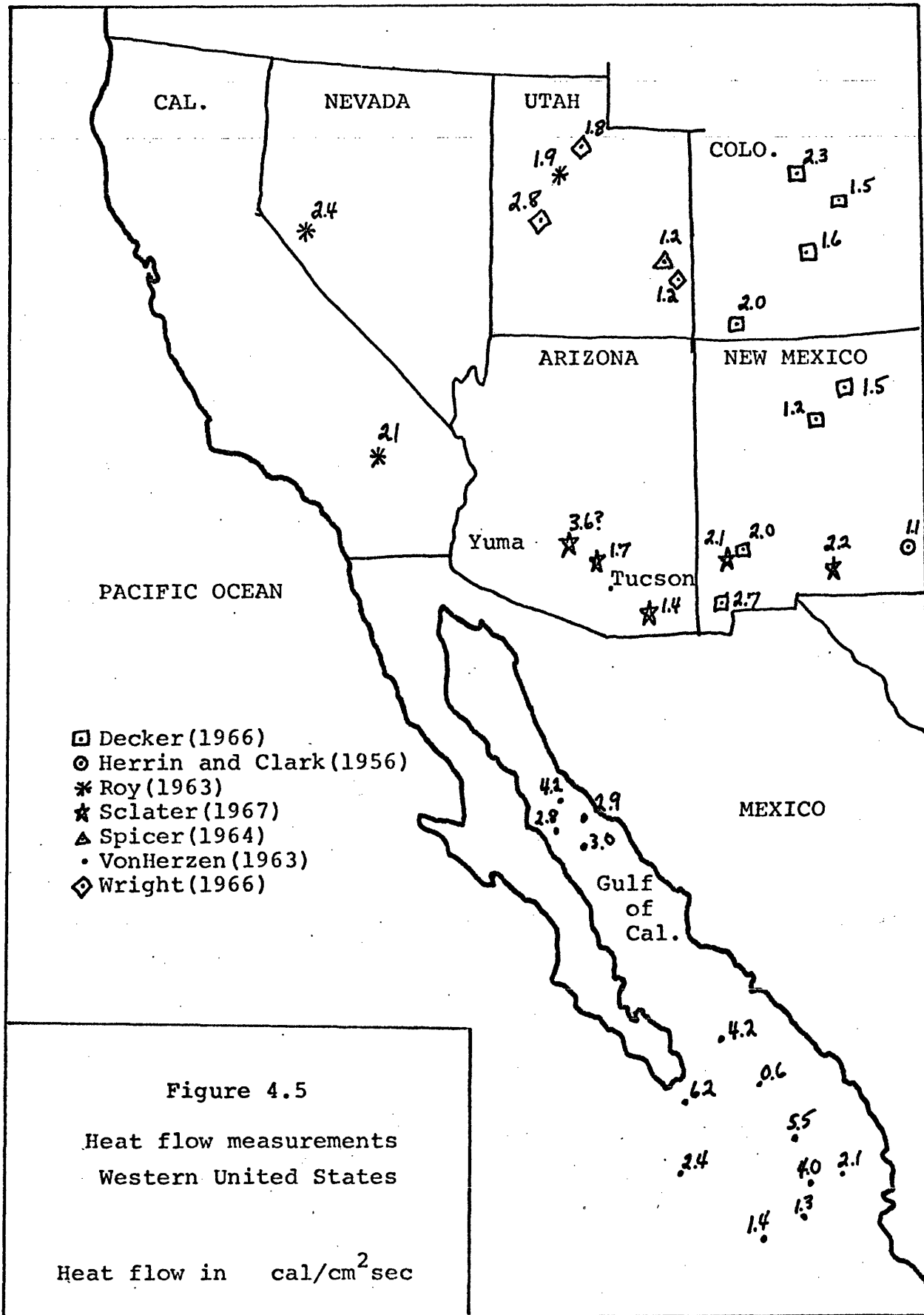


density can be explained. The consistency of the model to incorporate the differences in electrical conductivity, seismic velocity, density and phase also suggests that little melt is present.

#### Heat flow evidence

Figure 4.5 shows the heat flow values observed in the southwestern United States. High values of heat flow are indicated in the anomalous zone of high electrical conductivity and low  $P_n$  velocity. The regional average seems to be  $2.0 \mu\text{cal/cm}^2 \text{ sec}$ , with higher values probably associated with crustal intrusives or geothermal activity. Because of the time constant of about 30 million years for heat to pass through the outer 50 km of the earth, surface heat flow patterns possess a significant lag, and, thus, cannot be directly correlated with the relatively instantaneous magnetotelluric and seismic data.

A  $600^\circ$  increase in temperature at a depth of 50 kms, however, should be associated with an enhanced surface heat flow. As long as this increase in temperature does not affect the thermal conductivity structure, its contribution to the surface heat flow adds linearly to the normal heat flow. For a thermal conductivity of 0.006

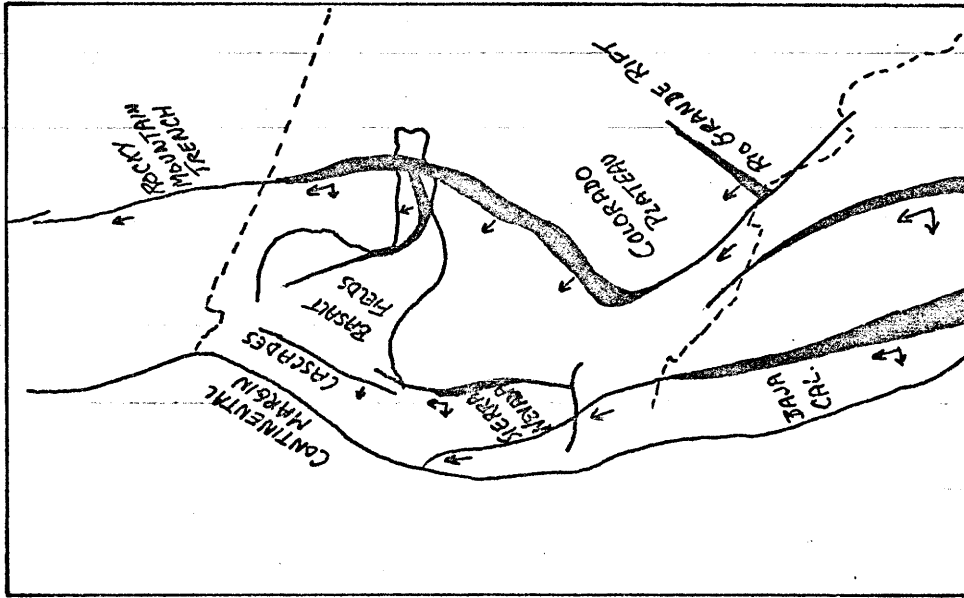


cal/cm sec. degree and a normal heat flow of  $1.2 \mu\text{cal/cm}^2$  sec., the expected steady state heat flow over the anomalous region is  $1.9 \mu\text{cal/cm}^2$  sec. Because this value is conservative for the observed heat flow, the postulated high temperature zone is not unreasonable.

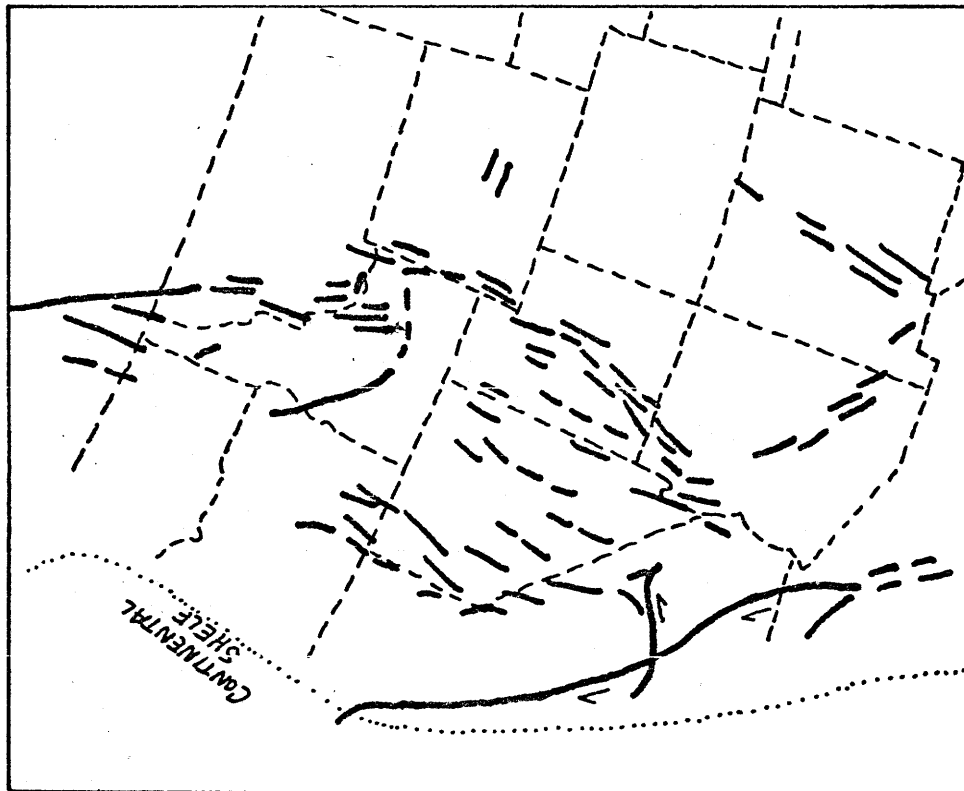
#### Relationship to the East Pacific Rise

In discussions of the tectonic evolution of the western United States, an "anomalous mantle" has been an integral feature (Cook, 1962; Gilluly, 1963; Thompson and Talwani, 1964; Pakiser and Zietz, 1965; etc.). Crustal tectonics are dominated by the late Cenozoic fault system (Figure 4.6). The strike-slip San Andreas fault system is characterized by shallow epicenters and is probably a more recent structure superimposed on the rest of the Cordilleran system. The Basin and Range block fault system is characterized by up to 300 km of extension (Hamilton and Myers, 1966) and by the possibility that some of these faults extend into the mantle (Roller, 1964).

The eastern margin of the Basin and Range province is an active belt of seismicity (Woollard, 1958) and en-echelon rift grabens (Cook, 1966). Cook (1962, 1966) connects the rift valleys of Utah and Arizona with the Rocky Mountain



Speculative extensional pattern  
(After Eardley, 1962)



Cenozoic fault system  
Western United States

Figure 4.6

trench of British Columbia to form a typical rift system of tension faults, thin crust, low  $P_n$  velocity, high heat flow, and high seismicity. This rift system is then attributed to a one-sided convective pattern upwelling at the rift zone to produce the uplift of the Colorado Plateau, moving westward to produce the extension in the Basin and Range.

This anomalous mantle zone is probably the continental extension of the East Pacific Rise, which is characterized by a broad topographic rise about 1000 km wide, low velocities, and high heat flow (Langseth, et al, 1965). Raitt (1964) believes that on the East Pacific Rise the strong correlation of low velocity with high heat flow is consistent with the hypothesis that the mantle material is normal, but its low velocity is caused by the high temperatures associated with high heat flow.

The topographic expression and the axis of high heat flow of the East Pacific Rise strikes into the North American continent at the Gulf of California and much uncertainty exists about its possible extension, although magnetic anomalies indicate short ridge lengths in the Pacific off Vancouver Island (Vine, 1966). Originally, Menard (1960) related the plateau of Mexico, the Basin and

Range province, and the Colorado Plateau to a continental extension of the East Pacific Rise. Recently it has become fashionable to classify the San Andreas fault as a transform fault connecting oceanic segments of the Rise, in which case there is no crest of the ridge between the Gulf of California and north of the Mendocino Escarpment.

The low  $P_n$  velocities and high electrical conductivity observed in the Basin and Range province and the Colorado Plateau, however, suggest that the East Pacific Rise and its associated high temperature zone extends northward from the Gulf of California and underlies the rift system as described by Cook. Although Vine (1966) has suggested that the Cenozoic tectonic history of the western United States can be attributed to the continent overriding and partially resorbing first a typical Pacific trench and more recently the crest of the East Pacific Rise, the present tensional forces, seismicity, and high temperatures indicate that typical ridge tectonics are operating now. A picture of one geologist's view of the present extensional pattern is shown in Figure 4.6 (Eardley, 1962). The observed NW-SE direction of tension is the same as that direction now operative for the oceanic Rise (Vine, 1966).

The East Pacific Rise is probably ultimately caused by

convective motions at depth (Von Herzen and Uyeda, 1963).

Excess heat could be transported through a high temperature upper mantle by means of increased radiative transfer and/or convective transfer via a liquid fraction within a solid peridotite matrix. Because the "conductive" geotherm may lie in the zone of partial melting, the convective transfer of heat via the minor liquid basalt portion possibly represents the physical mechanism which supports the temperature differential.

## Chapter 5 - Suggestions for Future Work

Theoretical studies are needed to quantitatively understand the effects of simple three-dimensional features. Only then can impedance data like that from Yuma and Tucson be properly interpreted.

For investigations of deep conductivity structure, continuous telluric coverage is necessary to adequately correct for the surface inhomogeneities or very long electrode separations are necessary. Therefore, many more magnetotelluric stations are required to properly interpret the anomalous conductivity zone in the southwestern United States. A profile of stations across the Rio Grande rift valley and the rift valleys of Utah would be most interesting.

The potential usefulness of the upper mantle temperatures obtainable from the specific magnetotelluric conductivity estimates suggests that the magnetotelluric technique should be included in investigations of other parts of the world's primary tectonic features. Interesting areas would be normal oceanic sites, oceanic trenches, and oceanic and other continental expressions of the world rift system.

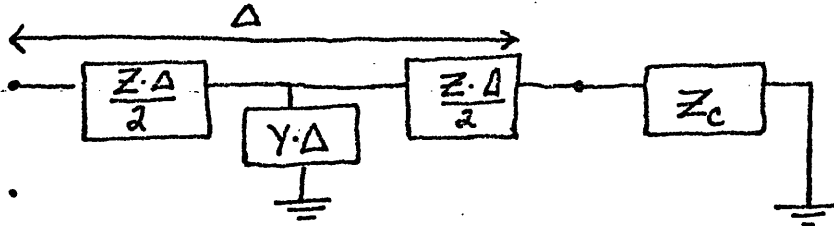


The correspondence between the interpreted magnetotelluric conductivity values and laboratory conductivity measurements on mantle materials suggests that an extension of magnetotelluric soundings to lower frequencies could yield information on the postulated phase transitions (particularly the olivine-spinel transition) in the mantle. Conversely, extension of the laboratory conductivity measurements to more realistic (more heterogeneous) assemblages and to higher temperatures would yield further information on possible conductivity mechanisms and on the minor constituent contribution to conductivity. Geotherms interpreted from magnetotelluric conductivity profiles would be more reliable with this information.

Appendix 1 - Error introduced by lumped circuit approximation to a distributed transmission line

Greenfield (1965) has evaluated the error due to grid spacing in a finite difference method solution to the scalar wave equation. The error introduced in the transmission line analogy method lies in approximating the distributed line by lumped circuit elements.

A maximum layer thickness criterion for a one-dimensional transmission line can be obtained by considering one layer, of thickness  $\Delta$ , over a homogeneous half space of the same conductivity. Then the lumped circuit is



where the characteristic impedance,  $Z_c = \sqrt{Z/Y}$

The surface impedance, which in this case should equal the characteristic impedance, is given as

$$Z_{\text{surface}} = \sqrt{\frac{Z}{Y}} \sqrt{1 + \frac{ZY\Delta^2}{4}}$$

A1-1

Therefore, the finite layer width introduces negligible error if, since  $ZY = -k^2$ ,

$$k \Delta \ll 2$$

A1-2

This criterion is roughly equivalent to requiring the layer thickness to be much less than a wave length in that layer. This is a straightforward restriction for the one-dimensional layered earth model and for the vertical spacing in a two-dimensional model. For the horizontal spacing in a two dimensional grid, spacing less than a horizontal wavelength is required. Since lateral conductivity contrasts can produce horizontal wavelengths due to diffraction effects near the contrasts, even if infinite horizontal wavelengths are assumed for the incident wave, horizontal spacing of the order of the vertical spacing is required near the contrasts.

It is impossible to analytically calculate the effect of a too-large grid spacing for an arbitrary two-dimensional case. An empirical check for a one-dimensional case results from the fact that large vertical grid spacings affect the calculated apparent resistivities oppositely when the E parallel and E perpendicular formulation are applied to a one-dimensional case. This effect results from the different associations made in the transmission line analogy for the two polarizations:

---

E parallel:	$V \Leftrightarrow E$	$I \Leftrightarrow H$	A1-3
-------------	-----------------------	-----------------------	------

---

E perpendicular:	$I \Leftrightarrow E$	$V \Leftrightarrow H$	A1-4
------------------	-----------------------	-----------------------	------

Therefore, for the E parallel polarization, the network impedance (V/I) is equivalent to the magnetotelluric impedance (E/H). For the E perpendicular case, the network impedance is equivalent to the magnetotelluric admittance. Since the product ZY is the same for both cases, the effect on the network impedance, as expressed in equation A1-1 is the same and, thus, the effect on the magnetotelluric impedance and, hence, on the apparent resistivities, is opposite. Any difference between the  $E_{\perp}$  and  $E_{\parallel}$  apparent resistivities gives an estimate of the error introduced by the vertical spacing. Moreover, the true value lies between the two calculated values.

Appendix 2 - Calculation of the vertical electric field

associated with a toroidal B mode diurnal

From equation 2.3-6, the toroidal B solutions are given as:

$$H = \sum \sum a_{MM} M_{MM} \quad \text{A2-1}$$

$$E = \frac{i\omega\mu}{k} \sum \sum a_{MM} N_{MM} \quad \text{A2-2}$$

where the components are given as

$$H_{\theta}^{MM} = a_{MM} \left( j_m(kR) \frac{\partial Y_m^m}{\sin\theta \partial \phi} \right) \quad \text{A2-3}$$

$$H_{\phi}^{MM} = a_{MM} \left( -j_m(kR) \frac{\partial Y_m^m}{\partial \theta} \right) \quad \text{A2-4}$$

$$E_r^{MM} = a_{MM} \left( \frac{i\omega\mu R(m+1)}{k} \frac{j_m(kR)}{kR} Y_m^m \right) \quad \text{A2-5}$$

$$E_{\theta}^{MM} = a_{MM} \left( \frac{i\omega\mu}{k^2 R} \frac{d}{dR} [R j_m(kR)] \frac{\partial Y_m^m}{\partial \theta} \right) \quad \text{A2-6}$$

$$E_{\phi}^{MM} = a_{MM} \left( \frac{i\omega\mu}{k^2 R} \frac{d}{dR} [R j_m(kR)] \frac{\partial Y_m^m}{\sin\theta \partial \phi} \right) \quad \text{A2-7}$$

A matrix formulation of Maxwell's equations for each harmonic, similar to that of equation 2.3-20 for the

poloidal B mode, is obtained analogously for the toroidal B mode,

$$\frac{\partial}{\partial r} \begin{bmatrix} r E_{\theta} \\ r H_{\phi} \end{bmatrix} = \begin{bmatrix} 0 & i\omega\mu \left(1 - \frac{m(m+1)}{k^2 r^2}\right) \\ -\sigma & 0 \end{bmatrix} \begin{bmatrix} r E_{\theta} \\ r H_{\phi} \end{bmatrix} \quad \text{A2-8}$$

Although this set is slightly different than equation 2.3-20, the long wavelength criterion is still

$$m(m+1) \ll k^2 r^2 \quad \text{A2-9}$$

The Riccati equation for the toroidal B impedance can be simply obtained from A2-8 and is

$$\frac{\partial Z_m}{\partial r} = \sigma Z_m^2 + i\omega\mu \left(1 - \frac{m(m+1)}{k^2 r^2}\right) \quad \text{A2-10}$$

Note that this expression reduces to the flat earth case for  $m = 0$ .

The vertical electric field,  $E_r$ , for a diurnal variation of  $50\%$  in  $H_{\phi}$  is simply calculated from evaluating A2-5. The diurnal variation is the  $n = 2$ ,  $m = 1$  harmonic. Therefore

$$|H_{\phi}^{12}| = |a_{12} j_2(k_{10}) \frac{\partial P_2'}{\partial \theta} e^{i\phi}| = 50 \gamma \quad \text{A2-11}$$

$$|E_{\Lambda}^{12}| = |a_{12} \frac{i\omega \Lambda b}{k^2 \Lambda_0} j_2(k_{10}) P_2' e^{i\phi}| \quad \text{A2-12}$$

Since

$$\frac{\partial P_2'}{\partial \theta} = \frac{\partial}{\partial \theta} \left( \frac{3}{2} \sin 2\theta \right) = 3 \cos 2\theta \quad \text{A2-13}$$

$$\left| \frac{\partial P_2'}{\partial \theta} \right|_{\text{MAX}} = 2 |P_2'|_{\text{MAX}} \quad \text{A2-14}$$

Then equation A2-11 can be expressed as

$$|a_{12} j_2(k_{10}) P_2' e^{i\phi}| = 25 \gamma \quad \text{A2-15}$$

Then the expression for the electric field reduces to

$$|E_{\Lambda}^{12}| = |a_{12} j_2(k_{10}) P_2' e^{i\phi}| \frac{6}{\sigma \Lambda_0} = \frac{150 \gamma}{\sigma \Lambda_0} \quad \text{A2-16}$$

Converting this expression to MKS units, and using a resistivity of 20 ohm meters as representative for the diurnal period, yields

$$|E_n^{12}| = \frac{(150 \times 10^{-5})(20 \Omega\text{-m})}{(6.4 \times 10^6 \text{ m})} \quad \text{A2-17}$$

Therefore

$$E_n(\text{ground}) \approx 0.75 \times 10^{-6} \text{ volts/meter} \quad \text{A2-18}$$

For the electric field in the air,

$$E_n(\text{air}) = \frac{\sigma_{\text{ground}}}{\sigma_{\text{air}}} E_n(\text{ground}) = 0.75 \times 10^5 \frac{\text{volts}}{\text{meter}} \quad \text{A2-19}$$

This value is unrealistically large and suggests that the low frequency geomagnetic field is in the poloidal B mode. Greenfield (1965), in considering transmission through the ionosphere, concluded that the low frequency toroidal B field is severely reflected by the atmosphere layer.



Appendix 3 - Greenfield algorithm for the direct solution  
of the magnetotelluric network equations

The large set of simultaneous linear equations  
resulting from the discrete network analog to electro-  
magnetic wave propagation in the earth can be arranged in  
the following form:

$$C V = S \quad \text{A3-1}$$

Where  $V$  (1, ..., N·M) unknown voltages

$S$  (1, ..., N·M) source terms and boundary conditions

$C$  (N·M by N·M) coefficient matrix

To avoid an N·M by N·M matrix inversion (360 by 360 for my  
largest grid), an algorithm developed by Greenfield (1965)  
which only involves M N by N inversions can be applied  
since C is of the form

$$C = \begin{bmatrix} A_1 & D_1 & & & & \\ & D_1 & A_2 & D_2 & & \\ & & & \ddots & & \\ & & & & A_{M-1} & D_{M-1} \\ & & & & D_{M-1} & A_M \end{bmatrix}$$

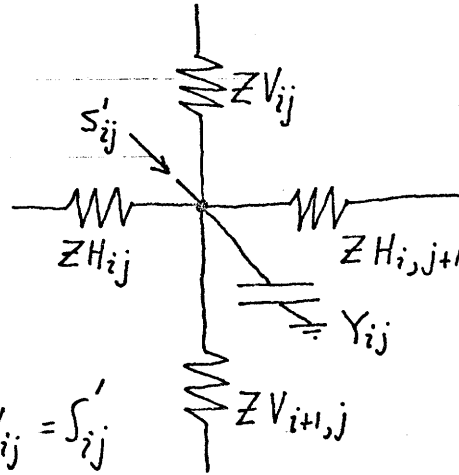
where  $A_i$  and  $D_i$  are N by N and  $D_i$  are diagonal. Figure  
A-1 shows this form for C for a small grid.

For a simple 3 by 4 grid

At each node

Node equation

$$\sum \frac{V_{neigh} - V_{ij}}{Z_{connecting}} + Y_{ij} V_{ij} = S'_{ij}$$



For  $[C][V] = [S]$

$$\left( \frac{1}{ZV_{11}} + \frac{1}{ZH_{12}} + \frac{1}{ZV_{21}} + \frac{1}{ZH_{11}} + Y_{11} \right)$$

$\left( \frac{1}{ZH_{12}} \right)$	$-\frac{1}{ZV_{21}}$			$V_{11}$	$S'_{11}$
$\frac{1}{ZH_{12}} \left( \right) \frac{1}{ZH_{13}}$	$-\frac{1}{ZV_{22}}$			$V_{12}$	$S'_{12}$
$\frac{1}{ZH_{13}} \left( \right)$	$-\frac{1}{ZV_{23}}$			$V_{13}$	$S'_{13}$
$-\frac{1}{ZV_{21}}$	$\left( \right) \frac{1}{ZH_{22}}$	$\frac{1}{ZV_{31}}$		$V_{21}$	$S'_{21}$
$-\frac{1}{ZV_{22}}$	$\frac{1}{ZH_{22}} \left( \right) \frac{1}{ZH_{23}}$	$-\frac{1}{ZV_{32}}$		$V_{22}$	$S'_{22}$
$-\frac{1}{ZV_{23}}$	$-\frac{1}{ZH_{23}} \left( \right)$	$-\frac{1}{ZV_{33}}$		$V_{23}$	$S'_{23}$
	$-\frac{1}{ZV_{31}}$	$\left( \right) \frac{1}{ZH_{32}}$	$-\frac{1}{ZV_{41}}$	$V_{31}$	$S'_{31}$
	$-\frac{1}{ZV_{32}}$	$\frac{1}{ZH_{32}} \left( \right) \frac{1}{ZH_{33}}$	$-\frac{1}{ZV_{42}}$	$V_{32}$	$S'_{32}$
	$-\frac{1}{ZV_{33}}$	$-\frac{1}{ZH_{33}} \left( \right)$	$-\frac{1}{ZV_{43}}$	$V_{33}$	$S'_{33}$
		$-\frac{1}{ZV_{41}}$	$\left( \right) -\frac{1}{ZH_{42}}$	$V_{41}$	$S'_{41}$
		$-\frac{1}{ZV_{42}}$	$\frac{1}{ZH_{42}} \left( \right) -\frac{1}{ZH_{43}}$	$V_{42}$	$S'_{42}$
		$-\frac{1}{ZV_{43}}$	$-\frac{1}{ZH_{43}} \left( \right)$	$V_{43}$	$S'_{43}$

Figure A-1 Coefficient matrix for network solution

Partitioning C into two triangular matrices,

$$C = EF$$

A3-2

where

$$E = \begin{bmatrix} I & & & & \\ E_1 & I & & & \\ & & \dots & & \\ & & & I & \\ & & & E_{M-1} & I \end{bmatrix}$$

$$F = \begin{bmatrix} F_1 & G_1 & & & \\ & F_2 & G_2 & & \\ & & & \dots & \\ & & & & F_{n-1} & G_{n-1} \\ & & & & & F_M \end{bmatrix}$$

Therefore

$$C = \begin{bmatrix} A_1 & D_1 & & & \\ D_1 & A_2 & & & \\ & & \dots & & \\ & & & & A_n \end{bmatrix} = EF = \begin{bmatrix} F_1 & G_1 & & & \\ E_1 F_1 & (F_2 + E_1 G_1) & & & \\ & & \dots & & \\ & & & & G_2 \end{bmatrix}$$

The elements of E and F can be obtained by

$$F_1 = A_1$$

A3-3

$$k=1, \dots, M-1 \left\{ \begin{array}{l} G_k = D_k \\ E_k = D_k F_k^{-1} \end{array} \right.$$

A3-4

A3-5

$$F_{k+1} = A_{k+1} - E_k G_k = A_{k+1} - E_k D_k$$

A3-6

The solution for V is through an intermediate vector,

$$Z = FV$$

A3-7

From  $C = EF$  the basic equation A3-1 transforms to

$$EFV = S \quad \text{A3-8}$$

Therefore, since  $FV = Z$

$$EZ = S \quad \text{A3-9}$$

Since  $E$  is triangular, the solution for  $Z$  is simply

$$Z_1 = S_1 \quad \text{A3-10}$$

$$Z_{k+1} = S_{k+1} - E_k Z_k \quad \text{A3-11}$$

For the solution  $V$ , equation A3-7 gives

$$V_M = F_M^{-1} Z_M \quad \text{A3-12}$$

$$V_k = F_k^{-1} (Z_k - D_k V_{k+1}) \quad \text{A3-13}$$

For  $k = M-1, \dots, 1$

Note that the  $F_k^{-1}$  inversions already appear in the computations of  $E_k$ .

This algorithm holds for complex coefficient matrices of the required form. The following computation simplification, which is valid for long horizontal wavelengths, allows the construction of the coefficient matrix  $C$  such that all off-diagonal elements are real, for both polarizations.

From Figure A-1 and ignoring grid spacing parameters in the lumped elements, C is composed of:

<u>element</u>	<u>characterized by</u>	<u>for E<sub>⊥</sub></u>	<u>for E<sub>∥</sub></u>	<u>for E<sub>∥</sub> x (-1)</u>
A <sub>jj</sub>	$\Sigma (\frac{1}{z}) + Y$	$\frac{1}{\sigma} - i\mu\omega$	$-\frac{1}{i\mu\omega} + \sigma$	$\frac{1}{\mu\omega} - i\sigma$
A <sub>j,j+1</sub>	$-\frac{1}{z}$	$-\frac{1}{\sigma}$	$\frac{1}{i\mu\omega}$	$-\frac{1}{\mu\omega}$
D <sub>jj</sub>	$-\frac{1}{z}$	$-\frac{1}{\sigma}$	$\frac{1}{i\mu\omega}$	$-\frac{1}{\mu\omega}$

Therefore, by multiplying C by (-i) for the E parallel case, the coefficient matrix C for both polarizations is characterized by having complex elements only along the diagonals. Then, by multiplying S by (-i) for the E parallel case, solutions for both polarizations can be computed by a Greenfield algorithm simplified by many real matrix multiplications.

Appendix 4 - Principal axes and principal values of the  
MT impedance tensor

For a two-dimensional structure, the eigenvectors of a theoretical impedance tensor are real, are oriented with and against the structural strike, and can be directly interpreted as principal axes. For measured tensors, only when the eigenvectors are almost cartesianally orthogonal and possess small imaginary parts can a straightforward eigenvector analysis be used. An approach to eliminate the  $Z_{11}$  and  $Z_{22}$  elements by diagonalizing  $Z \times \begin{bmatrix} 0 & 1 \\ 1 & 0 \end{bmatrix}$  results in skew axes with associated phases. To avoid interpreting complex skew eigenvectors, other approaches must be used for defining principal axes

- 1) To find the directions where a linearly polarized H will produce an E in only the perpendicular direction.

For  $\bar{H} = \bar{u}$ , where  $\bar{u}$  is real, E must satisfy

$$\bar{E} = \lambda \begin{bmatrix} 0 & 1 \\ -1 & 0 \end{bmatrix} \bar{u} \quad \text{A4-1}$$

Applying  $E = ZH$ , a standard eigenvalue problem results:

$$\lambda \begin{bmatrix} 0 & 1 \\ -1 & 0 \end{bmatrix} \bar{u} = Z \bar{u} \quad \text{A4-2}$$

$$\therefore \begin{bmatrix} 0 & +1 \\ -1 & 0 \end{bmatrix}^{-1} Z \bar{u} = \lambda \bar{u} \quad \text{A4-3}$$

The eigenvectors  $\bar{u}$  are in generally non-orthogonal directions. This approach is an analytic formulation of the criterion used by Bostick and Smith (1962) for the principal axes of the admittance tensor.

- 2) To find the direction for maximum "Cagniard element" ( $Z_{12}$  or  $Z_{21}$ )

Since  $Z_{12}(\theta) = Z_{21}(\theta + 90^\circ)$ , either element can be considered over a  $180^\circ$  range. From

$$Z'_{12} = Z_{12} \cos^2 \phi + (Z_{22} - Z_{11}) \sin \phi \cos \phi - Z_{21} \sin^2 \phi \quad 2.5-6b$$

the direction for the maximum Cagniard element is where

$$\frac{\partial}{\partial \phi} (|Z'_{12}|) = 0 \quad \text{A4-4}$$

This criterion emphasized the preferred current direction approach. Another similar criterion involves calculating the direction where a) the diagonal terms are least

$$(Z_{11}, Z_{22})$$

or b) the Cagniard elements are largest

A little algebra applied to equations 2.4-8 shows that

$$\phi \text{ for } \min \{ |z'_{11}|^2 + |z'_{22}|^2 \} = \phi \text{ for } \max \{ |z'_{11}|^2 + |z'_{21}|^2 \} \text{ A4-5}$$

Since  $z'_{12}(\phi_{\text{opt}}) \gg z'_{21}(\phi_{\text{opt}})$ , or vice versa, this criterion usually gives a similar direction to that from approach (2).

Principal values of the impedance tensor

To obtain apparent resistivities for these principal directions, the eigenvalues from A3-3 are appropriate for approach (1), and  $z'_{12}(\phi_{\text{opt}})$  for approach (2).

Additionally, the cross-coupled eigenvalue approach of Lanczos (1961) was applied. This approach for non-square, non-Hermitian matrices emphasizes the two separate vector spaces associated with the matrix. In this approach, matrix  $Z$  is interpreted as operating on  $H$  (expressed in the  $\underline{V}$  space) to produce a resultant  $E$  (expressed in the  $\underline{U}$  space). Two sets of eigenvectors result from this approach.

The formulation cross-couples the eigenvectors through the matrix and its complex conjugate transpose.

$$\begin{aligned} Z u &= \lambda v \\ \bar{Z} v &= \lambda u \end{aligned}$$



These can be solved by

$$Z \bar{Z} u = \lambda^2 u$$

A4-7

$$\bar{Z} Z v = \lambda^2 v$$

Since  $Z \bar{Z}$  and  $\bar{Z} Z$  are Hermitian,  $\lambda^2$  is positive real and two real eigenvalues can be used for apparent resistivities, but without associated phases. The E eigenvectors  $\bar{u}_1$  and  $\bar{u}_2$  are Hermitianly orthogonal. Thus, in considering the Fourier component  $\bar{E}_i = \bar{E}_{0i} e^{-i\omega t} \bar{u}_i$ , these eigenvectors are elliptically polarized and rotate in space with time. Although these eigenvectors are not instantaneously geometrically orthogonal, the principal axes of the polarization ellipses are. This approach seems to be best mathematically, but the principal axes are difficult to handle conceptually. More work could be done in this area.

Appendix 5 - Computational details of the sonogram  
analysis

The sonogram analysis for the higher frequencies utilizes various digital recursive operators, a topic recently discussed by Radar and Gold (1965) and Shanks (1965). First, the four data series ( $E_x$ ,  $E_y$ ,  $H_x$ ,  $H_y$ ) were high pass filtered using a 3 pole Chebyshev filter operator. Then the data were fed continuously into a bank of recursive filters, for which the Q's are set so that the response of neighboring filters overlap at the filter half-power points. For the frequency band of  $1.1 \times 10^{-3}$  to  $1.7 \times 10^{-4}$  cps the filters used had a Q of 6.53. Each filter was a five point operator with a Chebyshev filter response. Such a recursive band pass operator can be considered as the operation of dividing by a band reject filter. The amplitude response of the combined digital high pass and a particular recursive filter is shown in Figure A-2. These filters have a ringing time of twice the period of the band pass frequency.

The filter outputs were lagged  $90^\circ$  to obtain a quadrature component. Then power spectra were obtained using the following formulae:

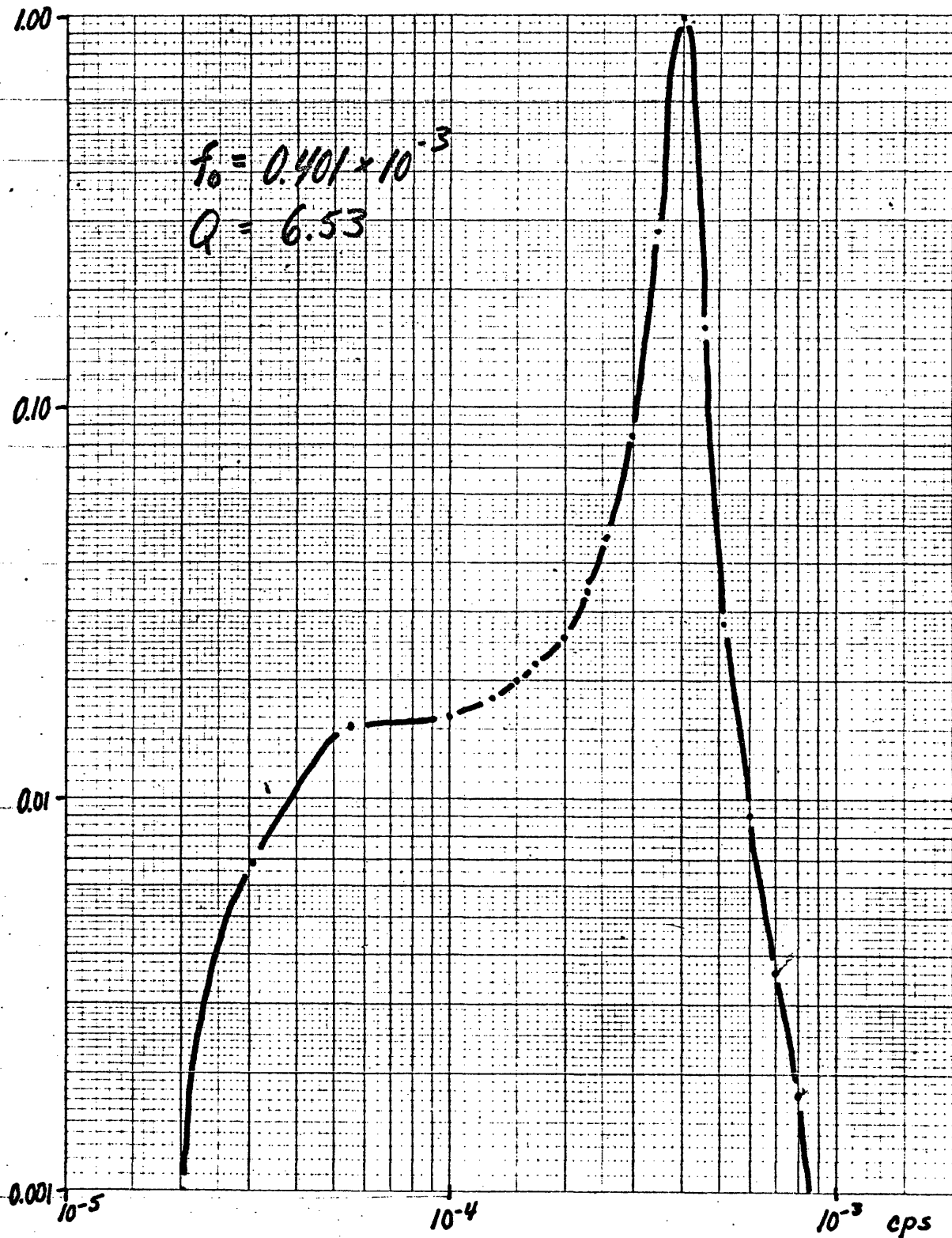


Figure A-2 Amplitude response of combined digital high-pass and a particular constant-Q recursive filter.

$$\text{Auto power: } E_x \bar{E}_x = E_x^2 \text{ (in phase)} + E_x^2 \text{ (quadrature)}$$

Cross power:

$$\begin{aligned} \text{Re}(E_x \bar{H}_y) &= E_x \text{ (in phase)} * H_y \text{ (in phase)} \\ &+ E_x \text{ (out of phase)} * H_y \text{ (out of phase)} \end{aligned}$$

$$\begin{aligned} \text{Im}(E_x \bar{H}_y) &= E_x \text{ (out of phase)} * H_y \text{ (in phase)} \\ &- E_x \text{ (in phase)} * H_y \text{ (out of phase)} \end{aligned}$$

These power spectra were averaged in time using another recursive operator with a half-power memory time of 192 points (equivalent to 8 hours of data). Note that because the expressions for coherency and the tensor elements involve ratios of these power spectra, the equal phase shifts introduced by the constant-Q filters need not be corrected.

References

- Akimoto, S., and H. Fujisawa, Demonstration of the electrical conductivity jump produced by the olivine-spinel transition, J. Geophys. Res., Vol. 70, pp. 443-449, 1965.
- Bartels, J., N. H. Heck and H. F. Johnston, The three-hour-range index measuring geomagnetic activity, J. Terr. Magnetism, Vol. 44, pp. 411-454, 1939.
- Barus, C., and J. P. Iddings, Note on the change of electric conductivity observed in rock magmas of different composition on passing from liquid to solid, Amer. Journal of Science, pp. 242-249, 1892.
- Biehler, S., R. C. Kovach and C. R. Allen, Geophysical framework of northern end of Gulf of California structural province, pp. 126-143, in Marine Geology of the Gulf of California, American Association of Pet. Geol., Memoir #3, 1964
- Birch, F., Density and composition of mantle and core, J. Geophys. Res., Vol. 69, pp. 4377-4388, 1964.
- Bostick, F. X., Jr., and H. W. Smith, Investigation of large-scale inhomogeneities in the earth by the magnetotelluric method, Proc. Inst. Radio Engineers, Vol. 50, pp. 2339-2346, 1962.
- Bradley, R. S., A. K. Jamil and D. C. Munro, Electrical conductivity of fayalite and spinel, Nature, Vol. 193, pp. 965-966, 1962.
- Cagniard, L., Basic theory of the magnetotelluric method of geophysical prospecting, Geophysics, Vol. 18, pp. 605-635, 1953.
- Caner, B., and W. H. Cannon, Geomagnetic depth-sounding and correlation with other geophysical data in Western North America, Nature, Vol. 207, pp. 927-929, 1965.

- Cantwell, T., Detection and analysis of low frequency magnetotelluric signals, Ph.D. Thesis, Department of Geology and Geophysics, M.I.T., 1960.
- Chapman, S., Solar Plasma, Geomagnetism and Aurora, Gordon and Breach (New York), 1964.
- Chapman, S., and J. Bartels, Geomagnetism, Oxford Univ. Press (London), 1940.
- Chapman, S., and A. T. Price, The electric and magnetic state of the interior of the earth, as inferred from terrestrial magnetic variations, Phil. Trans. Roy. Soc. London, A., Vol. 229, pp. 427-460, 1930.
- Chapman, S., and T. T. Whitehead, The influence of electrically conducting material within the earth on various phenomena of terrestrial magnetism, Trans. Phil. Soc. Cambridge, Vol. 22, pp. 463-482, 1923.
- Chetaev, D. N., The determination of the anisotropy coefficient and the angle of inclination of a homogeneous anisotropic medium, by measuring the impedance of the natural electromagnetic field, Izvest., Geophys. Series, pp. 617-619, 1960.
- Clark, S. P., Jr., ed., Handbook of Physical Constants, Geol. Soc. of Amer. Memoir #97, 1966.
- Clark, S. P., Jr., and A. E. Ringwood, Density distribution and constitution of the mantle, Reviews of Geophysics, Vol. 2, pp. 35-88, 1964.
- Cook, K. L., The problem of the mantle-crust mix: lateral inhomogeneity in the uppermost part of the earth's mantle, Advances in Geophysics, Vol. 9, pp. 295-360, 1962.
- Cook, K. L., Rift system in the Basin and Range province, pp. 246-279, in the World Rift System, Geological Survey of Canada Paper 66-14, 1966.
- Coster, H. P., The electrical conductivity of rocks at high temperatures, Monthly Notices Roy. Ast. Soc., Geophy. Suppl. Vol. 5, pp. 193-199, 1948.

- Decker, E. R., Terrestrial heat flow in Colorado and New Mexico, Ph.D. Thesis, Department of Geophysics, Harvard University, 1966.
- Eardley, A. J., Structural Geology of North America, Second edition, Harper and Row (New York), 1962.
- Eckhardt, D., K. Larner, and T. Madden, Long-period magnetic fluctuations, and mantle conductivity estimates, J. Geophys. Res., Vol. 68, pp. 6279-6286, 1963.
- Ellis, R. M., Analysis of natural ultra low frequency electromagnetic fields, Ph.D. Thesis, Dept. of Physics, Univ. of Alberta, 1964.
- d'Erceville, I., and G. Kunetz, The effect of a fault on the earth's natural electromagnetic field, Geophysics, Vol. 27, pp. 651-665, 1962.
- Filloux, J., Private communication, 1966.
- Fleming, J. A., Terrestrial Magnetism and Electricity, McGraw-Hill (New York), 1939.
- Fournier, H. G., S. H. Ward, and H. F. Morrison, Magneto-telluric evidence for the low velocity layer, Tech. Report of Nov. 22(89), Series No. 4, Issue No. 76, Space Sciences Lab, U. of Calif., Berkeley, 1963.
- Fournier, H. G., Essai d'un historique des connaissances magnetotelluriques, Note 17, Institut de Physique du Globe, Universite de Paris, 1966.
- Gilluly, J., The tectonic evolution of the western United States, Quart. J. Geol. Soc. London, Vol. 119, pp. 133-174, 1963.
- Greenfield, R. J., Two-dimensional calculations of magnetic micropulsation resonances, Ph.D. Thesis, Department of Geology and Geophysics, M.I.T., ONR Project NR-371-401 Report, 1965.
- Hales, A. L., and H. A. Doyle, P and S travel-time anomalies and their interpretation, Contribution #47, Geosciences Div., SW Center for Advanced Studies, pp. 1-28, 1967.

Hamilton, R. M., Temperature variation at constant pressures of the electrical conductivity of periclase and olivine, J. Geophys. Res., Vol. 70, pp. 5679-5692, 1965.

Hamilton, W., and W. B. Myers, Cenozoic tectonics of the western United States, Reviews of Geophysics, Vol. 4, pp. 509-550, 1966.

Herrin, E., and S. P. Clark, Jr., Heat flow in West Texas and eastern New Mexico, Geophysics, Vol. 21, pp. 1087-1099, 1956.

Herrin, E., and J. Taggart, Regional variations in  $P_n$  velocity and their effect on the location of epicenters, Bull. Seism. Soc. of Amer., Vol. 52, pp. 1037-1046, 1962.

Hopkins, G. H., Jr., and H. W. Smith, An investigation of the magnetotelluric method for determining subsurface resistivities, E. E. Research Lab. Report #140, Univ. of Texas, 1966.

Hughes, H., The pressure effect on the electrical conductivity of peridot, J. Geophys. Res., Vol. 60, pp. 187-191, 1955.

Jackson, D. B., Deep resistivity probes in the southwestern United States, Geophysics, Vol. 31, pp. 1123-1144, 1966.

Keller, G. V., L. A. Anderson and J. I. Pritchard, Geological Survey investigations of the electrical properties of the crust and upper mantle, Geophysics, Vol. 31, pp. 1078-1087, 1966.

Kertz, W., The conductivity anomaly in the upper mantle found in Europe, Jour. Geomag. Geoelect. Vol. 15, pp. 185-192, 1964.

Kinney, D. M., ed., Basement Map of North America, joint publication of Amer. Assoc. of Pet. Geol. and U. S. Geol. Sur., 1967.



- Kovtun, A. A., The magnetotelluric investigation of structures inhomogeneous in layers, Izvest, Geophys. Series, pp. 1663-1667, 1961.
- Lahiri, B. N., and A. T. Price, Electromagnetic induction in nonuniform conductors, and the determination of the conductivity of the earth from terrestrial magnetic variations, Phil. Trans. Roy. Soc. London, Series A, Vol. 237, pp. 509-540, 1939.
- Lambert, A., and B. Caner, Geomagnetic 'depth-sounding' and the coast effect in Western Canada, Can. J. of Earth Sci., Vol. 2, pp. 485-509, 1965.
- Lanczos, C., Linear Differential Operators, Van Nostrand (Princeton), 1961.
- Langseth, M. C., P. J. Grim, and M. Ewing, Heat flow measurements in the East Pacific Ocean, J. Geophys. Res., Vol. 70, pp. 367-380, 1965.
- MacDonald, G.J.F., The deep structure of continents, Reviews of Geophysics, Vol. 1, pp. 587-665, 1963.
- Madden, T. R., Spectral, cross-spectral, and bispectral analysis of low frequency electromagnetic data, pp. 429-450, in Natural Electromagnetic Phenomena, D. F. Bheil, Ed., Plenum Press (New York), 1964.
- Madden, T. R., Generalized impedance concepts and applications to wave propagation problems, M.I.T. class notes, 1966.
- Madden, T. R., and P. Nelson, A defense of Cagniard's magnetotelluric method, ONR Project NR-371-401, Geophysics Lab., M.I.T., 1964.
- Madden, T. R., and W. Thompson, Low frequency electromagnetic oscillations of the earth-ionosphere cavity, Reviews of Geophysics, Vol. 3, pp. 211-254, 1965.
- McConnell, R. K., Jr., L. A. McClaine, D. W. Lee, J. R. Aronson, and R. V. Allen, A model for planetary igneous differentiation, Review of Geophysics, Vol. 5, pp. 121-172, 1967

Menard, H. W., The East Pacific Rise, Science, Vol. 132, pp. 1737-1746, 1960.

Neves, A. S., The magnetotelluric method in two-dimensional structures, Ph. D. Thesis, Department of Geology and Geophysics, M.I.T., Cambridge, Mass., 1957.

Paghis, I., Magnetic and ionospheric storms, pp. 271-298, in C. O. Hines, et al, ed., Physics of the Earth's Upper Atmosphere, Prentice-Hall (Englewood Cliffs), 1965.

Pakiser, L. C., The basalt-eclogite transformation and crustal structure in the Western United States, U.S. Geol. Sur., Prof. Paper 525-B, B1-8, 1965.

Pakiser, L. C., and J. S. Steinhart, Explosion seismology in the Western Hemisphere, pp. 123-147, in H. Odishaw, Ed., Research in Geophysics, Vol. 2, M.I.T. Press, 1964.

Pakiser, L. C., and I. Zietz, Transcontinental crustal and upper mantle structure, Reviews of Geophysics, Vol. 3, pp. 505-520, 1965.

Parkinson, W. D., The influence of continents and oceans on geomagnetic variations, Geophys. J., Vol. 6, pp. 441-449, 1962.

Peterson, D. L., Bouguer anomaly map and principal facts for gravity stations for the central Arizona Project, U.S. Geol. Sur. open-file report, 1965.

Plouff, D., Magnetotelluric soundings in the southwestern United States, Geophysics, Vol. 31, pp. 1145-1152, 1966.

Price, A. T., The theory of magnetotelluric method when the source field is considered, J. Geophys. Res., Vol. 67, pp. 1907-1918, 1962.

Rader, C. M., and B. Gold, Digital filter design techniques, M.I.T. Lincoln Lab. Technical Note, 1965-1963, 1965.

Raitt, R. W., Geophysics of the South Pacific, pp. 223-240, in H. Odishaw, ed., Research in Geophysics, Vol. 2, Solid Earth and Interface Phenomena, M.I.T. Press (Cambridge), 1964

- Rankin, D., The magnetotelluric effect in a dyke, Geophysics, Vol. 27, pp. 666-676, 1962.
- Rikitake, T., Electromagnetic induction within the earth and its relation to the electrical state of the earth's interior, Bull. Earthquake Res. Inst., Tokyo Univ., Vol. 28, pp. 45-98, 1950.
- Rikitake, T., Conductivity anomaly in the crust and mantle Chapter 19, pp. 256-288, in Electromagnetism and the Earth's Interior, Elsevier (Amsterdam), 1966.
- Rikitake, T., and K. Whitham, Interpretation of the Alert anomaly in Geomagnetic variations, Can. Jour. of Earth Sciences, Vol. 1, pp. 35-62, 1964.
- Ringwood, A. E., Mineralogy of the mantle, pp. 357-399 in Advances in Earth Science, Ed. by P. Hurley, M.I.T. Press (Cambridge), 1966.
- Ringwood, A. E., Private communication, 1966b.
- Rokityanski, I. I., On the application of the magnetotelluric method to anisotropic and inhomogeneous masses, Izvest, Geophys. Ser., pp. 1607-1613, 1961
- Rokityanski, I. I., The shore effect in variations of the earth's electromagnetic field, Izvest, Geophys. Series, pp. 1814-1822, 1963.
- Roller, J.C., Crustal structure in the vicinity of Las Vegas, Nevada, from seismic and gravity observations, U.S. Geol. Sur., Prof. Paper 475-D, pp D108-D111, 1964.
- Roller, J. C., Crustal structure in the eastern Colorado Plateaus province from seismic-refraction measurements, Bull. Seis. Soc. Amer., Vol. 55, pp. 107-119, 1965.
- Rooney, W. J., Seasonal variations in earth currents at Tucson, Terr. Magnetism, Vol. 40, pp. 183-192, 1935.
- Roy, R., Heat flow measurements in the United States, Ph.D. Thesis, Department of Geophysics, Harvard Univ., 1963.

- Schmucker, U., Anomalies of geomagnetic variations in the southwestern United States, J. of Geomag. and Geoelect. Vol. 15, pp. 193-221, 1964.
- Schmucker, U., Private communication, 1967.
- Schmucker, U., O. Hartmann, A. A. Giesecke, Jr., M. Casaverde, and S. E. Forbush, Electrical conductivity anomalies in the earth's crust in Peru, Carnegie Inst. Wash. Year Book, 63, pp. 354-362, 1964.
- Sclater, J. G., Private communication, 1967
- Shankland, T. J. Synthesis and optical properties of forsterite, Tech. Report No. HP-16, Div. of Engg. and Applied Physics, Harvard Univ., 1966.
- Shanks, J. L., Recursion filters for digital processing, Geophysics, Vol. 32, pp. 33-51, 1967.
- Slater, J. C., Microwave Transmission, Dover (New York), 1942.
- Smith, S. W., Private communication, 1967.
- Snyder, C. W., M. Neugebauer, and U. R. Rao, The solar wind velocity and its correlation with cosmic-ray variations and with solar and geomagnetic activity, J. Geophys. Res., Vol. 68, pp. 6361-6370, 1963.
- Spicer, H. C., Geothermal gradients and heat flow in the Salt Valley anticline, Utah, Boll. Geofis. Teorica Appl., Vol. 6, pp. 263-282, 1964.
- Spitznogle, F. R., Some characteristics of magnetotelluric fields in the Soviet arctic, Ph.D. Thesis, Univ. of Texas, 1966.
- Srivastava, S. P. Theory of the magnetotelluric method for a spherical conductor, Geophys., J. R. Astr. Soc., Vol. 11, pp. 373-387, 1966.
- Srivastava, S. P., J. L. Douglas, and S. H. Ward, The application of the magnetotelluric and Telluric methods in central Alberta, Geophysics, Vol. 28, pp. 426-446, 1963.

Stewart, S. W., and L. C. Pakiser, Crustal structure in eastern New Mexico interpreted from the Gnome explosion, Bull. Seis. Soc. Amer., Vol. 52, pp. 1017-1030, 1962.

Stratton, J. A., Electromagnetic Theory, McGraw Hill (New York), 1941.

Thompson, G. A., and M. Talwani, Crustal structure from Pacific Basin to central Nevada, J. Geophys. Res., Vol. 69, pp. 4813-4837, 1964.

Tikhonov, A. N., Determination of the electrical characteristics of the deep strata of the earth's crust, Dok. Akad. Nuak, USSR, Vol. 73, pp. 295-297, 1950.

Tikhonov, A. N., and M. N. Berdichevskii, Experience in the use of magneto-telluric methods to study the geologic structure of sedimentary basins, Izvest., Earth Physics, No. 2, pp. 34-41, 1966.

Tozer, D. C., The electrical properties of the earth's interior, Phys. and Chem. of the Earth, Vol. 3, pp. 414-436, 1959.

Uhri, D. C., The electrical properties of iron-rich silicates, Ph.D. Thesis, Dept. of Geology and Geophysics, M.I.T., 1961.

Vestine, E. H., The upper atmosphere and geomagnetism, pp. 471-512, in J. A. Ratcliffe, ed., Physics of the Upper Atmosphere, Academic Press (New York), 1960.

Vine, F. J., Spreading of the ocean floor: new evidence, Science, Vol. 154, pp. 1405-1415, 1966.

Von Herzen, R. P., Geothermal heat flow in the Gulfs of California and Aden, Science, Vol. 140, pp. 1207-1208, 1963.

Von Herzen, R. P., and S. Uyeda, Heat flow through the Eastern Pacific Ocean floor, J. Geophys. Res., Vol. 68, pp. 4219-4250, 1963.

- Vozoff, K., H. Hasegawa and R. M. Ellis, Results and limitations of magnetotelluric surveys in simple geologic situations, Geophysics, Vol. 28, pp. 778-792, 1963.
- Vozoff, K., and C. M. Swift, Jr., Magnetotelluric measurements in the North German Basin, (in press).
- Wait, J. R., On the relation between telluric currents and the earth's magnetic field, Geophysics, Vol. 19, pp. 281-289, 1954.
- Wait, J. R., Theory of magnetotelluric fields, J. Res. NBS, Vol. 66D, pp. 509-541, 1962.
- Warren, D. H., Private communication, 1967.
- Weaver, J. T., The electromagnetic field within a discontinuous conductor with reference to geomagnetic micropulsations near a coastline, Can. J. of Physics, Vol. 41, pp. 484-495, 1963.
- Whitham, K., Geomagnetic variation anomalies in Canada, J. of Geomag. and Geoelect., Vol. 17, pp. 481-498, 1965.
- Whitham, K., and F. Anderson, Magnetotelluric experiments in Northern Ellesmere Island, Geophys. Jour. Roy. Ast. Soc., Vol. 10, pp. 317-345, 1965.
- Wright, P. M., Geothermal gradient and regional heat flow in Utah, Ph.D. Thesis, Geophysics Department, Univ. of Utah, 1966.
- Woollard, G. P., Areas of tectonic activity in the United States as indicated by earthquake epicenters, Amer. Geophysical Union Trans., Vol. 39, pp. 1135-1150, 1958.
- Yoder, H. S., and C. E. Tilley, Origin of basalt magmas: an experimental study of natural and synthetic rock systems, J. Petrology, Vol. 3, pp. 342-532, 1962.
- Yungul, S. H., Magnetotelluric sounding three-layer interpretation curves, Geophysics, Vol. 26, pp. 465-478, 1961.

Biographical note

---

Charles Moore Swift, Jr., was born on September 26, 1940, in Boston, Massachusetts. He attended elementary schools in Exeter, New Hampshire, before graduating from Phillips Exeter Academy in 1958. He graduated magna cum laude in Geology from Princeton University in 1962 with an A.B. degree. During the summers between graduate work at M.I.T., he worked in industrial geophysical research positions. After completion of work at M.I.T., Mr. Swift will be employed by the Kennecott Copper Corporation.